The Design of Functional Ion Gels and Hydrogels for Additive Manufacturing of Devices and Composites

Jitkanya (Jenn) Wong

A dissertation

submitted in partial fulfillment of the

requirements for the degree of

Doctor of Philosophy

University of Washington

2022

Reading Committee:

Alshakim Nelson, Chair

Matthew R. Golder

Dianne J. Xiao

Program Authorized to Offer Degree:

Chemistry

University of Washington

Abstract

The Design of Functional Ion Gels and Hydrogels for Additive Manufacturing of Devices and Composites

Jitkanya (Jenn) Wong

Chair of the Supervisory Committee:

Dr. Alshakim Nelson

Department of Chemistry

Additive manufacturing (AM or 3D printing) involves selective deposition of materials in a layer-by-layer fashion to create customizable structures with precise 3-dimensional control. As AM evolved from a rapid prototyping process to a key driver towards the next industrial revolution, massive efforts have been made towards developing advanced printable materials. However, significant progress is still required to be made to push AM materials toward greater accessibility of the technology and functionality of the materials. One promising method to achieve this goal is

4D printing (4DP), which involves AM of materials that change their material properties (post-printing) in response to an external environmental stimulus. Stimuli-responsive materials have seen increased utility in AM of tissue engineering models, biomedical application, sensory and actuating devices. This thesis focuses on the development of stimuli-responsive hydrogels, ion gels, and ionoelastomers, for direct-ink-write (DIW) printing of composites, sensors, and actuators. Chapter 1 includes an overview of current stimuli-responsive materials for AM and their applications. Chapter 2 discusses the first demonstration of DIW printing of ion gel without the need of curing between layers or use of a nonsolvent, and 3D printing of soft sensors that have increased stretchability through both the material's mechanical properties and the structural auxetic design. Chapter 3 explores incorporation of polymerizable ionic liquids to print shape memory ionoelastomers that can exhibit multi-directional bending upon stretch and release of the printed structure. Chapter 4 introduces a new method of post-print photocuring opaque hydrogel/particle composites via triplet fusion upconversion to overcome the limitations posed by traditional UV curing.

TABLE OF CONTENTS

LIST OF FIGURES

LIST OF TABLES

LIST OF SCHEMES

ACKNOWLEDGEMENTS

As I'm writing this thesis, I reflected upon the journey that brought me here. This thesis would not have existed without the supports I have received from those around me. I am filled with gratitude to have been blessed with so many wonderful people in my life. First and foremost, I would like to thank my P.I. Alshakim Nelson. Al, you are my role model from day 1, and I can only hope that I will become an amazing scientist like you one day. You've allowed me to go out there and explore, to not be afraid to try new ideas, but at the same time you are always there for me to support, be there every step of the way, to encourage, inspire, and excite me about the work we do. I couldn't have asked for a better boss and will forever be thankful.

To the Nelson lab, thank you. Trevor, Amrita, Dylan, Ryan, Patrick, and Chris, thank you very being there since the first day as my mentors who shaped me into the scientist I am today. Dylan and Ryan, sorry that I'm so bad at DnD, but thank you for letting me be a part of your game nights. Dylan, you are forever my favorite desk partner who was always up for taking a break to go get coffee, snacks, or boba. Chris, who answered all my questions whether its lab related or about job applications, I cherish all our conversations. Fang, Eva, Naroa, and Gokce, you have become my sisters. I enjoyed and appreciated all the times we get to hang out outside of lab. Gokce and Naroa, you girls have become my main support in the past few months. Thank you for always being there, and for helping me through many difficult times.

I would like to thank my committee members Dr. Matthew Golder, Dr. Dianne Xiao, and Dr. Corie Cobb for their support. Additionally, I would also like to thank Dr. Corie Cobb, along with other collaborators Dr. Haritz Sardon, Alex Gong, Dr. Nick Boechler, Dr. Lilo Pozzo, and

Dr. Luis Campos. Ultimately, it’s the collaboration with several other amazing researchers that drive each project to completion. I would also like to thank my mentors Li and TJ, along with other lab members at Meta Reality Labs, for an amazing internship experience which played a large part in shaping my views on research outside academia.

To my family and friends, I love and appreciate all of you. Emily, thank you for always being up to hang out, eat lunch, and explore new cafes. Savannah and Quoc, I cherish our friendship and really enjoyed all the times that you have visited me. To my American family, mom, Kate, and Sarah, thank you for giving me a home away from home. Mom, thank you for your support, love, and many words of wisdom. To my Thai family, mommy and Kristina (Godzi), thank you for being supportive in my decision to come study in the States. Thank you for visiting me many times, sending me Thai goodies and snacks, the video calls that keep me connected. Godzi, thank you for being there for me when things get rough, and for teaching and coaching me through the years. You are my sister, role model, and main pillar of support.

Last but not least, I would like to thank my husband Vincent. Fate has brought us together, and you have been my new home. During rough times, you have been my strength, reminding me to believe in myself and fight through. You have given me a reason to be excited about life, but you have also kept me grounded. I am very proud of you, and I am proud of us. We’ve been through so many highs and lows together, and I am looking forward to watching us grow alongside each other. None of this would have happened without you, and I am the luckiest person to have you as partner and best friend.

CHAPTER 1: **INTRODUCTION**

1.1 INTRODUCTION TO ADDITIVE MANUFACTURING AND 4D PRINTING

In recent decades, additive manufacturing (AM), popularly referred to as 3D printing, has seen an explosion in popularity, growth, and development. AM is an emerging manufacturing process of building a material up in a layer-by-layer fashion with precise 3-dimensional control.[1] Compared to traditional manufacturing methods, such as subtractive manufacturing or injection molding, AM offers advantages such as faster production time and conservation of materials and parts.[2] While subtractive manufacturing or machining requires a block of material at the start of the process, where materials are removed (as waste) until the desired shape is achieved, AM only requires amounts of materials close to the end product. In contrast to injection molding that requires additional manufacturing steps where molds need to be made each time specifications of the product change, AM can create different product shapes by simply altering the structure on the CAD model.[3] AM offers simplification to the manufacturing process, as well as allows creation of complex structures that were no achievable in the past in a less wasteful manner (Figure 1.1).[4,5]

The development of AM technology can be divided into 3 subsets. The first is the hardware, or the printers themselves. 3D printers started off as large, expensive machines in industrial settings for prototyping purposes. Nowadays, there is a wide variety of affordable printers that can be used by anyone to create 3D printed parts. The increased accessibility to 3D printers lead many to believe that 3D printing will be a key driving force to the next industrial revolution, where anyone can customize and manufacture parts in the comforts of their own homes.[6,7] The second field of AM development is the software and CAD modeling. Similar to the first subset, through computer-aided design/computer-aided manufacturing (CAD/CAM) software for AM has become more user-friendly to most, and the complexity of the structures created by the software has no limitation other than "our own imagination". Lastly, the third subset is the materials. Currently materials for AM are materials initially designed for traditional manufacturing methods, simply altered to be printable. In order to unlock the full potential of AM, materials that are designed specifically for AM are still needed.

To add functionality and increase impact of 3D printed devices, we can add a fourth dimension of time (4D printing) to increase the complexity of the printed part, which can be achieved by using stimuli-responsive materials. Stimuli-responsive materials exhibit property changes, whether mechanical properties, shape, or color when exposed to a stimulus.[8] Common stimuli include temperature, pH, electromagnetic field, and introduction of a chemical compound, which can modify the chemical interactions within the material, leading to the change in properties. Successful development of printable stimuli-responsive materials is critical for applications in 4D printing. 4D printing will allow us to create structures and exploit their stimuli-responsive to do mechanical work, record data, and actuate, impacting the fields of soft robotics, sensors, and biomedical devices (Figure 1.2).

1.2 HYDROGELS AS SOFT, STIMULI-RESPONSIVE MATERIALS FOR AM

Hydrogels are polymer networks swollen in a large amount of water. The polymers are hydrophilic and crosslinked through covalent, hydrogen, or ionic bonds, physical entanglements, or other dipolar interactions. The polymers and monomers can be either natural or synthetic.[9,10] While natural polymers have better biocompatibility and biodegradability, synthetic polymers have emerged as a promising solution to precisely control the interactions between the polymer chains and solvent. The softness, biocompatibility, and flexibility (similar to human tissues), allow hydrogels to be used as implants in a noninvasive fashion or used as a contact layer in wearable devices with increased comfort.[11] AM of hydrogels' biggest impact is seen in tissue engineering applications to create complex tissue scaffolds and organ grafts that can be patient-specific. Creating tissue scaffolds holds great promise in facilitating new tissue regeneration and material biodegradation.[4,12,13]

Additionally, the self-assembly of a polymer within an aqueous medium, driven by molecular interactions of polymer functional groups can lead to a stimuli-response.[14] Stimuli-responsive hydrophilic polymers, such as thermoresponsive poly(N-isopropylacrylamide) (pNIPAM), poly(vinyl methyl ether) (pVME), or pH-responsive poly(2-hydroxyethyl methacrylate–ethylene glycol dimethacrylate) (p(HEMA–EDMA)), are common examples of polymer choices for creating stimuli-responsive hydrogels.[15] Thermoresponsive block copolymers with lower critical solution temperature (LCST) behavior exhibits sol-gel transitions that have been extensively studied for drug delivery applications.[16,17] For hydrogels, stimuli such as pH change and chemical compounds can easily be diffused throughout the aqueous environment surrounding and inside the material, allowing for uniform changes in the material properties throughout the entire structure in a controllable manner. Conformation changes of the polymer chains lead to volume changes that alter shape, refractive index, elastic modulus, permeability, interfacial tension, or adhesion.[18,19] Despite the advances in stimuli-responsive hydrogels, the lack of gels with good printability, shape integrity, and mechanical properties has been a major drawback in the rapid advancement of this field.[4]

A significant limitation of hydrogels is the environmental control required to maintain steady-state hydration. In non-hydrated environments, they can dry out under ambient conditions, which limits their operational use.[20,21] When submerged in water, hydrogels will swell to their maximum water capacity. Swollen or dried out hydrogels can have substantially different mechanical and chemical properties compared to the initial material.[22,23] Any additives introduced to hydrogel need to be hydrophilic or soluble, to avoid settling issues (Figure 1.3). Furthermore, there is also a limitation with stimuli-responsive hydrogels. Changes are typically slow, as they are often limited by the diffusion rate.

1.3 ION GELS AS ALTERNATIVE SOFT MATERIALS FOR AM

Ion gels are polymer networks swollen with ionic liquids that have emerged as a promising alternative material for printable stimuli-responsive materials. An ionic liquid (IL) is made of an organic cation and either an organic or inorganic anion (Figure 1.4).[24] The size and bulkiness of the ions prevents crystalline packing, allowing these salts to exist as liquids at temperatures below 100 °C. Replacing water in hydrogels with ionic liquids offers advantages such as the thermal and chemical stability, negligible vapor pressure, and outstanding ability to solubilize organic, inorganic, and organometallic additives.[25,26] IL's ability to dissolve a wide variety of compounds allows possibility of incorporating new additives and polymers that previously had solubility issues in hydrogels or water, while the gels retain similar softness and fluidity. Their thermal stability and low vapor pressure allows ion gels to operate without concerns of drying out. Ion gels that can be printed will open new opportunities for facile fabrication of stimuli-responsive objects that can operate in a wide range of thermal and pressure conditions.[27] Due to its low volatility, thermal stability, and flame retardancy, many have exploited the advantages offered by ion gels to develop safer solid electrolytes for batteries, sensors, actuators, and biomedical devices.[28] In recent works on ion gels, ILs were used as the dispersed phase, polymerized into the continuous phase (ionoelastomer), or both.[24]

Various types of stimuli-responsive ion gels have been developed. The functionalities obtained may result from the intrinsic properties of the IL, from the interaction within the polymer, or between IL with polymers.[28] Electrochromic ion gels have the ability to alter their optical properties upon application of electrical potential.[29] Watanabe, *et al.* demonstrated thermo- and photoresponse behavior of a random copolymer consisting of N-isopropylacrylamide and 4-phenylazophenyl methacrylate in IL 1-butyl-3-methylimidazolium hexafluorophosphate, leading to solubility and upper critical solution temperature (UCST)-type transitions.[30] ILs generally exhibit a wide electrochemical window[31–33] , allow higher voltages to be applied in electrically responsive devices without risking side redox reactions. Their high thermal stability, nonvolatility, and good affinity with polar gases makes ion gels attractive for gas separation.[34,35] Ion gels can capture gases via hydrogen bonding and van der Waals interaction, and the resulting changes in conductivity and viscosity can be exploited to detect gas capture.[36] Another advantage of using ion gels is the vast number of ILs available, due to the limitless number of cation and anion combinations.[37]

1.4 DESIGNING SHEAR-THINNING GEL INKS AND POST PROCESSING METHODS FOR DIW AM

According to the American Society of Testing and Materials (ASTM) and International Organization of Standardization (ISO), AM is divided into 7 printing techniques: binder jetting, material jetting, powder bed fusion, directed energy deposition, sheet lamination, material extrusion, and VAT photopolymerization.[38–40] In comparison to other printing techniques, material extrusion offers advantages such as use of less material and relatively low cost of the printers.[6] Material extrusion can be sub-divided into 2 categories: fused deposition modeling (FDM) and direct-ink-writing (DIW). In FDM, a thermoplastic filament is heated above their glass transition temperature (T_g) or melting temperature (T_m) and the semi-liquid melted state is extruded onto the print bed or on top of an existing layer. As each layer is deposited and cooled individually, the weak mechanical properties resulting from interlayer defects and the limited option of thermoplastic materials are the main drawbacks in FDM (Figure 1.5a).[7,41,42]

DIW printing involves application of pressure to extrude a viscoelastic ink, which experiences a decrease in viscosity upon application of shear stress (Figure 1.5b). Once deposited, the ink solidifies through reduction in stress, use of a support bath, phase change, coagulation in contact with a nonsolvent, solvent evaporation, or polymerization.[43] DIW has become an effective and facile fabrication method for gels, due to the diversity of gels options with suitable viscoelastic and shear-thinning properties. Gel that are self-supporting (ink solidifies upon reduction in stress) have become a popular option as the printing is performed in air without the need to solidify the filament after extrusion. Popular materials used to create self-supporting inks include Pluronic F127 and nanoclay[44], which can modify the rheological properties of the gels.

Pluronic F127-based hydrogels have been regarded as the gold standard of a self-supporting, extrudable gel and used in our lab to design hydrogels for DIW printing.[45–47] Pluronic F127 is a commercially available ABA triblock copolymer made up of a center poly(propylene oxide) (PPO) ‘B’ block and two flanking, hydrophilic poly(ethylene oxide) (PEO) ‘A’ blocks (Figure 1.6a). When dissolved in aqueous solution, the hydrophobic nature of the PPO block causes the polymer to self-assemble into micelles, where the PPO core is surrounded by the PEO corona to minimize exposure to water.[48] The formation of micelles is temperature-dependent, and the polymers exhibit a lower critical solution temperature (LCST)-type behavior. The LCST response arises from the temperature-dependent solubility of the polymer, expressed by Gibb’s free energy of mixing, in the Gibbs−Helmholtz equation (Equation 1):

$$\Delta G_{mix} = \Delta H_{mix} - T\Delta S_{mix} \qquad (1)$$

where a negative ΔH_{mix} represents the favorable enthalpically mixed state due to hydrogen bonding between water and the PEO blocks. A negative ΔS_{mix} represents the entropically unfavorable mixed state due to the water molecules forming an ordered layer surrounding the hydrophobic PPO chain. On one hand, at low temperatures (small T), $-\Delta H_{mix}$ plays the dominant role that results in favorable polymer solubility, $-\Delta G_{mix}$. On the other hand, a higher temperature (increasing T) increases the contribution of $T\Delta S_{mix}$, ultimately leading to unfavorable solubility that drives the polymer to self-assemble into micelles[49,50] (Figure 1.6b).

At concentrations above 20 wt%, the micelles can pack into crystallize BCC lattice, leading to gelation.[51] The packed micelles are held together by weak intermolecular forces, which can be easily disrupted with application of force. Once disrupted, the micelles can slide past each other, allowing the hydrogel to flow.[52] This behavior leads to the hydrogel's shear-thinning ability, as the material yields when stress is applied (Figure 1.6c). The flow behavior of the inks can be described by the Herschel-Bulkley model (Equation2):

$$\tau = \tau_y + K\dot{\gamma}^{\mathrm{n}} \tag{2}$$

Where τ is the shear stress, K the consistency index, $\dot{\gamma}$ is the shear rate, and n is the flow index ($n < 1$ for shear-thinning fluids). During printing, the applied shear stress must exceed the yield stress for the material to extrude. Upon exiting the nozzle, the material's τ will recover to its yield stress τ_y.[2] Therefore, the yield stress of the material is an important parameter for good printability and self-supporting ability. If τ_y is too high, the printer needs to exert a large amount of pressure to be able to extrude the material. If too low, the recovered material will not be robust enough for have good shape integrity or be able to hold the load applied by materials printed on top. The yield stress of the material can be studied through rheology, and materials with higher yield stress showed printed filaments that are more uniform and closer in geometry to the nozzle.[45]

Today, the majority of AM printed parts still have inferior mechanical properties and anisotropy introduced during the layer-by-layer process and incomplete polymerization of inks and resins that limit their potential applications.[7,53] Therefore, most printed structures require additional processes beyond the AM step to create functional and working devices. When using a self-supporting gel like F127 hydrogels to print, the entire structure can be printed first before the next post-processing step. One method of post-processing a material is via thermal or photo-curing that induces additional crosslinking of the material.[54] This step can increase the cohesion across layer boundaries to reduce interlayer defects.[55] Curing plays a large role in the final mechanical properties of the printed structure, as many have demonstrated discrepancies in flexural strength, flexural modulus, and dimensional accuracy when using different curing machines. Furthermore, the curing process also influences the degree of conversion, which can affect leaching of monomer and ultimately the biocompatibility of the printed structure.[56,57] Our lab has modified the chain ends of F127 to contain bisurethane methacrylate groups (creating F127-BUM), which allows the hydrogel to undergo post-print crosslinking via UV curing to fix the printed structures and increase its mechanical robustness (Figure 1.6d).[58–60] While UV curing is fast and facile, there are disadvantages such as UV degradation and insufficient penetration through thick or opaque materials.[61] Although thermal annealing is an alternative option, using heat can dehydrate materials such as hydrogels. With limitations of current post-processing methods, new methods are needed to optimize and improve the AM manufacturing process.

1.5 CONCLUSION

The following chapters will discuss the design and development of a stimuli responsive ion gels and hydrogels for DIW AM of functional devices. Chapter 2 introduces a novel ion gel that can be used to print 3-dimensional structures without needing to cure between layers or printed onto a nonsolvent for coagulation, enabling creating of complex auxetic sensors that have enhanced stretchability through structural design. Chapter 3 builds on this platform by introducing a polymerizable group to the ionic liquids to create a continuous network ionoelastomer, which exhibits tunable shape memory behavior, allowing for printing of structures that exhibit programmable, multi-directional bending upon mechano-activation. Finally, chapter 4 investigates a current problem with photopolymerization methods in 3D printing and suggests a solution that allows 3D printing and post-print photocuring of thick and opaque hydrogels.

1.6 REFERENCES

(1) Jandyal, A.; Chaturvedi, I.; Wazir, I.; Raina, A.; Ul Haq, M. I. 3D printing –A review of processes, materials and applications in industry 4.0. *Sustainable Operations and Computers* **2022**, *3*, 33–42.

(2) Truby, R. L.; Lewis, J. A. Printing soft matter in three dimensions. *Nature* **2016**, *540*, 371–378.

(3) Shahrubudin, N.; Lee, T. C.; Ramlan, R. An Overview on 3D Printing Technology: Technological, Materials, and Applications. *Procedia Manufacturing* **2019**, *35*, 1286–1296.

(4) Li, J.; Wu, C.; Chu, P. K.; Gelinsky, M. 3D printing of hydrogels: Rational design strategies and emerging biomedical applications. *Mater. Sci. Eng. R Rep.* **2020**, *140*, 100543.

(5) Zhou, L. Y.; Fu, J.; He, Y. A Review of 3D Printing Technologies for Soft Polymer Materials. *Adv. Funct. Mater.* **2020**, *30*, 2000187.

(6) Jiang, Z.; Diggle, B.; Tan, M. L.; Viktorova, J.; Bennett, C. W.; Connal, L. A. Extrusion 3D Printing of Polymeric Materials with Advanced Properties. *Adv. Sci.* **2020**, *7*, 2001379.

(7) Ngo, T. D.; Kashani, A.; Imbalzano, G.; Nguyen, K. T. Q.; Hui, D. Additive manufacturing (3D printing): A review of materials, methods, applications and challenges. *Composites Part B* **2018**, *143*, 172–196.

(8) Lee, J. Y.; Jia An, J.; Chua, C. K. Fundamentals and applications of 3D printing for novel materials. *Appl. Mater. Today* **2017**, *7*, 120–133.

(9) Koetting, M. C.; Peters, J. T.; Steichen, S. D; Peppas, N. A. Stimulus-responsive hydrogels: Theory, modern advances, and applications. *Mater. Sci. Eng. R Rep.* **2015**, *93*, 1–49.

(10) Yoon, C. K.; Xiao, R.; Park, J.; Cha, J.; Nguyen, T. D.; Gracias, D. H. Functional stimuli responsive hydrogel devices by self-folding. *Smart Mater. Struct.* **2014**, *23*, 094008.

(11) Ge, G.; Wang, Q.; Zhang, Y. Z.; Alshareef, H. N.; Dong, X. 3D Printing of Hydrogels for Stretchable Ionotronic Devices. *Adv. Funct. Mater.* **2021**, *31*, 2107437.

(12) Highley, C. B.; Rodell, C. B.; Burdick, J. A. Direct 3D Printing of Shear-Thinning Hydrogels into Self-Healing Hydrogels. *Adv. Mater.* **2015**, *27*, 5075–5079.

(13) Chimene, D.; Lennox, K. K.; Kaunas, R. R.; Gaharwar, A. K. Advanced Bioinks for 3D Printing: A Materials Science Perspective. *Ann Biomed Eng* **2016**, *44*, 2090–2102.

(14) Zhang, X. N.; Zheng, Q.; Wu, Z. L. Recent advances in 3D printing of tough hydrogels:

A review. *Composites Part B* **2022**, *238*, 109895.

(15) Zhang, D.; Ren, B.; Zhang, Y.; Xu, L.; Huang, Q.; He, Y.; Li, X.; Wu, J.; Yang, J.; Chen, Q.;Chang, Y.; Zheng, J. From design to applications of stimuli-responsive hydrogel strain sensors. *J. Mater. Chem. B* **2020**, *8*, 3171–3191.

(16) Chatterjee, S.; Hui, P. C. Review of Applications and Future Prospects of Stimuli-Responsive Hydrogel Based on Thermo-Responsive Biopolymers in Drug Delivery Systems. *Polymers* **2021**, *13*, 2086.

(17) Sood, N.; Bhardwaj, A.; Mehta, S.; Mehta, A. Stimuli-responsive hydrogels in drug delivery and tissue engineering. *Drug Deliv*. **2016**, *23*, 748–770.

(18) Ahn, S.; Kasi, R. M.; Kim, S.; Sharmaa, N.; Zhou, Y. Stimuli-responsive polymer gels. *Soft Matter* **2008**, *4*, 1151–1157.

(19) Tokarev, I.; Minko, S. Stimuli-responsive hydrogel thin films. *Soft Matter* **2009**, *5*, 511–524.

(20) Mredha, T. I.; Le, H. H.; Cui, J.; Jeon, I. Double-Hydrophobic-Coating through Quenching for Hydrogels with Strong Resistance to Both Drying and Swelling. *Adv. Sci.* **2020**, *7*, 1903145.

(21) Calvert, P. Hydrogels for Soft Machines. *Adv. Mater.* **2009**, *21*, 743–756.

(22) Abd Alla, S. G.; Sen, M.; El-Naggar, A. W. M. Swelling and mechanical properties of superabsorbent hydrogels based on Tara gum/acrylic acid synthesized by gamma radiation. *Carbohydr. Polym.* **2012**, *89*, 478–485.

(23) Omidian, H.; Park, K. Introduction to Hydrogels. In *Biomedical Applications of Hydrogels Handbook*. Springer, 2010, pp 1–16.

(24) Gao, Y. R.; Cao, J. F.; Shu, Y.; Wang, J. H. Research progress of ionic liquids-based gels in energy storage, sensors and antibacterial. *GreenChE* **2021**, *2*, 368–383.

(25) Nulwalaa, H.; Mirjafaric, A.; Zhou, X. Ionic liquids and poly(ionic liquid)s for 3D printing – A focused mini-review. *Eur. Polym. J.* **2018**, *108*, 390–398.

(26) Lu, J.; Yan, F.; Texter, J. Advanced applications of ionic liquids in polymer science. *Prog. Polym. Sci.* **2009**, *34*, 431–448.

(27) Ueki, T. Stimuli-responsive polymers in ionic liquids. *Polym. J.* **2014**, *46*, 646–655.

(28) Correia, D. M.; Fernandes, L. C.; Martins, P. M.; García-Astrain, C.; Costa, C. M.; Reguera, J.; Lanceros-Méndez, S. Ionic Liquid–Polymer Composites: A New Platform for Multifunctional Applications. *Adv. Funct. Mater.* **2020**, *30*, 1909736.

(29) Moon, H. C.; Lodge, T. P.; Frisbie, C. D. Solution Processable, Electrochromic Ion Gels for Sub 1 V, Flexible Displays on Plastic. *Chem. Mater.* **2015**, *27*, 1420−1425.

(30) Ueki, T.; Nakamura, Y.; Lodge, T. P.; Watanabe, M. Light-Controlled Reversible

Micellization of a Diblock Copolymer in an Ionic Liquid. *Macromolecules* **2012**, *45*, 7566−7573.

(31) Hanabusa, K.; Fukui, H.; Suzuki, M.; Shirai, H. Specialist Gelator for Ionic Liquids. *Langmuir* **2005**, *21*, 23, 10383–10390.

(32) Singh, V. V.; Nigam, A. K.; Batra, A.; Boopathi, M.; Singh, B.; Vijayaraghavan, R. Applications of Ionic Liquids in Electrochemical Sensors and Biosensors. *Int. J. Electrochem. Sci.* **2012**, *607*, 165683.

(33) Lu, W.; Henry, K.; Turchi, C.; Pellegrino, J. Incorporating Ionic Liquid Electrolytes into Polymer Gels for Solid-State Ultracapacitors. *J. Electrochem. Soc.* **2008**, *155*, A361.

(34) Gu, Y.; Lodge, T. P. Synthesis and Gas Separation Performance of Triblock Copolymer Ion Gels with a Polymerized Ionic Liquid Mid-Block. *Macromolecules* **2011**, *44*, 1732–1736.

(35) Sasikumara, B.; Arthanareeswarana, G.; Ismail, A. F. Recent progress in ionic liquid membranes for gas separation. *J. Mol. Liq.* **2018**, *266*, 330–341.

(36) Cui, J.; Li, Y.; Chen, D.; Zhan, T.; Zhang, K. *Adv. Funct. Mater.* **2020**, *30*, 2005522.

(37) Li, Y.; Zhang, C.; Zhou, Y.; Dong, Y.; Chen, W. Novel multi-responsive polymer materials: When ionic liquids step in. *Eur. Polym. J.* **2015**, *69*, 441–448.

(38) Salmi, M. Additive Manufacturing Processes in Medical Applications. *Materials* **2021**, *14*, 191.

(39) Singh, T.; Kumar, S.; Sehgal, S. 3D printing of engineering materials: A state of the art review. *Materials Today: Proceedings* **2020**, *28*, 1927–1931.

(40) Tan, L. J.; Zhu, W.; Zhou, K. Recent Progress on Polymer Materials for Additive Manufacturing. *Adv. Funct. Mater.* **2020**, *30*, 2003062.

(41) Wang, P.; Zhou, B.; Ding, S.; Li, L.; Huang, C. Effects of FDM-3D printing parameters on mechanical properties and microstructure of CF/PEEK and GF/PEEK. *CJA* **2021**, *34*, 236–246.

(42) Levenhagen, N. P.; Dadmun, M. D. Improving Interlayer Adhesion in 3D Printing with Surface Segregating Additives: Improving the Isotropy of Acrylonitrile–Butadiene–Styrene Parts. *ACS Appl. Polym. Mater.* **2019**, *1*, 876–884.

(43) Ilbey, I.; Lin, L. 3D printing technologies: techniques, materials, and post-processing. *Curr. Opin. Chem. Eng.* **2020**, *28*, 134–143.

(44) Chen, Z.; Zhao, D.; Liu, B.; Nian, G.; Li, X.; Yin, J.; Qu, S.; Yang, W. 3D Printing of Multifunctional Hydrogels. *Adv. Funct. Mater.* **2019**, *29*, 1900971.

(45) Smith, P. T.; Basu, A.; Saha, A.; Nelson, A. Chemical modification and printability of shear-thinning hydrogel inks for direct-write 3D printing. *Polymer* **2018**, *152*, 42–50.

(46) Saha, A.; Johnston, T. G.; Shafranek, R. T.; Goodman, C. J.; Zalatan, J. G.; Storti, D. W.; Ganter, M. A.; Nelson, A. Additive Manufacturing of Catalytically Active Living Materials. *ACS Appl. Mater. Interfaces* **2018**, *10*, 13373−13380.

(47) Narupai, B.; Smith, P. T.; Nelson, A. 4D Printing of Multi-Stimuli Responsive Protein-Based Hydrogels for Autonomous Shape Transformations. *Adv. Funct. Mater.* **2021**, *31*, 2011012.

(48) Thomas, S. S.; Hosseini-Nejad, H.; Bohne, C. Dynamics of small molecules within the F127 PEO–PPO–PEO triblock copolymer gel and sol phases studied at the molecular scale. *Soft Matter*, **2022**, *18*, 1706–1714.

(49) Pardeshi, S.; Damiri, F.; Zehravi, M.; Joshi, R.; Kapare, H.; Prajapati, M. K.; Munot, N.; Berrada, M.; Giram, P. S.; Rojekar, S.; Ali, F.; Rahman, H.; Barai, H. R. Functional Thermoresponsive Hydrogel Molecule to Material Design for Biomedical Applications. *Polymers* **2022**, *14*, 3126.

(50) Matthes, R.; Frey, H. Polyethers Based on Short-Chain Alkyl Glycidyl Ethers: Thermoresponsive and Highly Biocompatible Materials. *Biomacromolecules* **2022**, *23*, 2219−2235.

(51) Mortensen, K.; Batsberg, W.; Hvidt, S. Effects of PEO-PPO Diblock Impurities on the Cubic Structure of Aqueous PEO-PPO-PEO Pluronics Micelles: fcc and bcc Ordered Structures in F127. *Macromolecules* **2008**, *41*, 1720-1727.

(52) Walza, M.; Magerla, A.; Wolff, M.; Zabel, H. Structure and texture of micelles under shear. *Superlattices and Microstructures* **2007**, *41*, 185–189.

(53) Cingesar, I. K.; Marković, M.-P.; Domagoj Vrsaljko, D. Effect of post-processing conditions on polyacrylate materials used in stereolithography. *Addit. Manuf.* **2022**, *55*, 102813.

(54) Karakurt, I.; Lin, L. 3D printing technologies: techniques, materials, and post-processing. *Curr. Opin. Chem. Eng.* **2020**, *28*, 134–143.

(55) Ao-Ieong, W. S.; Chien, S. T.; Jiang, W. C.; Yet, S. F.; Wang, J. The Effect of Heat Treatment toward Glycerol-Based, Photocurable Polymeric Scaffold: Mechanical, Degradation and Biocompatibility. *Polymers* **2021**, *13*, 1960.

(56) Piedra-Cascón, W.; Krishnamurthy, V. R.; Att, W.; Revilla-Léon, M. 3D printing parameters, supporting structures, slicing, and post-processing procedures of vat-polymerization additive manufacturing technologies: A narrative review. *J. Dent.* **2021**, *109*, 103630.

(57) Urrios, A.; Parra-Cabrera, C.; Bhattacharjee, N.; Gonzalez-Suarez, A. M.; Rigat-Brugarolas, L. G.; Nallapatti, U.; Samitier, J.; DeForest, C. A.; Posas, F.; Garcia-Corderob, J. L.; Folch, A. 3D-printing of transparent bio-microfluidic devices in PEG-DA. *Lab Chip* **2016**, *16*, 2287–2294.

(58) Karis, D. G.; Nelson, A. Time-dependent covalent network formation in extrudable

hydrogels. *Polym. Chem.* **2020**, *11*, 6910–6918.

(59) Johnston, T. G.; Yuan, S.; Wagner, J. M.; Yi, X.; Saha, A.; Smith, P. T.; Nelson, A.; Alper, H. S. Compartmentalized microbes and co-cultures in hydrogels for on-demand bioproduction and preservation. *Nat. Commun.* **2020**, *11*, 563.

(60) Millik, S. C.; Dostie, A. M.; Karis, D. G.; Smith, P. T.; McKenna, M.; Chan, N.; Curtis, C. D.; Nance, E.; Theberge, A. B.; Nelson, A. 3D printed coaxial nozzles for the extrusion of hydrogel tubes toward modeling vascular endothelium. *Biofabrication* **2019**, *11*, 045009.

(61) Taormina, G.; Sciancalepore, C.; Messori, M.; Bondioli, F. 3D printing processes for photocurable polymeric materials: technologies, materials, and future trends. *JABFM* **2017**, *16*, 151–160.

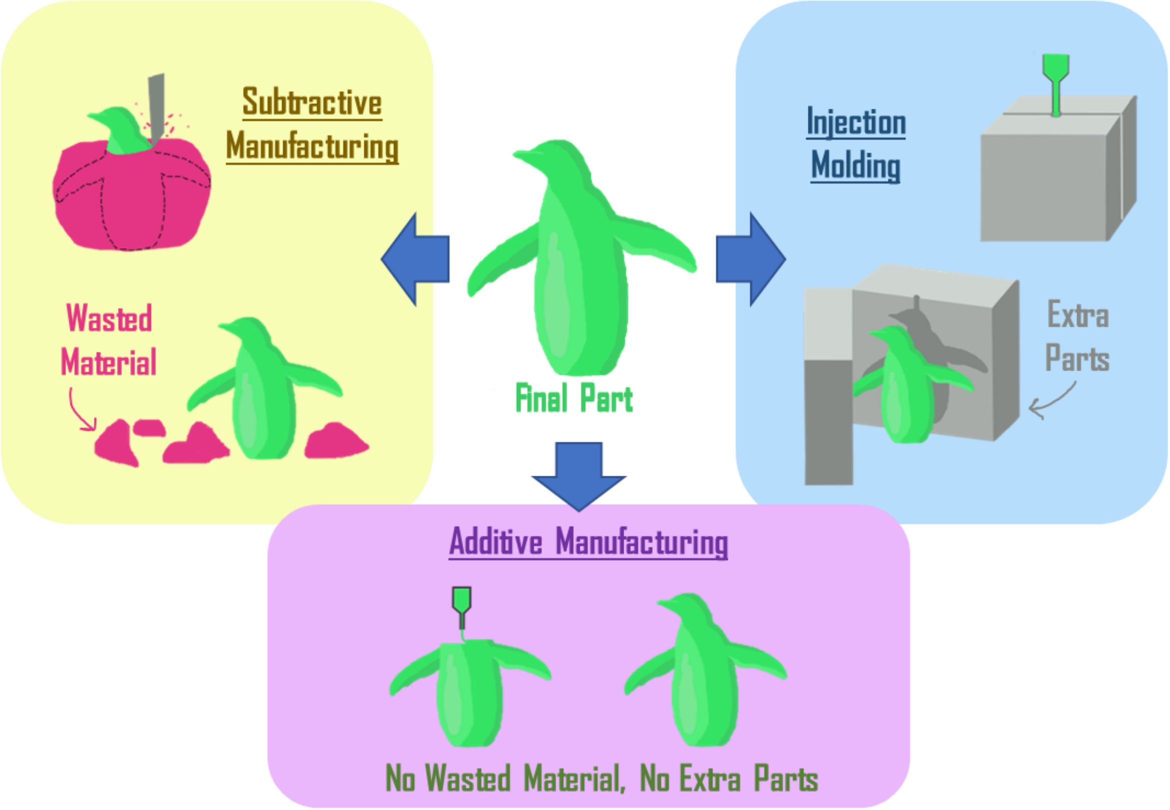

Figure 1.1 Comparison between subtractive manufacturing, injection molding, and additive manufacturing. Additive manufacturing uses less materials and does not require additional parts such as molds.

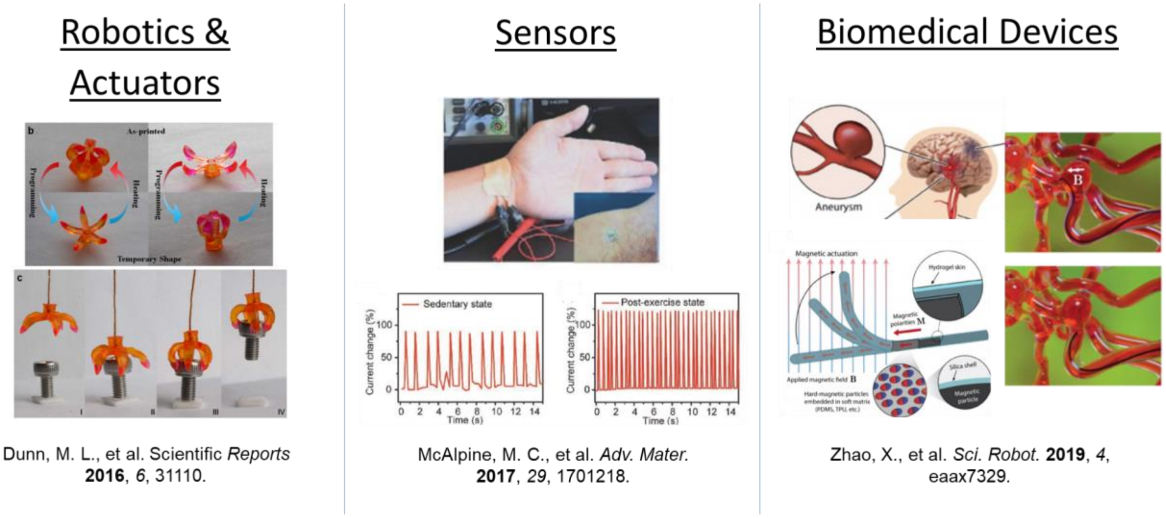

Dunn, M. L., et al. Scientific *Reports* **2016**, *6*, 31110.

McAlpine, M. C., et al. *Adv. Mater.* **2017**, *29*, 1701218.

Zhao, X., et al. *Sci. Robot.* **2019**, *4*, eaax7329.

Figure 1.2 Examples for stimuli-responsive materials and their applications. From left to right: a thermo-responsive gripper that can be used to do mechanical work, a sensor the converts biopotentials to electrical signals that can be read and recorded, and a rod that changes shape according to an applied magnetic field that can be used as a biomedical device to navigate through blood vessels and remove clots caused by aneurysms.

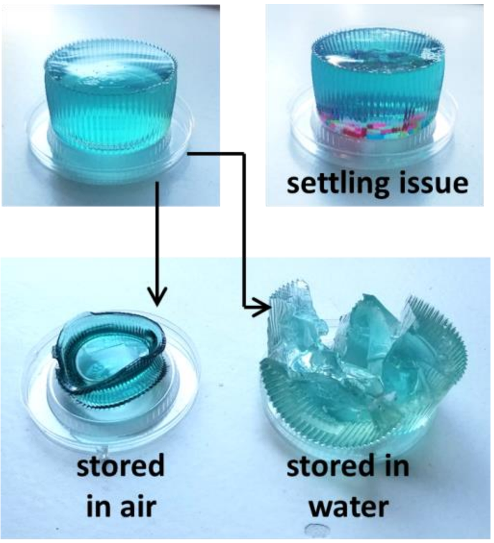

Figure 1.3 Limitations with using hydrogels. When using hydrogel, additives must be water-soluble to avoid settling issues. Hydrogels dry out in ambient conditions, and swell to their maximum capacity when submerged in water. As a result, the mechanical properties are significantly different compared to the hydrogel when it was first made.

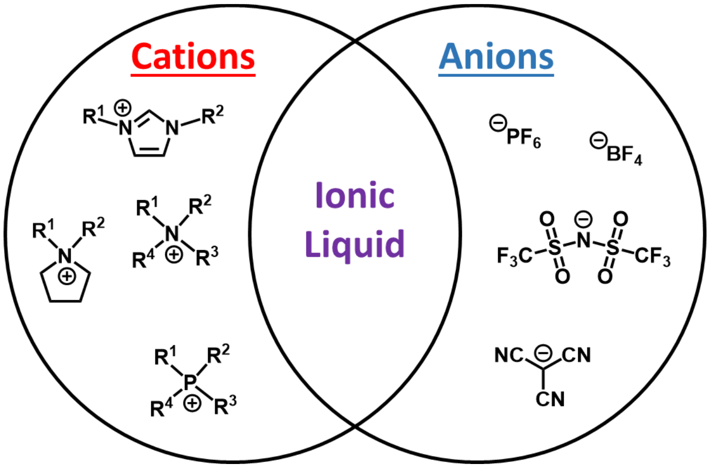

Figure 1.4 Examples of ionic liquids. An ionic liquid is a combination of an organic cation and an organic or inorganic anion.

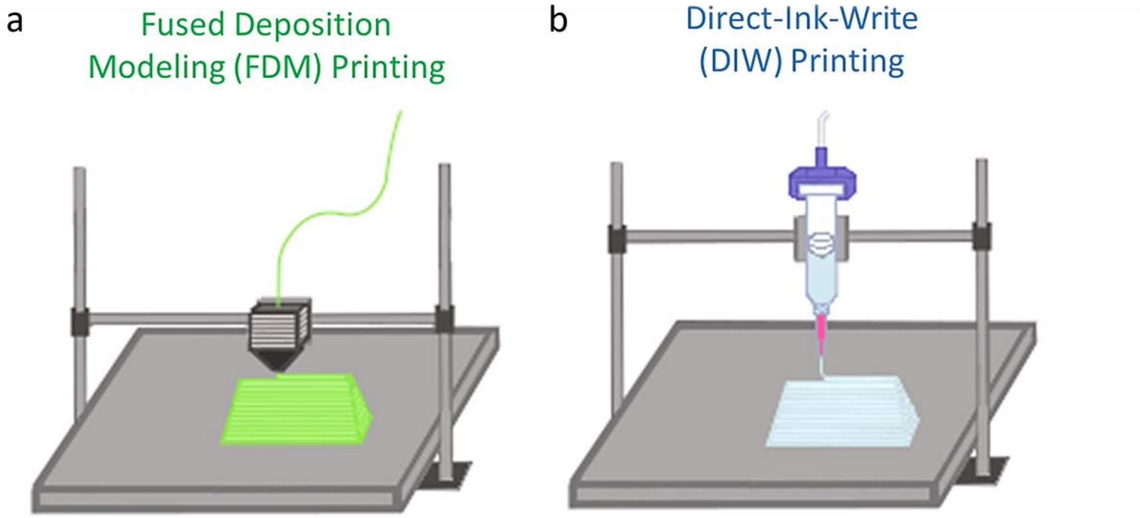

Figure 1.5 Comparison between FDM and DIW printing. a) FDM involves using heat to extrude thermoplastics in its semi-liquid state, and the filaments solidify upon cooling. b) DIW uses viscoelastic shear-thinning inks that can be extruded with application of pneumatic pressure or shear force. Self-supporting viscoelastic inks can solidify upon removal of force.

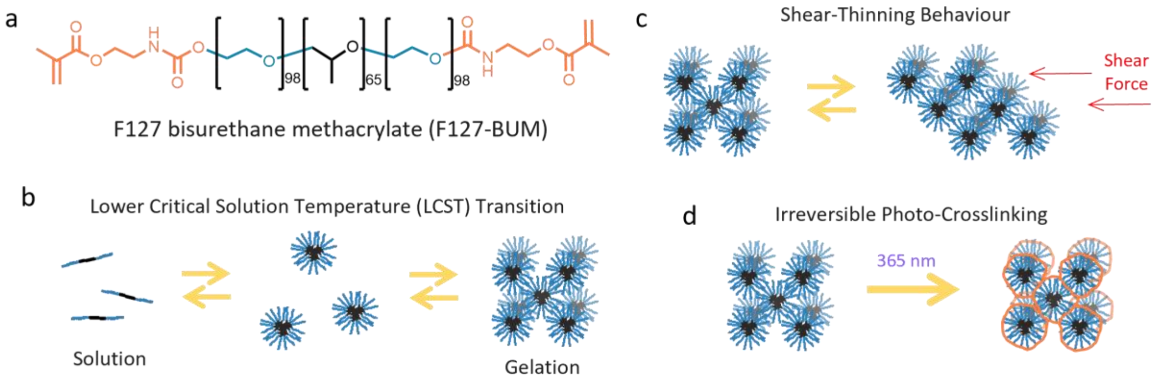

Figure 1.6 Pluronic F127, chemical structure shown in (a) is a triblock copolymer that forms a gel at concentrations above 20 wt%. The gel exhibits a lower critical solution temperature transition (b) and shear-thinning behavior (c). The addition of the bisurethane methacrylate end groups allows the gel to under photopolymerization to crosslink the material (d).

CHAPTER 2: **3D PRINTING ION GEL AUXETIC FRAMEWORKS FOR STRETCHABLE SENSORS**

2.1 ABSTRACT

Ion gels are an emerging class of soft materials that exhibit ionic conductivity and thermal stability without the need to replenish ions or the addition of conductive particle fillers. An ion gel ink is reported for direct-write 3D printing to fabricate conductive structures that can vary in the printed object geometries. This approach relies on a shear-thinning ion gel ink that can be extruded to afford self-supporting constructs. After a brief UV cure, the printed construct is transformed into a mechanically tough, transparent structure that is ionically conductive. Upon application of stretching and twisting loads, the 3D-printed objects exhibit detectable changes in conductivity. To demonstrate the versatility of rapid prototyping with the ion gel inks, an auxetic structure is 3D printed and tested as a strain sensor. The printed auxetic structure exhibits an electrical response to strain, but also demonstrates increased extensibility and operational range in comparison to a casted bulk film with the same outer dimensions.

2.2 INTRODUCTION

Stretchable sensors hold great potential for wearable electronics[1–3], biomedical devices[4,5], and soft robotic applications.[6–7] In addition to their ability to convert physical variables such as motion, pressure, temperature, light and humidity, into electronic signals[8–13], stretchable sensors also conform to the target’s surface and undergo large amounts of strain without loss in performance, leading to higher sensitivity and operation range.[14] Stretchable sensors are typically comprised of a conductive fillers patterned onto, or encapsulated within, an insulating soft matrix such as a silicone.[15–18] However, the rigidity of the fillers and electrodes have limited performance and causes hysteresis over repeated deformation cycles. [19,20] While there is an ongoing search for new materials, achieving the required mechanical attributes through structural designs via 3D printing have emerged as an alternative solution.[19,21,22] 3D printing is an additive manufacturing process that enables the rapid fabrication and iteration of complex geometries for laboratory research[23–26] and commercial products.[27–29] Recent technological advancements and the commercial availability of low-cost 3D printers have driven the adoption of this technology. While 3D printing hardware and software has rapidly improved, there is a great need for new functional materials that are specifically designed for 3D printing stretchable sensors.[30,31]

Ion gels are polymer networks swollen with ionic liquids that have emerged as a promising solution to creating conductive materials for printing stretchable electronics. Although their ionic conductivity is generally lower than the values for salt hydrogels and hydrogels with conductive fillers, ionic liquids provide high thermal stability and negligible vapor pressure.[32–35] Hence, ion gels can retain their shape without the need to be stored in aqueous solution or replenished with fresh ions. Incorporating conductive particles such as graphene oxide and CNTs often cause turbidity[36] and require specialized processing methods to control particle homogeneity.[20,37–38] Recently, the 3D patterning of ion gels has been demonstrated with inkjet[39,40] and photolithographic techniques.[24,41–43] Gatenholm et al. demonstrated[44] an extrusion-based 3D printing of ion gels wherein the ink was comprised of cellulose dissolved in 1-ethyl-3-methylimidazolium acetate. However, this approach required printing onto a secondary gel that contained water as a nonsolvent for the ink to coagulate and form a structure post-printing. Thus, ionic liquid inks that facilitate extrusion printing without the use of additional support surfaces or vats could potentially improve feature resolution and expand the geometries that can be afforded.

Herein, we report the first shear-thinning ion gel ink designed for direct-write 3D printing conductive 3D constructs, including an auxetic strain sensor. The ion gel was comprised of F127 bisurethane methacrylate (F127-BUM) dissolved in 1-butyl-3-methylimidazolium tetrafluoroborate ([BMIM]BF_4) and a photo-radical generator (Figure 1a). The resulting gel was pneumatically extrusion-printed to afford a 3D construct. It was then exposed to UV irradiation to induce photo-radical polymerization and cross-linking of the polymer network.

2.3 MATERIALS AND METHODS

2.3.1 Materials

Pluronics® F127 (BioReagent), and 1-butyl-3-methylimidazolium tetrafluoroborate ([BMIM]BF_4, ≥98%) was purchased from MilliporeSigma. 2-isocyanatoethyl methacrylate (98%) was purchased from Arctom. Dibutyltin dilaurate (>95%) was purchased from TCI America. Ether and methanol (HPLC grade) were purchased from Fisher Scientific. All reagents were used as received. Anhydrous methylene chloride was obtained by purification over alumina column on a Pure Process Technology purification system.

2.3.2 F127-BUM Synthesis

Glassware was oven-dried at 125 °C for at least 16 h and F127 (60 g, 4.8 mmol) was dried under vacuum (~ 2 Pa) for at least 16 h at room temperature in a round-bottom flask. Anhydrous dichloromethane (550 mL) was charged to the flask under an N_2 atmosphere. The mixture was stirred at 30 °C, and following complete dissolution of the F127, dibutyltin dilaurate (12 drops) was added using a glass Pasteur pipette. The 2-isocyanatoethyl methacrylate (3.5 mL, 24.8 mmol) was diluted in anhydrous dichloromethane (50 mL) and added to the reaction mixture at a rate of approximately 1 drop/s. The reaction was left to stir under dry N_2 at 30 °C. After 2 d, the reaction was quenched by the addition of methanol (60 mL), and the mixture was concentrated at 30 °C using a rotary evaporator. F127-BUM was precipitated in diethyl ether (2000 mL). During the precipitation, ether was stirred in a large conical flask, and the concentrate was poured in slowly. The precipitate mixture was stirred for an additional 15 min before separation via centrifugation. Eight 50 mL centrifuge tubes were filled with precipitate mixture and centrifuged (3000 g) for approximately 10 min. The transparent supernatant in each tube was decanted, and more of the precipitate mixture was added on top of each pellet. This process was repeated until all of the precipitate had been collected in the eight centrifuge tubes, and all of the solvent had been discarded. The precipitate was then washed twice by adding diethyl ether (approximately 30 mL) to each pellet and vortex-mixing until redispersion of the precipitate was observed, followed by centrifugation (3000 g) for re-separation of the precipitate, and supernatants were again discarded. After washing, the F127-BUM from each tube was pooled and transferred to a large beaker. Excess ether was allowed to evaporate by agitating with a spatula under an N_2 atmosphere. The resultant F127-BUM powder was dried fully overnight at room temperature under vacuum (~ 2 Pa) and stored in the dark at 4 °C until further use.

2.3.3 Preparation of Ion Gel Inks

The ion gel with compositions of 27 wt % polymer were prepared by adding F127-BUM (0.81 g) to $[BMIM]BF_4$ (2.19 g). To encourage solubility of the polymer in IL, methanol (approx. 1.5 mL) was added, followed constant stirring at room temperature until a clear, transparent solution was obtained. The photoinitiator 2-hydroxy-2-methylpropiophenone (HMP, 3.0 μL) was then added via a volumetric pipette. The solution was then subjected to a short cycle of strong mechanical mixing, followed by removal of methanol in vacuo at 40 °C until a self-supporting gel was obtained. The gel was loaded onto a 3 cc syringe, capped and centrifuged to remove trapped bubbles. The cap was then removed and replaced with a 25 Ga Metcal extrusion nozzle (I.D. 0.26 mm).

2.3.4 Rheometrical Characterization

Rheometrical characterization was performed on a TA Instruments DHR-2 equipped with an Advanced Peltier Plate system and 365 nm LED UV-curing accessory. All rheometric experiments were performed using a stainless steel 8 mm upper plate. All gel samples were loaded onto a 3 cc syringe, centrifuged to remove any trapped bubbles, and left overnight to equilibrate. The sample was then loaded by extruding the gel onto the loading plate and trimmed after the upper plate was lowered to the trim gap at 600 µm. The geometry gap between upper and lower plates was then set to 500 µm for all experiments. For experiments involving the Peltier plate, a pre-shear was applied at 5 °C for 10 s before additional sample conditioning at 25 °C for 8 min. A 365 nm LED UV-curing accessory with disposable acrylic plates was used in the photorheology experiments.

2.3.5 DIW Printing of Ion Gels

DIW 3D printing was performed on a modified Alunar i3 RepRap extrusion printer that has been retrofitted for pneumatic dispensation. G-codes were written through text editor for the lines and star, while the cylinders, UW logo, and auxetic structure were originally created as a CAD file in SolidWorks 2018 and converted to G-codes via Slic3r. All printing was performed using the 27 wt% ion gel ink with an extrusion air pressure of 20 psi. The dimensions and print speeds for each structure in Figure 1c are as following: 1.5 cm line was printed at 10 mm/s, 1.3 cm diameter 5-pointed star was printed at 10 mm/s, the cylinders with diameter of 1 cm were printed at 6.5 mm/s, and the UW logo with W×H dimensions 7.0 × 2.5 cm was printed at 10 mm/s. These structures were printed with 0.3 mm layer height. The auxetic structure, with dimensions 4.5 × 7 cm, was printed with 0.25 mm layer height, 4 layers total, at 7 mm/s. Upon completion of the 3D printing, the structures were irradiated under 365 nm light (at 3.4 mW/cm^2) for 25 min to cross-link F127-BUM and chemically fix the structures.

2.3.6 Mechanical Characterization

An Instron 5585H 250 kN electro-mechanical test frame with a 50 N load cell was used to evaluate the tensile properties of the cross-linked ion gel. The ASTM D638 type V specimen specifications were used to prepare dogbone samples by transferring approximately 2 g to 27 wt% gel into a Teflon dogbone mold. The gel was then exposed to 365 nm light for 15 min. The chemically cross-linked structure was then removed from the mold, flipped and inserted back in. A small amount of gel was then used to fill any defects present, and the samples were cured for an additional 5 min. The sample was then placed on pneumatic self-aligning grips fixed on the load frame, and the sample was subjected to increasing strain at a constant rate of 10 mm/min until mechanical failure of the sample. The toughness was calculated by taking an integral to calculate the area under the stress-strain curve.

2.3.7 Conductivity Measurement

Ion gel samples for conductivity measurement were prepared by the same method described above. The ionogel was transferred into a silicone mold via solvent casting. The sample was first left under ambient conditions to allow the residual methanol to evaporate, and then placed under high vacuum at 60 ° C. Lastly, the film was exposed to a xenon arc lamp (Helios Italquartz, 45 $mW\cdot cm^{-2}$) in order to cross-link the material.

The ionic conductivity was studied by electrochemical AC impedance spectroscopy (EIS) with an Autolab 302N potentiostat galvanostat with temperature control attachment by a Microcell HC station. The cross-linked sample was placed between two stainless steel electrodes and sealed in a Microcell under argon atmosphere in a glove box (M-Braun) to avoid contact with moisture. The frequency range was set from 0.1 MHz to 0.1 Hz and applied amplitude was 10 mV. The surface area of the electrode was 0.5026 cm^2. The ionic conductivity was measured first at room temperature, followed by increments of 10 °C from 30 to 90 °C.

2.3.8 Thermogravimetric Analysis

The thermal stability of the cross-linked ion gel was determined by thermogravimetric analysis (TGA), which was carried out on a TA Q50 V20.13 Build 39 under N_2 atmosphere. A sample of the cross-linked ion gel (5.22300 mg) was placed onto a clean platinum pan. Starting at room temperature, the sample was then heated to 700 °C at a constant rate of 10 °C/min. The weight and derivative weight was then measured as a function of time (Figure S6).

2.3.9 Initial Evaluation of Soft Sensors

Changes in the conductivity of films and printed structures were recorded by applying a constant potential across the cross-linked samples and measuring the resulting change in current due to stretching and twisting motions. A DAGAN Chem Clamp N = 1 headstage was used to apply the potential and measure the current for the smaller dimension films (1 × 2.5 cm), while a DAGAN Chem Clamp N = 0.01 headstage was used to measure the larger dimension films (4.5 × 7 cm) and 3D-printed auxetic structures. The N = 0.01 headstage has a higher current threshold to accommodate the larger background currents of the larger dimension films and 3D printed auxetic structures. +300 mV was applied to the smaller dimension films and auxetic structure, while +40 mV was applied to the larger dimension gels.

The smaller films were clamped between alligator clips on opposing sides of the film, as shown in Figure 3b,d, while applying a constant voltage (+300 mV). Upon stretching, the films were manually pulled until taut, held in that position for approximately 5-10 s, then slowly relaxed back to its neutral position. Upon twisting, the films were manually twisted approximately 450 degrees clockwise in a quick motion, held for approximately 5-10 s, then quickly untwisted back to its neutral rectangular position.

All stretching and twisting gel movements generated measureable, and predictable changes in current (dI). The current signal was sampled at 100 kHz using a 1322A digitizer (Axon Instruments), and filtered at 1 kHz with a low-pass Bessel filter (DAGAN Chem Clamp). Current vs. time data was recorded using Axoscope 10.0 software (Molecule Devices), and analyzed with Clampfit 10.4 (Molecular Devices). The recorded traces were background subtracted and post-filtered to 100 Hz. All electrochemical experiments were performed in a home-built, grounded faraday cage.

2.3.10 Sensor Assembly and Electromechanical Testing

Fabrication of the auxetic structure was previously described in "*2.3.5 DIW Printing of Ion Gels*". The films were made by curing 6 g of ion gel pressed between 2 large borosilicate glass slides with 1mm spacers for 25 min under 365 nm light. The cross-linked ion gel is then removed from the glass slides and trimmed with a razor to produce a 4.5 × 7.0 cm film. The samples were then assembled into sensors in the following steps shown in Figure S7. Silver conductive coating (MG Chemicals) was applied onto 2 sheets of copper plates (1.5 × 7 cm). Upon placing the ends of the cross-linked ionogel onto the conductive coating, a thin layer of cyanoacrylate super glue

(The Original Super Glue) was spread around and on top of the ionogel followed by a second pair of copper plates (1.5 × 5 cm). Binder clips were then used to press the copper plates together at each end until the glue was completely dried.

The electromechanical characterization setup consisted of a dynamic mechanical tester (Electroforce Testbench, TA, USA) and source-meter (Keithley 2450, Tektronix, USA). Auxetic and film sensors were prepared and loaded into sandpaper lined grips to ensure a non-slip condition. The sensors were preloaded 0.1 N, and the cross-sectional area and gauge length was measured using the digital caliper. The gauge length was defined as the distance between contact points of the grips. 300 mV was applied through the film sensor and 100 mV was applied through the auxetic sensor, and the resulting current reading was equilibrated for 20 min before the application of a strain.

Uniaxial mechanical testing includes cyclic and ramp to failure experiments. For the cyclic experiments, the sensors are stretched to a specific distance (1.0, 1.5, and 2.0 cm) at a rate of 4 mm/s and relaxed back to its original position at the same rate. Each test consisted of 15 stretching/releasing cycles, with a 3 second pause between each cycle (Figure S8). For the ramp to failure experiments, the sensors are stretched at a rate of 0.16666 mm/s (10 mm/min) until failure. This experiment was performed in triplicate for both the film and auxetic samples.

2.4 RESULTS AND DISCUSSIONS

2.4.1 Formulation and Printability of F127-BUM Ion Gel

In the preparation of the ion gel, we first synthesized F127-BUM[45] by reacting the chain ends of commercial Pluronic F127 with isocyanatoethyl methacrylate. Pluronic F127 is an amphiphilic ABA triblock copolymer, comprised of poly(ethylene oxide) as the A blocks and poly(propylene oxide) as the B block, that forms a shear-thinning gel when dissolved in an aqueous medium (20-40 wt%). The F127-BUM is preferred over the F127-dimethacrylate our group has previously utilized[26,46,47] for its ease of purification. F127-BUM was initially dissolved in ionic liquid with methanol as a co-solvent, which was subsequently removed *in vacuo*. Several ionic liquids including 1-butyl-3-methylimidazolium hexafluorophosphate, 1-ethyl-3-methylimidazolium hydrogen sulfate, 1,3-dimethylimidazolium dimethyl phosphate, and $[BMIM]BF_4$ were tested, but only $[BMIM]BF_4$ provided good polymer solubility and afforded a gel. The optimal self-suppoting ion gel for DIW printing contained 27 wt% F127-BUM, 72.99 wt% $[BMIM]BF_4$, and 0.01 wt% photoinitiator (Figure 2.1).

2.4.2 Viscoelastic Behavior via Rheology

The shear-thinning and yielding characteristics of the ion gel were investigated using rheometrical experiments to better understand the behavior of the gel during extrusion. The strain sweep experiment (Figure 2.2a) was performed at 25 °C from 0.01 to 100% strain (1 Hz). This experiment showed the viscoelastic changes in the ion gel with increasing applied stress. The relatively high storage modulus (1.9×10^4 Pa) at low oscillatory stresses indicated the material is a firm gel. When the applied stress exceeded ~359 Pa, the storage modulus rapidly decreased, suggesting a gel-to-sol transition—the behavior required for the ion gel to flow out from the nozzle with applied stress. The viscosity versus shear rate experiment (Figure 2.2b) was performed at 25 °C over a shear rate range of 0.01 to 100 s-1. This experiment showed the decrease in viscosity of the gel with an increase in applied shear rate, confirming the gel's shear-thinning behavior. In Figure 1d, a strain sweep experiment showed the gel-to-sol transition. The cyclic shear strain experiment (Figure 2.2c) was performed at 25 °C using alternating strains of 1% for 5 min and 100% for 3 min (1 Hz). In this experiment, the storage modulus instantly switched between high (1.6×10^4 Pa) and low (171 Pa) values by alternating the amount of applied strain from 1% to

100%, respectively. The rapid transition between the two states suggested a fast response in which the ion gel could flow when pressure was applied and quickly recover its gel state when pressure was removed. The process of alternating between high and low stress was repeated for 5 cycles without any significant hysteresis, and minimal thixotropy was observed. As a result, the ion gel ink reliably printed self-supporting multi-layered constructs, even in the absence of chemical cross-linking. Lastly, a UV-curing rheometrical experiment (Figure 2.2d) showed the process of the gel cross-linking via photopolymerization. The samples were equilibrated for 120 s, and a 1200 s irradiation with 365 nm light at 5 $mW\cdot cm^{-2}$ intensity was applied, and the sample was monitored at room temperature for a total of 1500 s (1 Hz, 1% strain). After exposure to 365 nm light for a period of 25 min, the storage modulus increased from 1.67×10^5 Pa to 2.66×10^5 Pa, which suggested an increase in firmness of the gel due to the photocrosslinking process.

2.4.3 Ion Gel Properties Post-Curing

After cross-link, the gel exhibits excellent transparency as well (Figure 2.3a) Additionally, the bulk mechanical strength of the cross-linked ion gel was determined via tensile testing. As shown in the stress-strain curve (Figure 2.3b), the tensile strength of the ion gel reaches 0.81 MPa at 242 % strain. In addition to their elasticity, the cross-linked ion gel exhibited a high degree of toughness (1.02×10^6 $J\cdot m^{-3}$). Interestingly, both the ultimate strain and toughness were higher than other reported values for ion gels.[42,48–50]

The ionic conductivity of the ion gel before and after cross-linking was evaluated by AC impedance spectroscopy. Figure 2.4a represents the Arrhenius plots for both samples. Similar to previous reports, the addition and cross-linking of polymer appears to decrease the overall conductivity of the system.[13,33.51,52] We observed that cross-linking the polymer decreased the conductivity values by one-third of the initial values. However, with remarkable improvement of the ion gel's mechanical properties, the cross-linked gel still provided a good ionic conductivity, suggesting that the ionic mobility is not significantly compromised by the cross-linked network.[53]

Thermogravimetric analysis (Figure 2.4b) was performed to confirm that the incorporation of a cross-linked polymer network did not hinder the ionic liquid's high thermal stability.[32,54] The results indicated that the cross-linked ion gel was stable at high temperatures and the onset of decomposition did not occur until 361 °C. In comparison, pure [BMIM]BF_4 has an onset of thermal decomposition of 357 °C[54], which confirmed that the incorporation of the ionic liquid into a cross-linked polymer network did not affect its thermal stability. Additionally, total mass loss from room temperature to 200 °C is 0.3747%, suggesting that there was no water or methanol remaining in the sample from gel processing.

2.4.4 Initial Evaluation as Soft Sensor

The cross-linked gel was tested for its capability as a strain sensor by measuring its current response while applying a constant potential. Initial testing by hand on a small ionogel sample with dimensions 1 cm × 2.5 cm and thickness of 0.6 mm showed that small mechanical motions such as stretching and twisting generated relatively large current fluctuations (Figure 2.5). These current changes in response to the gel's mechanical motions can be explained using Equation 1 and Equation 2.[20] Equation 1 describes the relationship between resistance (R, Ω) to resistivity (ρ, Ω·m), with varying length (L, m) and cross sectional area (A, m^2). Equation 2 is derived through substitution of Ohm's law (V=IR) for resistance to explicitly show the relationship between current, I, and film geometry L, A.

$$\boldsymbol{R = \rho \frac{L}{A}} \tag{1}$$

$$\boldsymbol{\frac{V}{I} = \rho \frac{L}{A}} \tag{2}$$

The polarity of the measured current responses were in agreement with Equation 2. While the film is stretched, the length increased and the area decreased, which resulted in a decrease in current. Likewise, the twisting motion slightly decreased the length of the film and increased the cross-sectional area due to the gel folding on itself, to afford an increase in current. Since the applied movements produced predictable changes in current according to Equation 2, we demonstrated that our ionogel may be used as a sensor for detecting these mechanical movements.

2.4.5 Direct-Write 3D Printing

The ion gel was extruded through a 25 gauge nozzle (I.D. 0.260 mm) onto a glass slide under a pressure of 20 psi. The position of the nozzle was controlled by movement of the syringe holder and print bed. All prints done in this works are shown in Figure 2.6. We have printed 20 layer-single lines without loss in layer-to-layer integrity, a leaning cylinder with 35° offset without needing supports, a 5-pointed star with intersecting filaments, and a large UW logo. These examples show the versatility in the structures achievable, and the ability of the ion gel inks to self-support the structure without needing to photocure layer-by-layer.

2.4.6 Fabrication of Auxetic Sensor and Electromechanical Testing

Subsequently, we compared the current responses of an auxetic structure versus a bulk rectangular film with the same outer dimensions. We printed an hourglass auxetic structure with line widths in the range of 0.5-0.7 mm at a pitch of 7.5 mm. By design, auxetic structures exhibit a negative Possion's ratio, wherein they expand and contract in directions transverse to the applied loads (Figure 2.7).[55] Auxetic structures are low in density (22% in area when compared to the bulk film) and more mechanically robust than their bulk equivalent forms. Additionally, fabrication of the auxetic sensors requires less material and yield a lightweight structure. For wearable sensors, this translates to increased sensor robustness and overall wear comfort for the user.

To accurately test the current change responses to applied strain, the film and auxetic structures were subjected to multiple stretching cycles at specific stretching distances. The auxetic structure was more sensitive to changes in elongational strain, which was reflected by changes in the current. As expected, the % change in current output doubled when the sensor was subjected to twice the stretching distance. The experiment was repeated to show consistent output across 3 different samples (Figure 2.8). With the same stretching distance, the percent change in current response are constant across the cycles. Cyclic testing was also performed on film samples. However, upon stretching the films by 1.5 cm over repeated cycles, the film mechanically fails (Figure 2.9).

Ramp to failure experiments demonstrated that the auxetic structure can be stretched further by over twice the distance. The bulk film sensors typically failed at 16.43, 10.25, 9.77 mm , while the auxetic sensor’s first failure point occurs at 23.53, 28.96, 51.10 mm (Figure 2.10). At the first failure point, the films break completely and can no longer operate to give a current reading. In contrast, at each failure point for the auxetic structure, only one filament within the structure mechanically failed while the rest of the sensor remained intact and conductive. In contrast to the bulk film’s immediate failure, the auxetic structure remains conductive and can still provide current readings in response to strain after multiple failure points. Therefore, the auxetic structure has a better operational range as a strain sensor relative to the analogous continuous film. The ramp to failure experiments for the auxetic sensor was recorded until the third failure point of the sensor.

2.5 CONCLUSION

In conclusion, we developed a shear-thinning ion gel that can be printed into geometric objects that are ionically conductive. The cured elastomeric ion gels exhibited a high toughness and were well suited for fabricating strain sensors that were sensitive to bending, twisting, and stretching motions. A strain sensor based on the ion gel printed into an auxetic geometry exhibited up to 310% greater extension relative to a continuous film. The auxetic construct exhibited a tolerance to internal mechanical failure during extension, as demonstrated by the small changes in conductivity as individual filaments were damaged. Moreover, the fabrication process consumes less material and yields a lightweight structure for overall increased wear comfort. Thus, these 3D printable ion gels are promising candidates to enable rapid prototyping and reiteration of complex geometries that can be integrated into sensor devices.

2.6 ACKNOWLEDGEMENTS

Adapted with permission from Wong, J.; Gong, A. T.; Defnet, P. A.; Meabe, L.; Beauchamp, B.; Sweet, R. M.; Sardon, H.; Cobb, C.; Nelson, A. 3D Printing Ionogel Auxetic Frameworks for Stretchable Sensors. *Adv. Mater. Technol.* **2019**, *4*, 1900452. Copyright 2019 WILEY-VCH Verlag GmbH & Co. KGaA, Weinheim

2.7 REFERENCES

(1) Huang, Z.; Hao, Y.; Li, Y.; Hu, H.; Wang, C.; Nomoto, A.; Pan, T.; Gu, Y.; Chen, Y.; Zhang, T.; Li, W.; Lei, Y.; Kim, N. H.; Wang, C.; Zhang, L.; Ward, J. W.; Maralani, X. Li, X.; Durstock, M. F.; Pisano, A.; Lin, Y.; Xu, S. Three-dimensional integrated stretchable electronics. *Nature Electronics*. **2018**, *1*, 473–480.

(2) Wu, H.; Huang, Y. A.; Xu, F.; Duan, Y.; Yin, Z. Energy Harvesters for Wearable and Stretchable Electronics: From Flexibility to Stretchability. *Adv. Mater.* **2016**, *28*, 9881–9919.

(3) Trung, T. Q.; Lee, N. E. Flexible and Stretchable Physical Sensor Integrated Platforms for Wearable Human-Activity Monitoring and Personal Healthcare. *Adv. Mater.* **2016**, *28*, 4338–4372.

(4) Guo, S. Z.; Qiu, K.; Meng, F.; Park, S. H.; McAlpine, M. C. 3D Printed Stretchable Tactile Sensors. *Adv. Mater.* **2017**, *29*, 1701218.

(5) Someya, T.; Amagai, M. Toward a new generation of smart skins. *Nature Biotechnology*. **2019**, *37*, 382–388.

(6) Hartmann, F.; Drack, M.; Kaltenbrunner, M. Meant to merge: Fabrication of stretchy electronics for robotics. *Sci. Robot*. **2018**, *3*, eaat9091.

(7) Kim, H. J.; Sim, K.; Thukral, A.; Yu, C. Rubbery electronics and sensors from intrinsically stretchable elastomeric composites of semiconductors and conductors. *Sci. Adv*. **2017**, *3*, 1701114.

(8) Lei, Z.; Wang, Q.; Sun, S.; Zhu, W.; Wu, P. A Bioinspired Mineral Hydrogel as a Self-Healable, Mechanically Adaptable Ionic Skin for Highly Sensitive Pressure Sensing. *Adv. Mater*. **2017**, *29*, 1700321.

(9) Wales, D. J.; Cao, Q.; Kastner, K.; Karjalainen, E.; Newton, G. N.; Sans, V. 3D-Printable Photochromic Molecular Materials for Reversible Information Storage. *Adv. Mater*. **2018**, *30*, 1800159.

(10) Takei, Y.; Matsumoto, K.; Shimoyama, I. Wearable sweat monitoring sensor based on Ionic Liquid Gel. *IEEE Int. Conf. on Micro Electro Mechanical Systems (MEMS, IEEE)*, IEEE, Shanghai, China **2016**, 924–925.

(11) Xie, Y.; Xie, R.; Yang, H. C.; Chen, Z.; Hou, J.; López-Barrón, C. R.; Wagner, N. J.; Gao, K. Z. Iono-Elastomer-Based Wearable Strain Sensor with Real-Time Thermomechanical Dual Response. *ACS Appl. Mater. Interfaces* **2018**, *10*, 32435–32443.

(12) Xu, Y.; We, X.; Guo, X.; Kong, B.; Zhang, M.; Qian, X.; Mi, S.; Sun, W. The Boom in 3D-Printed Sensor Technology. *Sensors* **2017**, *17*, 1166.

(13) Zhang, S.; Wang, F.; Peng, H.; Yan, J.; Pan, G. Flexible Highly Sensitive Pressure Sensor Based on Ionic Liquid Gel Film. *ACS Omega* **2018**, *3*, 3014–3021.

(14) Bao, Z.; Chen, X. Flexible and Stretchable Devices. *Adv. Mater.* **2016**, *28*, 4177–4179.

(15) Shin, S. R.; Farzad, R.; Tamayol, A.; Manoharan, V.; Mostafalu, P.; Zhang, Y. S.; Akbari, M.; Jung, S. M.; Kim, D.; Comotto, M.; Annabi, N.; Al-Hazmi, F. E.; Dokmeci, M. R.; Khademhosseini, A. A Bioactive Carbon Nanotube-Based Ink for Printing 2D and 3D Flexible Electronics. *Adv. Mater.* **2016**, *28*, 3280–3289.

(16) Patel, D. K.; Sakhaei, A. H.; Layani, M.; Zhang, B.; Ge, Q.; Magdassi, S. Highly Stretchable and UV Curable Elastomers for Digital Light Processing Based 3D Printing. *Adv. Mater.* **2017**, *29*, 1606000.

(17) Keplinger, C.; Sun, J. Y.; Foo, C. C.; Rothermund, P.; Whitesides, G. M.; Suo, Z. Stretchable, transparent, ionic conductors. *Science* **2013**, *341*, 984–987.

(18) Hinton, T. J.; Hudson, A.; Pusch, K.; Lee, A.; Feinberg, A. W. 3D Printing PDMS Elastomer in a Hydrophilic Support Bath via Freeform Reversible Embedding. *ACS Biomater. Sci. Eng.* **2016**, *2*, 1781–1786.

(19) Kim, D. H.; Rogers, J. A. Stretchable Electronics: Materials Strategies and Devices. *Adv. Mater.* **2008**, *20*, 4887–4892.

(20) Truby, R. L.; Wehner, M.; Grosskopf, A. K.; Vogt, D. M.; Uzel, S. G.M.; Wood, R. J.; Lewis, J. A. Soft Robotics: Soft Somatosensitive Actuators via Embedded 3D Printing. *Adv. Mater.* **2018**, *30*, 1706383.

(21) Jiang, Y.; Liu, Z.; Matsuhisa, N.; Qi, D.; Leow, W. R.; Yang, H.; Yu, J.; Chen, G.; Liu, Y.; Wan, C.; Liu, Z.; Chen, X. Auxetic Mechanical Metamaterials to Enhance Sensitivity of Stretchable Strain Sensors. *Adv. Mater.* **2018**, *30*, 1706589.

(22) Gao, Q.; Li, H.; Zhang, J.; Xie, Z.; Zhang, J.; Wang, L. Microchannel Structural Design For a Room-Temperature Liquid Metal Based Super-stretchable Sensor. *Sci. Rep.* **2019**, *9*, 5908.

(23) Lacey, S. D.; Kirsch, D. J.; Li, Y.; Morgenstern, J. T.; Zarket, B. C.; Yao, Y.; Dai, J.; Garcia, L. Q.; Liu, B.; Gao, T.; Zu, S.; Raghavan, S. R.; Connell, J. W.; Lin, Y.; Hu, L. Extrusion-Based 3D Printing of Hierarchically Porous Advanced Battery Electrodes. *Adv. Mater.* **2018**, *30*, 1705651.

(24) Schultz, A. R.; Lambert, P. M.; Chartrain, N. A.; Ruohoniemi, D. M.; Zhang, Z.; Jangu, C.; Zhang, M.; Williams, C. B.; Long, T. E. 3D Printing Phosphonium Ionic Liquid Networks with Mask Projection Microstereolithography. *Macro Lett.* **2014**, *3*, 1205–1209.

(25) Gebler, M.; Uiterkamp, A. J.M.S.; Visser, C. A global sustainability perspective on 3D printing technologies. *Energy Policy* **2014**, *74*, 158–167.

(26) Smith, P. T.; Basu, A.; Saha, A.; Nelson, A. Chemical modification and printability of shear-thinning hydrogel inks for direct-write 3D printing. *Polymer* **2018**, *152*, 42–50.

(27) Conner, B. P.; Manogharan, G. P.; Martof, A. N.; Rodomsky, L. M.; Rodomsky, C. M.; Jordan, D. C.; Limperos, J. W. Making sense of 3-D printing: Creating a map of additive manufacturing products and services. *Additive Manufacturing* **2014**, *1*, 64–76.

(28) Tom Lecklider, 3D printing drives automotive innovation, https://www.evaluationengineering.com/test-issues-techniques/technology/3d-printing/article/13014908/3d-printing-drives-automotive-innovation, accessed: Jan., 2019.

(29) Aprecia Pharmaceuticals, Zipdose Technology: World's First 3DP Dosage Form, https://www.aprecia.com/technology/zipdose, accessed: Jan., 2019

(30) Valentine, A. D.; Busbee, T. A.; Boley, J. W.; Raney, J. R.; Chortos, A.; Kotikian, A.; Berrigan, J. D.; Durstock, M. F.; Lewis, J. A. Hybrid 3D Printing of Soft Electronics. *Adv. Mater.* **2017**, *29*, 1703817.

(31) Nulwala, H.; Mirjafari, A.; Zhou, X. Ionic liquids and poly(ionic liquid)s for 3D printing – A focused mini-review. *European Polymer Journal* **2018**, *108*, 390–398.

(32) Lodge, T. P. A Unique Platform for Materials Design. *Science* **2008**, *321*, 50–51.

(33) Susan, Md.A.B.H.; Kaneko, T.; Noda, A.; Watanabe, M. Ion Gels Prepared by in Situ Radical Polymerization of Vinyl Monomers in an Ionic Liquid and Their Characterization as Polymer Electrolytes. *J. Am. Chem. Soc.* **2005**, *127*, 4976–4983.

(34) Bideau, J. L.; Viau, L.; Vioux, A. Ionogels, ionic liquid based hybrid materials. *Chem. Soc. Rev.* **2011**, *40*, 907–925.

(35) Isik, M.; Lonjaret, T.; Sardon, H.; Marcilla, R.; Herve, T.; Malliaras, G. G.; Ismailova, E.; Mecerreyes, D. Cholinium-based ion gels as solid electrolytes for long-term cutaneous electrophysiology. *J. Mater. Chem. C* **2015**, *3*, 8942–8948.

(36) Tian, K.; Bae, J.; Bakarich, S. E.; Yang, C.; Gately, R. D.; Spinks, G. M.; Panhuis, M.; Suo, Z.; Vlassak, J. J. 3D Printing of Transparent and Conductive Heterogeneous Hydrogel–Elastomer Systems. *Adv. Mater.* **2017**, *29*, 1604827.

(37) Peng, R.; Wang, Y.; Tang, W.; Yang, Y.; Xie, X. Progress in Imidazolium Ionic Liquids Assisted Fabrication of Carbon Nanotube and Graphene Polymer Composites. *Polymers* **2013**, *5*, 847–872.

(38) Winey, K.; Kashiwagi, T.; Mu, M. Improving Electrical Conductivity and Thermal Properties of Polymers by the Addition of Carbon Nanotubes as Fillers. *MRS Bulletin* **2007**, *32*, 348–353.

(39) Ho, C. C.; Evans, J. W.; Wright, P. K. Direct write dispenser printing of a zinc microbattery with an ionic liquid gel electrolyte. *J. Micromech. Microeng.* **2010**, *20*, 104009.

(40) Karjalainen, E.; Wales, D. J.; Gunasekera, D. H.A.T.; Dupont, J.; Licence, P.; Wildman, R. D.; Sans, V. Tunable Ionic Control of Polymeric Films for Inkjet Based 3D Printing. *ACS Sustainable Chem.* **2018**, *6*, 3984–3991.

(41) Tang, B.; Schneiderman, D. K.; Bidoky, F. Z.; Frisbie, C. D.; Lodge, T. P. Printable, Degradable, and Biocompatible Ion Gels from a Renewable ABA Triblock Polyester and a Low Toxicity Ionic Liquid. *Macro Lett.* **2017**, *6*, 1083–1088.

(42) Ahmed, K.; Naga, N.; Kawakami, M.; Furukawa, H. Extremely Soft, Conductive, and Transparent Ionic Gels by 3D Optical Printing. *Macromol. Chem. Phys.* **2018**, *219*, 1800216.

(43) Ndefru, B. G.; Ringstrand, B. S.; Diouf, S. I.Y.; Seifert, S.; Leal, J. H.; Semelsberger, T. A.; Dreier, T. A.; Firestone, M. A. Multiscale additive manufacturing of polymers using 3D photo-printable self-assembling ionic liquid monomers. *Mol. Syst. Des. Eng.* **2019**, 580–585.

(44) Markstedt, K.; Sundberg, J.; Gatenholm, P. 3D Bioprinting of Cellulose Structures from an Ionic Liquid. *Addit. Manuf.* **2014**, *1*, 115–121.

(45) Dutta, S.; Cohn, D. Temperature and pH responsive 3D printed scaffolds. *J. Mater. Chem. B.* **2017**, *5*, 9514–9521.

(46) Basu, A.; Saha, A.; Goodman, C.; Shafranek, R. T.; Nelson, A. Catalytically Initiated Gel-in-Gel Printing of Composite Hydrogels. *ACS Appl. Mater. Interfaces* **2017**, *9*, 40898–40904.

(47) Saha, A.; Johnston, T. G.; Shafranek, R. T.; Goodman, C. J.; Zalatan, J. G.; Storti, D. W.; Ganter, M. A.; Nelson, A. Additive Manufacturing of Catalytically Active Living Materials. *ACS Appl. Mater. Interfaces* **2018**, *10*, 13373–13380.

(48) Ding, Y.; Zhang, J.; Chang, L.; Zhang, X.; Liu, H.; Jiang, L. Preparation of High-Performance Ionogels with Excellent Transparency, Good Mechanical Strength, and High Conductivity. *Adv. Mater.* **2017**, *29*, 1704253.

(49) Gu, Y.; Zhang, S.; Martinetti, L.; Lee, K. H.; McIntosh, L. D.; Frisbie, C. D.; Lodge, T. P. High Toughness, High Conductivity Ion Gels by Sequential Triblock Copolymer Self-Assembly and Chemical Cross-Linking. *J. Am. Chem. Soc.* **2013**, *135*, 9652–9655.

(50) Fujii, K.; Asai, H.; Ueki, T.; Sakai, T.; Imaizumi, S.; Chung, U.; Watanabe, M.; Shibayama, M. High-performance ion gel with tetra-PEG network. *Soft Matter* **2012**, *8*, 1756–1759.

(51) Zhang, S.; Lee, K. H.; Sun, J.; Frisbie, C. D.; Lodge, T. P. Ionic Conductivity, Capacitance, and Viscoelastic Properties of Block Copolymer-Based Ion Gels. *Macromolecules* **2011**, *44*, 940–949.

(52) Armand, M.; Endres, F.; MacFarlane, D. R.; Ohno, H.; Scrosati, B. Ionic-liquid materials for the electrochemical challenges of the future. *Nat. Mater.* **2009**, *8*, 621–629.

(53) Cao, Y.; Morrissey, T. G.; Acome, E.; Allec, S. I.; Wong, B. M.; Keplinger, C.; Wang, C. A Transparent, Self-Healing, Highly Stretchable Ionic Conductor. *Adv. Mater.* **2017**, *29*, 1605099.

(54) Liu, P.; Wang, M.; Cheng, A. M. Thermal Stability and Vapor–Liquid Equilibrium for Imidazolium Ionic Liquids as Alternative Reaction Media. *J. Chem. Eng. Data* **2015**, *60*, 836–844.

(55) Kapnisi, M.; Manfield, C.; Marijon, C.; Guex, A. G.; Perbellini, F.; Bardi, I.; Humphrey, E. J.; Puetzer, J. L.; Mawad, D.; Koutsogeorgis, D. C.; Stuckey, D. J.; Terracciano, C. M.; Harding, S E.; Stevens, M. M. Auxetic Cardiac Patches with Tunable Mechanical and Conductive Properties toward Treating Myocardial Infarction. *Adv. Funct. Mater* **2018**, *28*, 1800618.

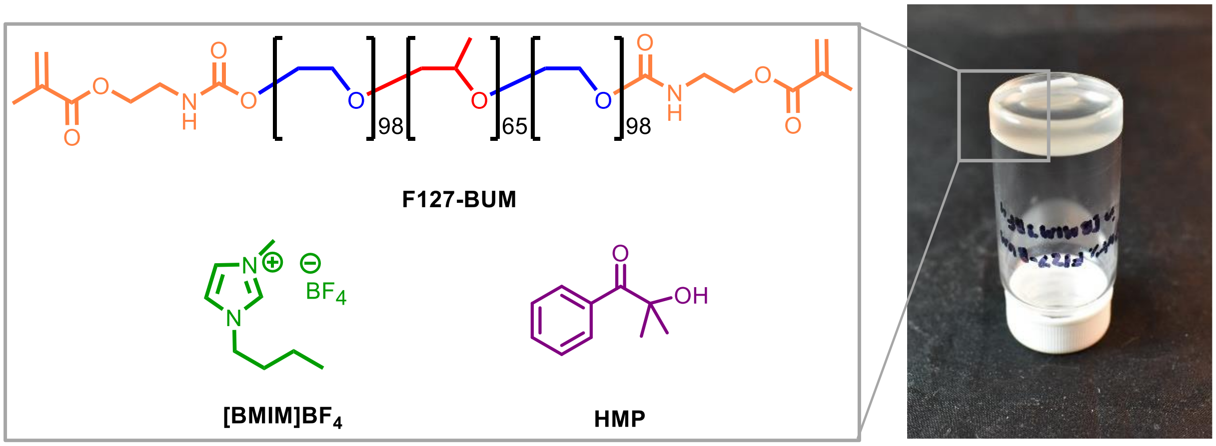

Figure 2.1 The optimized ion gel was formed from F127 bisurethane methacrylate (F127-BUM) using 1-butyl-3-methylimidazolium tetrafluoroborate ([BMIM]BF_4) as the ionic liquid and 2-hydroxy-2-methylpropiophenone (HMP) as the photoradical initiator. Methanol was initially used as a cosolvent. Upon evaporation of methanol, a clear, self-supporting ion gel is obtained.

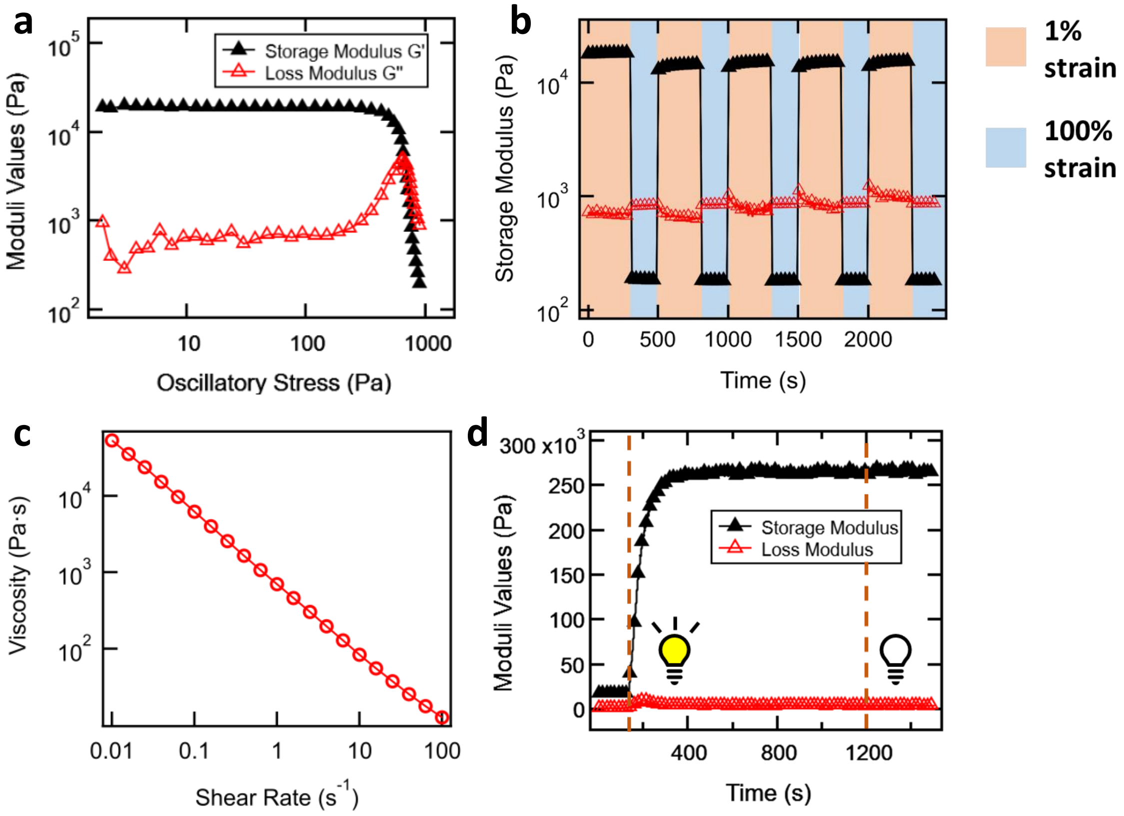

Figure 2.2 Rheometrical characterization including a) strain sweep representing the yielding point of ion gel in response to applied stress, b) cyclic strain experiment, which illustrates the fast transition between sol- and gel-state with with alternating low (1%) strain and high (100%) strain, c) viscosity vs. shear rate to show the shear-thinning behavior, and d) UV cure experiment to show increase in robustness after exposure to 365 nm light to induce photopolymerization.

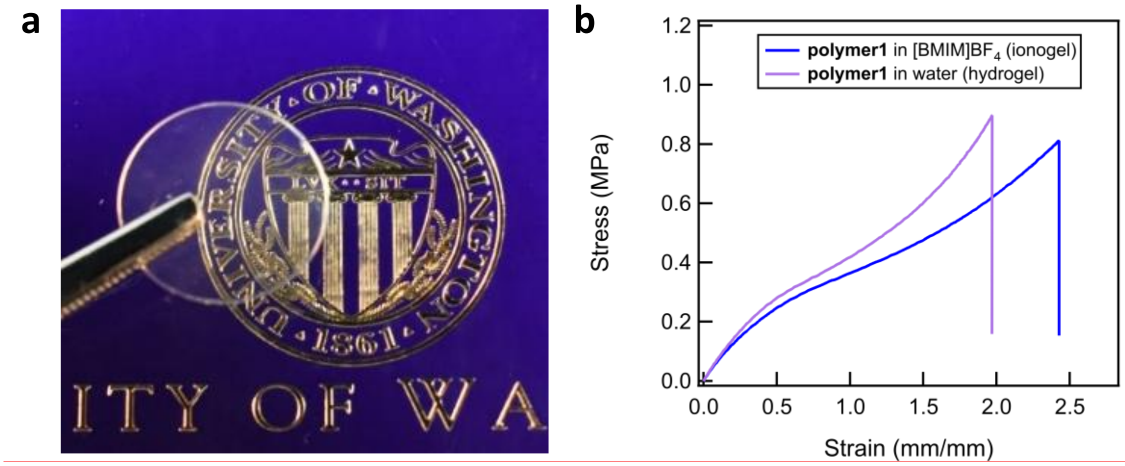

Figure 2.3 Properties of the ion gel after photocrosslinking. a) Photograph of a cross-linked ion gel disk demonstrating its excellent transparency (16.4 mm diameter, 1.0 mm thickness). b) Tensile stress-strain curve for 27 wt% F127-BUM hydrogel and ion gel.

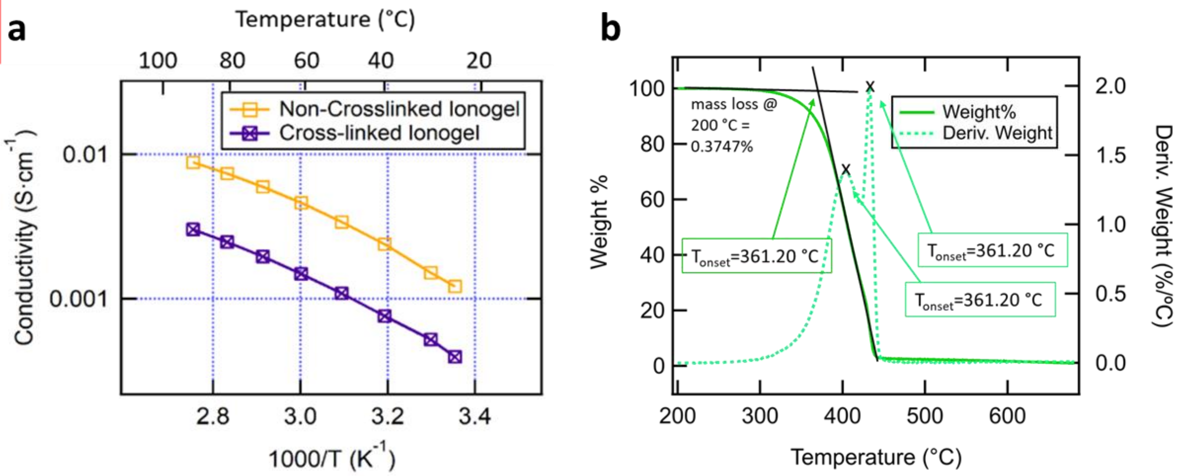

Figure 2.4 a) Calculated ionic conductivity values across a temperature range 25-90 °C. b) The resulting TGA plot shows high thermal stability and low water content in the crosslinked ion gel.

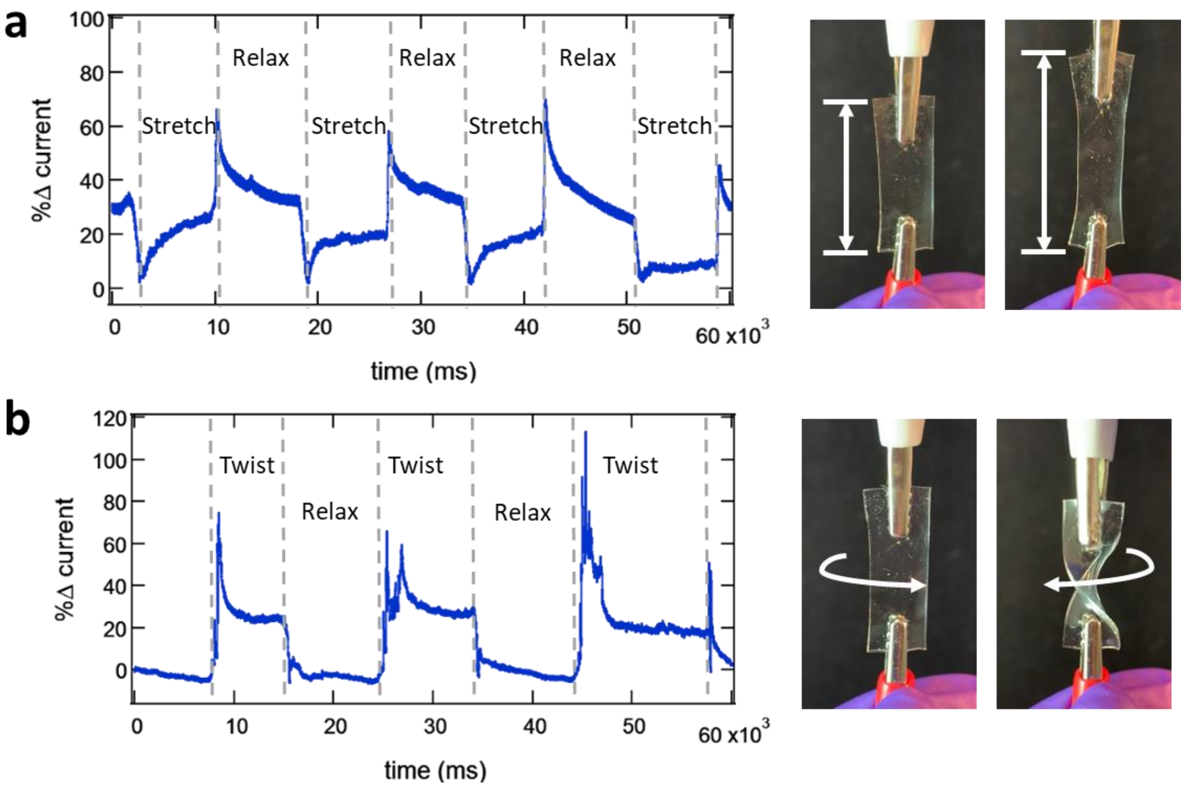

Figure 2.5 Changes in current were measured for a cross-linked ion gel continuous film (1 × 2.5 cm) in response to (c) stretching by 1 cm and (d) twisting clockwise by 450° by hand. The changes in current are repeatable, as shown in the characteristic shape of the curves with each deformation mode.

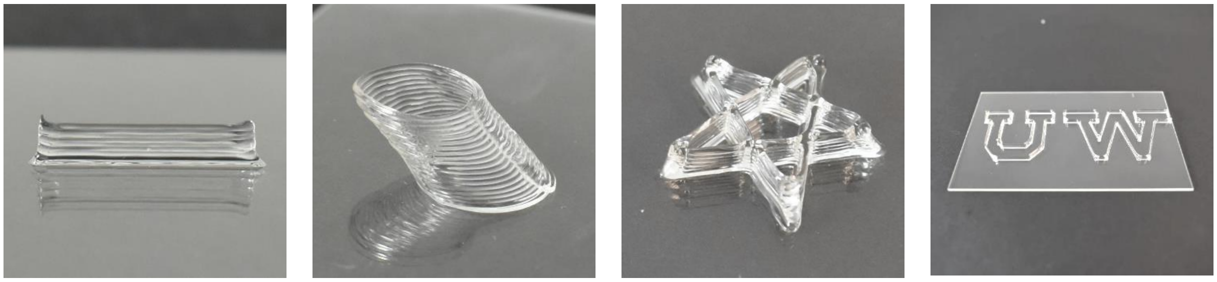

Figure 2.6 All printed objects have 0.3 mm single layer heights. Example prints include (left to right): 20 layer line; 1 cm diameter leaning cylinder with 35° offset; 8 layer, 1.3 cm wide star; 20 layer, 1 cm diameter cylinder; 8 layer, 7 × 2.5 cm UW logo.

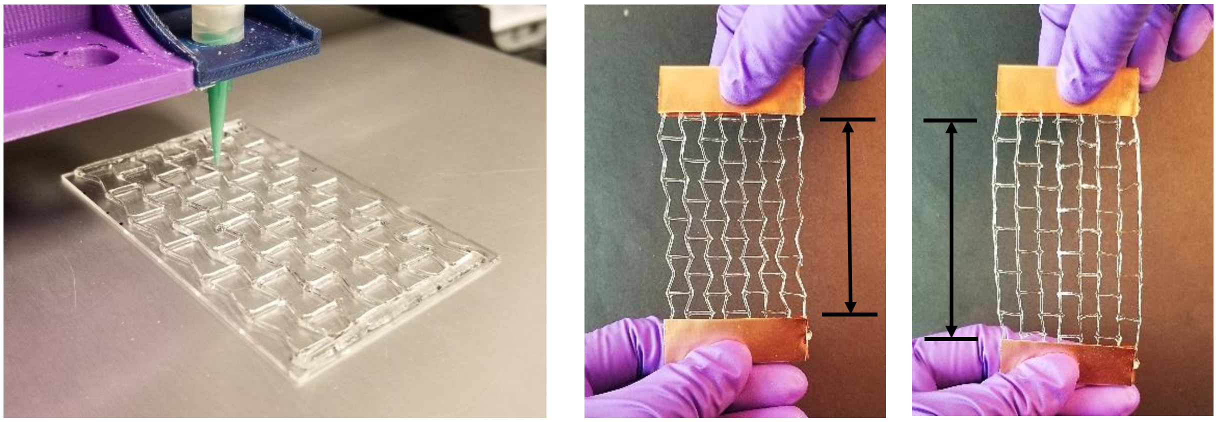

Figure 2.7 The printed and cross-linked auxetic structure (4.5 × 7 cm) expands in the direction normal to the tensile forces when stretched.

Sample #1:

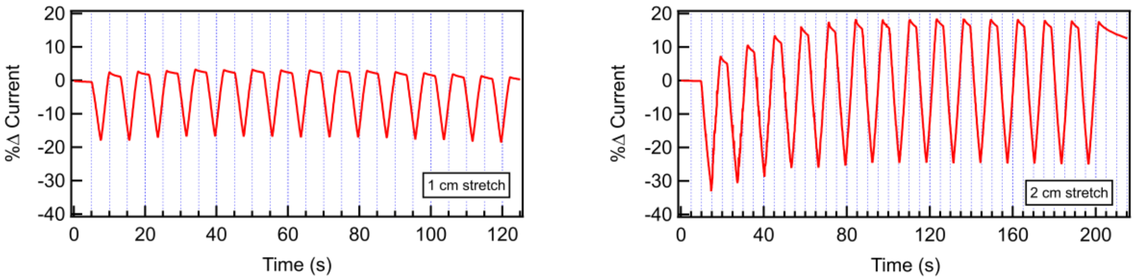

Sample #2:

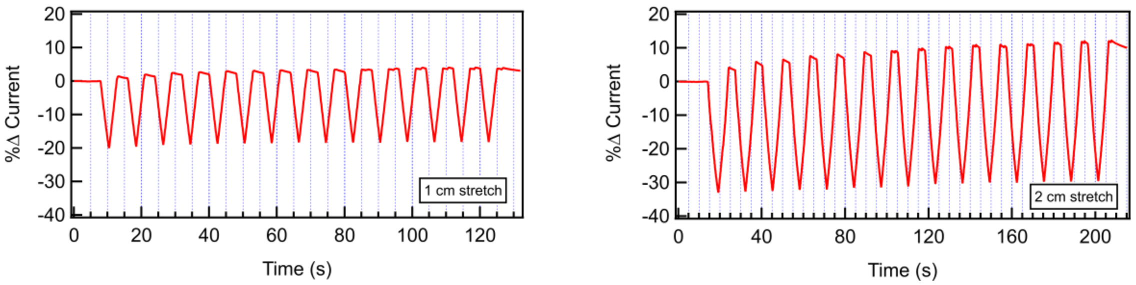

Sample #3:

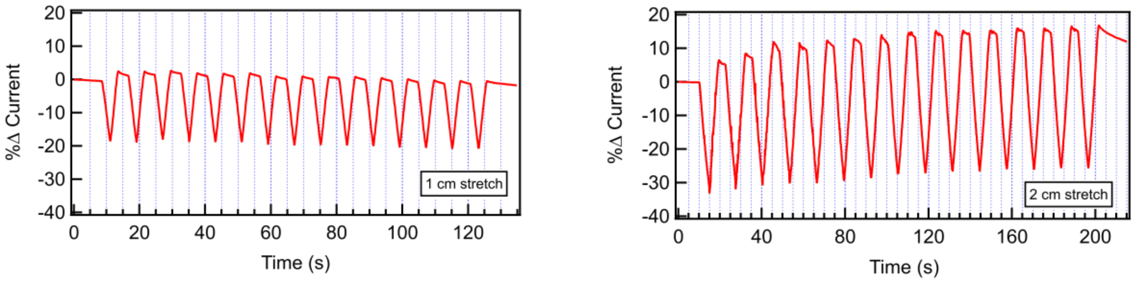

Figure 2.8 Cyclic test on printed auxetic sensor. The graphs show the current changes that occur as the auxetic structure was stretched by 1 cm and 2 cm for 15 cycles. The % current change doubled when the sensor was stretched to twice the distance. The current changes are similar across multiple printed samples.

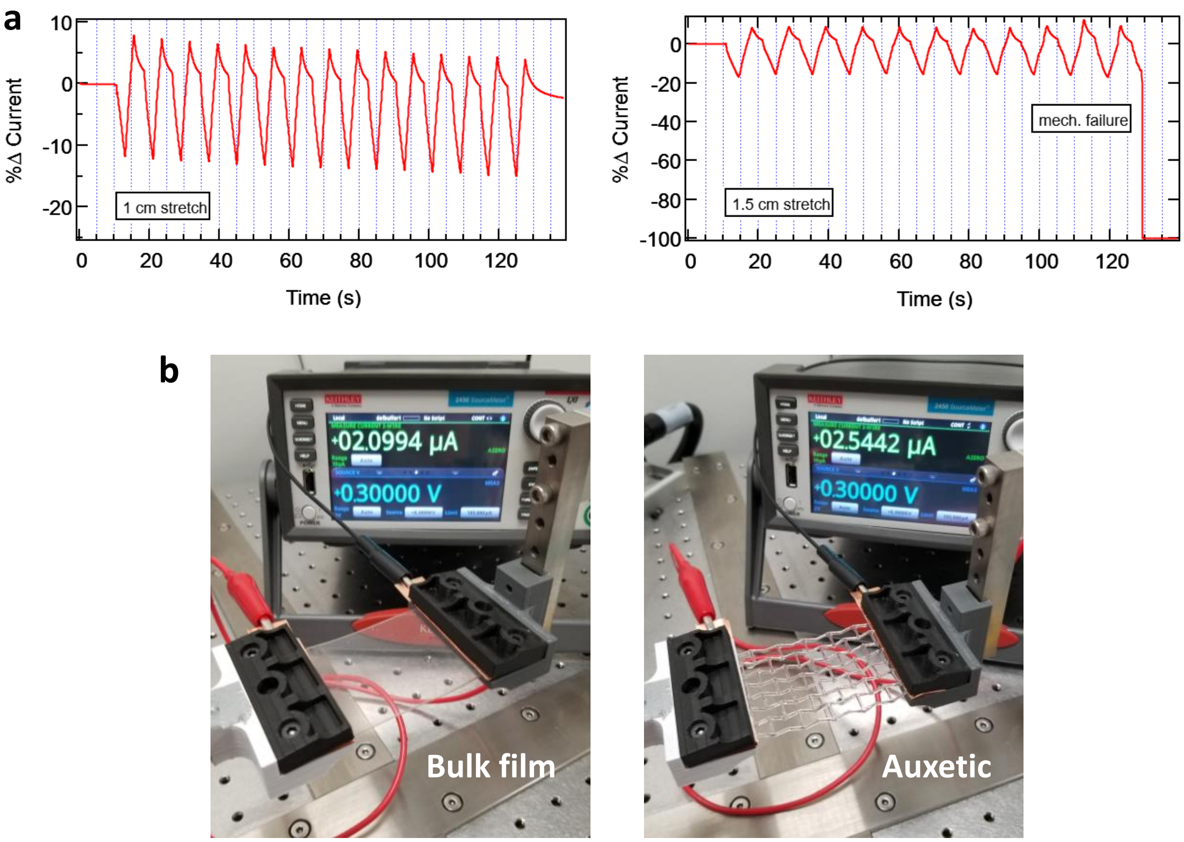

Figure 2.9 Cyclic test on bulk film sensor. a) The film breaks during the 1.5 cm stretching cyclic test, dropping the current reading to 0 A. b) Electromechanical testing setup while applying a constant potential of 300 mV on the casted film and 100 mV on the printed auxetic structure.

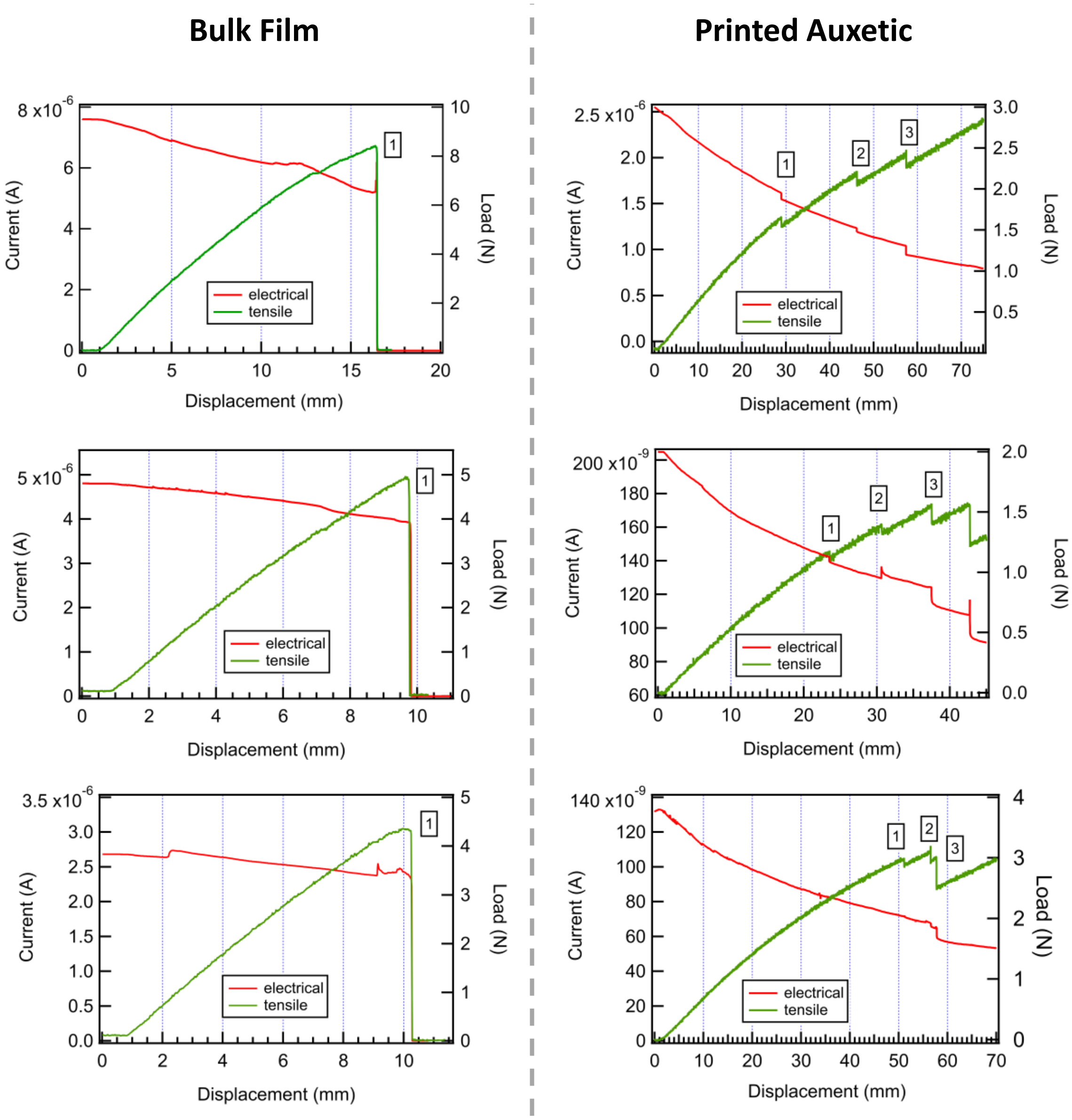

Figure 2.10 Ramp to failure experiment on both the bulk film and printed auxetic structure shows the increased stretchability of the auxetic structure relative to the casted film. The auxetic structure provides a current response after multiple failure points (labeled with boxed 1, 2, and 3), while the current response from the film immediately falls to 0 A at the first failure point.

CHAPTER 3: **MECHANO-ACTIVATED OBJECTS WITH MULTIDIRECTIONAL SHAPE MORPHING PROGRAMMED VIA 3D PRINTING**

3.1 ABSTRACT

Mechano-activation as a stimuli-response in 4D printing offers advantages such as orthogonality to other stimuli and control over the magnitude of applied force. Herein, we demonstrate mechanically activated morphing with directional control that is dictated by the patterns produced via multi-material 3D printing. An advantage of this approach is that pre-stretching of the sample is not required. We developed on gel inks comprised of a cross-linkable self-assembling triblock copolymer and polymerizable ionic liquids that varied in the size of the cation. The multi-material printing of these inks afforded objects that changed their shape in a predetermined manner upon the application of a tensile force.

3.2 INTRODUCTION

Stimuli-responsive 3D printed objects (4D printing) have recently garnered much attention due to their potential in the development of robotic actuators, sensors, and biomedical devices.[1–3] By utilizing responsive materials, the printed constructs undergo chemical or physical changes through time when exposure to various stimuli, including temperature, light, or electromagnetic fields, are used to induce a mechanical shape change.[4–8] In contrast, biological systems, such as Venus fly traps and mimosa plants, have inspired a growing interest in 4D objects that respond to mechanical stimuli (either applied force or deformation) to achieve a complex autonomous response.[9–16]

Mechanical forces can be orthogonal to other stimuli and offer facile control over the magnitude of the applied force. One mechanism that has been shown to achieve shape morphing is to leverage composite (e.g. two materials bonded together, which we also refer to as a "bilayer") elements with mismatched elastic properties.[17–21] Upon compressive loading[17] or relaxation of a previously applied strain (e.g. pre-strain)[18–21], composite elements can undergo 3D shape changes via buckling instabilities or bending. Within the context of 4D printing, previously demonstrated examples of mechanically induced shape change have been restricted to 3D printing on already pre-strained layers. The major downside of this approach is that it significantly confines the possible designs that can be printed and the resulting morphed shapes achieved, due to the necessity of a pre-stretched sheet. For instance, prior studies on pre-stretched sheets were restricted to unidirectional folding.[18] Without the need for pre-straining the sample, the ability to easily fabricate complex 3D geometries with multiple materials, can be leveraged, and more complex 4D objects and responses achieved. So far, two examples that demonstrated mechano-activated shape change in the absence of a pre-stretched layer were achieved by mismatched recovery introduced by alignment of embedded fibers[22] and degree of crystallinity[23], however, these examples cannot be 3D printed, which limits the complexity of their potential shape changes.

Herein, we demonstrate 3D printable ion gel inks that enable fabrication of multi-layered and multi-material objects with tunable viscoelastic and plastic responses, and then show how these inks can be used to create 3D constructs that can undergo multidirectional mechano-activated shape change without the need for pre-strain (Figure 3.1a). Tailoring the underlying materials' viscoelastic and plastic response enables control over the temporal response of the composite, as well as its reversibility. Shear-thinning ion gel inks based on self-assembling F127-bisurethane methacrylate (F127-BUM, Figure 3.1b) in imidazolium ionic liquids were previously shown to be effective for direct ink write (DIW) 3D printing to afford robust multi-layered constructs.[24] Unlike hydrogels (a commonly utilized 4D printing ink), ion gels utilize ILs with low vapor pressures[25–27], and as a consequence, do not dry out under ambient conditions. The polymerizable ionic liquids (PIL) used to form the ion gels in this study contain vinyl groups that can undergo photo-initiated polymerization (Figure 3.1c). Thus, after the ion gels were printed, the entire construct was photo-cured to form ionoelastomer comprised of continuous polymer networks and F127-BUM crosslinks (Figure 3.1d) that had varied elastic, viscous, and plastic mechanical proper-ties. Used in the context of multi-material DIW printing, these ion gels with varied mechanical properties enabled our creation of objects that are programmed via 3D printing to undergo multidirectional mechano-activated shape change in response to tensile forces.

3.3 MATERIALS AND METHODS

3.3.1 Materials

Pluronics® F127 (BioReagent) was purchased from MilliporeSigma. 2-isocyanatoethyl methacrylate (98%), dibutyltin dilaurate (>95%), 1-bromoethane (>99%), 1-bromobutane (>98%), 1-bromohexane (>98%), and sodium tetrafluoroborate (>95%) were purchased from TCI America. 1-vinylimidazole (>99%) was purchased from Alfa Aesar. Diethyl ether, acetone, and methanol (HPLC grade) were purchased from Fisher Scientific. All reagents were used as received. Anhydrous methylene chloride was obtained by purification over alumina column on a Pure Process Technology purification system. All ^{1}H and ^{13}C NMR spectra were collected on a Brüker Avance DRX 500 MHz spectrometer equipped with a Brüker triple resonance TXO probe (SI). Spectra were collected at 298 K with a pulse delay time (d1) of 5 or 10 s and 24 scans (^{1}H) and 32 scans (^{13}C). The spectrometer was interfaced with a computer running Red Hat Enterprise Linux

6.2 and Topspin 2.1 software. Spectra were analyzed with Topspin 4.0.7 software. DMSO-d_6 was purchased from Cambridge Isotope Laboratories (D, 99.9% + 0.05% V/V TMS).

3.3.2 Synthesis of 1-ethyl-3-vinylimidazolium bromide ([EVIM]Br)

To a solution of 1-vinylimidazole (18.12 mL, 200 mmol) in acetonitrile (100 mL), 1-bromoethane (17.91 mL, 240 mmol, 1.2 equiv.) was added and magnetically stirred at 40 °C for 24 h. The solution was allowed to cool, and the crude product was precipitated in 500 mL EtOAc. The solids are collected by filtration, redissolved with minimal amount of MeOH, and added dropwise into 500 mL EtOAc. The precipitate is collected by filtration as a white solid and further dried in vacuo at 35 °C (32.71 g, 80 %). ^{1}H NMR (500 MHz, DMSO-d_6, δ): 9.67 (s, 1 H); 8.26 (t, 1 H); 8.00 (t, 1 H); 7.33 (q, 1 H); 6.00 (dd, 1 H); 5.41 (dd, 1 H); 4.25 (q, 2 H); 1.45 (t, 3 H).

3.3.3 Synthesis of 1-butyl-3-vinylimidazolium bromide ([BVIM]Br)

1-vinylimidazole (9.06 mL, 100 mmol) and 1-bromobutane (12.89 mL, 120 mmol, 1.2 equiv.) were magnetically stirred at 45 °C for 24 h. After cooling, the viscous solution was washed with 100 mL ether three times and dried under vacuum to yield a pale yellow viscous liquid in quantitative yield. ^{1}H NMR (500 MHz, DMSO-d_6, δ): 9.80 (s, 1 H); 8.30 (t, 1 H); 8.03 (t, 1 H); 7.36 (q, 1 H); 6.03 (dd, 1 H); 5.41 (dd, 1 H); 4.24 (t, 2 H); 1.81 (quintet, 2 H); 1.27 (sextet, 2 H); 0.89 (t, 3 H).

3.3.4 Synthesis of 1-hexyl-3-vinylimidazolium bromide ([HVIM]Br)

1-vinylimidazole (9.06 mL, 100 mmol) and 1-bromohexane (16.80 mL, 120 mmol, 1.2 equiv.) were magnetically stirred at 45 °C for 24 h. After cooling, the viscous solution was washed with 100 mL ether five times and dried under vacuum to yield a pale yellow viscous liquid in quantitative yield. ^{1}H NMR (500 MHz, DMSO-d_6, δ): 9.76 (s, 1 H); 8.29 (t, 1 H); 8.01 (t, 1 H);

7.35 (q, 1 H); 6.02 (dd, 1 H); 5.41 (dd, 1 H); 4.22 (t, 2 H); 1.82 (quintet, 2 H); 1.26 (m, 6 H); 0.84 (t, 3 H).

3.3.5 Synthesis of 1-ethyl-3-vinylimidazolium tetrafluoroborate ([EVIM]BF_4)

1-ethyl-3-vinylimidazolium bromide (32.71 g, 161 mmol) and sodium tetrafluoroborate (18.57 g, 169 mmol, 1.05 equiv.) were added to acetone (75 mL) and let stir at rt for 48 h. The solution is then filtered through alumina to remove NaBr (fine white powder) and acetone was removed in vacuo to obtain a pale yellow oil. The oil is then filtered through alumina to remove remaining $NaBF_4$ (white crystalline solids) and dried in vacuo (23.08 g, 68%). ^{1}H NMR (500 MHz, DMSO-d_6, δ): 9.45 (s, 1 H); 8.16 (t, 1 H); 7.91 (t, 1 H); 7.27 (q, 1 H); 5.94 (dd, 1 H); 5.41 (dd, 1 H); 4.23 (q, 2 H); 1.45 (t, 3 H).

3.3.6 Synthesis of 1-butyl-3-vinylimidazolium tetrafluoroborate ([BVIM]BF_4), 1-hexyl-3-vinylimidazolium tetrafluoroborate ([HVIM]BF_4)

[BVIM]BF_4 and [HVIM]BF_4 were prepared using the same method for [EVIM]BF_4. The resulting products were pale yellow oils ([BVIM]BF_4 :16.17 g, 67.9%, [HVIM]BF_4: 14.85 g, 55.8%). [BVIM]BF_4 ^{1}H NMR (500 MHz, DMSO-d_6, δ): 9.46 (s, 1 H); 8.18 (t, 1 H); 7.91 (t, 1 H); 7.27 (q, 1 H); 5.95 (dd, 1 H); 5.42 (dd, 1 H); 4.20 (t, 2 H); 1.81 (quintet, 2 H); 1.29 (sextet, 2 H); 0.91 (t, 3 H). [BVIM]BF_4 ^{13}C NMR (500 MHz, DMSO-d_6, δ): 135.3; 128.8; 123.2; 119.1; 108.6; 49.0; 31.0; 18.8; 13.2. [HVIM]BF_4 ^{1}H NMR (500 MHz, DMSO-d_6, δ): 9.46 (s, 1 H); 8.18 (t, 1 H); 7.92 (t, 1 H); 7.28 (q, 1 H); 5.95 (dd, 1 H); 5.42 (dd, 1 H); 4.19 (t, 2 H); 1.82 (quintet, 2 H); 1.27 (m, 6 H); 0.86 (t, 3 H). [HVIM]BF_4 ^{13}C NMR (500 MHz, DMSO-d_6, δ): 135.3; 128.9; 123.2; 119.1; 108.6; 49.2; 30.5; 29.0; 25.1; 21.8; 13.8.

3.3.7 ATR-FTIR on PILs Before/After UV Curing

Photopolymerization of the PILs are monitored via FTIR spectroscopy. Spectra were collected on a Perkin Elmer Frontier FT-IR/FIR Spectrometer with a Universal ATR Sampling Accessory. Both the PILs and ionoelastomers were tested under ambient conditions.

3.3.8 Preparation of Ion Gels

The [EVIM]BF_4 and [BVIM]BF_4 ion gels were prepared by adding 0.81 g F127-BUM to 2.19 g [EVIM]BF_4 or [BVIM]BF_4. To prepare the [HVIM]BF_4 ion gel, 1.11 g of F127-BUM was added to 1.89 g [HVIM]BF_4. To each mixture, 6 μL of 2-hydroxyl-2-methylpropriophenone was added via volumetric pipette and approximately 3 mL of MeOH was added as a cosolvent. The mixtures are subjected to magnetic stirring for 2 h until a clear solution was obtained. MeOH was then removed *in vacuo* at 40 °C until a transparent, self-supporting gel was obtained. The ion gels are loaded into syringes and centrifuged to remove air pockets. The syringe cap was then removed and replaced with a 25 Ga Metcal extrusion nozzle (I.D. 0.26 mm).

3.3.9 Small-Angle X-ray Scattering

SAXS measurements were carried out at the Small- and Wide-Angle X-Ray Scattering (SAXS/WAXS/GISAXS) Beamline 7.3.3 at the Advanced Light Source facility located in the Lawrence Berkeley National Laboratory, Berkeley, CA. A monochromated X-ray beam with a wavelength of 1.23984 Å was used to irradiate the samples at room temperature, and the sample-to-detector distance was set at 3570 mm. The scattered X-rays were counted using ADSC Quantum 4r CCD detectors with an active area of 188x188 mm^2 (pixel size 0.172 mm). The beamline control and data acquisition (DAQ) was done through LabVIEW, provided at the ALS.[28] In each measurement for the ion gels, the ion gels were extruded into the center of stainless steel washers, sealed with Kapton tape, and mounted onto the sample holder. For measurements on the ionoelastomers, the samples were directly taped onto the sample holder.

By obtaining the Q-values at the maxima of the peaks, the corresponding particle diameter (Equation 1) can be determined.

$$particle\ diameter = \frac{2\pi}{Q} \tag{1}$$

For our material system, the particle diameter is equivalent to the average distance between the centers of micelles.

3.3.10 Rheological characterization

Rheological characterization was performed on a TA Instruments DHR-2 equipped with an Advanced Peltier Plate system. All rheometric experiments were performed using a stainless steel 8 mm upper plate. All gel samples were loaded onto a 3 cc syringe, centrifuged to remove any trapped air bubbles, and left overnight to equilibrate. The sample was then loaded by extruding the gel onto the loading plate and trimmed after the upper plate was lowered to the trim gap at 600 μm. The geometry gap between upper and lower plates was then set to 500 μm for all experiments. For all experiments, a pre-shear was applied at 5 °C for 10 s before additional sample conditioning at 25 °C for 8 min. The frequency sweep experiment was performed to measure the storage and loss moduli at 1% strain over frequency range of 0.1 to 100.0 rad/s (equivalent to 0.0159-15.9 Hz). The strain sweep experiment was performed to measure the storage and loss moduli over 0.01 to 100% strain (1 Hz). The cyclic shear strain experiment (Figure 1e) was performed at 25 °C using alternating strains of 1% for 5 min and 100% for 3 min (1 Hz). The viscosity versus shear rate experiment was performed at 25 °C over a shear rate range of 0.01 to 100 s^{-1}.

3.3.11 Conductivity Measurement

The ionic conductivity was studied by electrochemical AC impedance spectroscopy (EIS) with a Princeton Applied Research Ametek Parstat 4000A potentiostat with a Rhd Instruments Passive Cell Holder. Three different samples were measured for each material. For the ion gels, the gel was first extruded onto an electrode with a Teflon washer (inner area of 0.196 cm^2 and thickness of 0.2 cm). The top electrode was then placed, and the overflowing gel was carefully cleaned off with a Kimwipe. For the ionoelastomers, samples with area 0.785 cm^2 and thickness 0.3-0.5 mm were prepared by curing a thin layer of ion gel under 365 nm light for 55 min and cut into discs using a 1 cm diam. biopsy punch. In each measurement, the sample was placed between two stainless steel electrodes, sealed in a Metrohm TSC SW closed measuring cell, and connected to the cell holder. The frequency range was set from 5 MHz to 1 Hz and applied amplitude was 10 mV. The measurements were performed at room temperature. The results were displayed as Nyquist plots in ZView, and the ionic conductivity (σ) was calculated by taking the ratio between the thickness of sample (length of electrode gap, L) and the product of the resistance minima (Z_0) and sample area (A) (Equation 2).

$$\sigma = \frac{L}{Z_0 \cdot A} \tag{2}$$

3.3.12 Thermogravimetric Analysis

The thermal stabilities of the ionoelastomers with and without F127-BUM were determined by thermogravimetric analysis (TGA), which was carried out on a Mettler Toledo TGA/DSC 3+ Thermogravimetric Analyzer under N_2 atmosphere. Each sample of the ionoelastomers (masses 5-7 mg) were placed onto a tared standard aluminum pan and sealed. Starting at room temperature, the sample was then heated to 450 °C at a constant rate of 10 °C/min.

3.3.13 Direct-Write 3D Printing

Direct Ink Write 3D printing was performed on a modified Alunar i3 RepRap extrusion printer that has been retrofitted for pneumatic dispensation. G-codes were written through text editor for the lines and lattice structure, while the cylinders and shape-shifting constructs were originally created as a CAD file in SolidWorks 2019 and converted to G-codes via Slic3r. All printing was performed using the ion gel inks with an extrusion air pressure of 17-20 psi. The structures were printed with 0.3 mm layer height, with printing speeds at 6-10 mm/s. Upon completion of printing, the structures were irradiated under 365 nm light (at 3.4 $mW \cdot cm^{-2}$) for 55 min to polymerize the PILs and crosslink the network with F127-BUM, irreversibly fixing the structures.

3.3.14 Mechanical Characterization

An Instron 5585H 250 kN electro-mechanical test frame with a 200 N load cell was used to evaluate the mechanical properties of the ionoelastomers. All dogbone samples used in tensile tests were 5 mm long, 2 mm thick, and 2 mm wide in the narrow section. The dogbones were prepared by either extruding the ion gel into a dogbone mold or printed on the RepRap extrusion printer. The gel was then exposed to 365 nm light for 55 min. The sample was then attached to the pneumatic self-aligning grips fixed on the load frame with sandpaper and superglue. In tensile tests, the samples were subjected to increasing strain at a constant rate of 10 mm/min until mechanical failure of the sample. Additional dogbones were made and submerged in methanol for 7 days to extract any unpolymerized IL. Tensile tests were performed on extracted dogbones and compared to the original samples.

3.3.14 Extent of Shape Change in Bilayer Structures

All bilayer dogbone samples used in tensile tests were 10 mm long and 5 mm wide in the narrow section. The dogbones were printed on the RepRap extrusion printer, with one material per layer, setting layer height to 0.3 mm (thickness/layer). The printed parts were then exposed to 365 nm light for 55 min. The sample was then attached to the pneumatic self-aligning grips fixed on the Instron 5585H 250 kN electro-mechanical test frame with sandpaper and superglue. The samples were subjected to increasing strain at a constant rate of 10 mm/min until 50, 75, or 100% strain, then removed from the grips. After 1 minute, the photo of the bilayer is taken and the degree of bending is measured with ImageJ software.

3.4 RESULTS AND DISCUSSIONS

3.4.1 Synthesis and Photopolymerization of PILs

Three PILs [EVIM]BF_4, [BVIM]BF_4, and [HVIM]BF_4 were synthesized via neat S_N2 reaction[29,30] followed by anion exchange[31](Scheme 3.1). The first step involves an S_N2 quarternization reaction between vinyl imidazole and an alkyl halide, ran neat at elevated temperature. The unreacted starting material is extracted with diethyl ether. The second step is a simple anion exchange with sodium tetrafluoroborate, where sodium bromide is insoluble in acetone and can be filtered out before the solution is concentrated to obtain the product. The cation's side chain length were varied by changing the alkyl halide used in the S_N2 reaction. The vinyl group on the cation allows the PILs to polymerize via free radical polymerzation. When mixed with a small amount of HMP as the photoradical initiator, the PILs can be photocured when irridiated with 395 nm light to form an ionoelastomer. The polymerization is observable through

ATR-FTIR, where decrease in signals for vinyl C=C peaks at 1656 cm^{-1} suggest the PILs undergo photopolymerization when exposed to 395 nm light (Figure 3.2).

3.4.2 Formulation of Polymerizable Ion Gels

Three ion gel inks using PILs were developed, which were comprised of F127-BUM dissolved in [EVIM]BF_4, [BVIM]BF_4, or [HVIM]BF_4. The imidazolium ionic liquids possess vinyl groups that can undergo photo-initiated radical polymerization that can also co-polymerize with the methacrylate endgroups of F127-BUM to form a crosslinked polymerized ionic liquid network. Three different alkyl chain lengths were chosen as we hypothesized that these side chains would affect the viscoelastic and plastic properties of both the ion gel and the polymerized ionic liquid. Ion gels that were formed from [EVIM]BF_4 and [BVIM]BF_4 each required 27 wt% F127-BUM to achieve self-supporting gels. SAXS characterization of these ion gels showed multiple distinct signal peaks, which suggested the presence of F127-BUM micelles arranged in an ordered packing structure (Figure 3.3). The q-value ratios were summarized in Tables 3.1. The normalized Q-values roughly corresponding to 1, $1^{1/2}$, $3^{1/2}$, indicating a BCC arrangement, which is consistent with F127-based hydrogels that have been reported in the literature.[32,33] A higher loading of F127-BUM (37 wt%) was required when [HVIM]BF_4 was the solvent, which was likely due to the increased compatibility between the imidazolium cation and poly(propylene oxide) blocks of the triblock copolymer.

3.4.3 Characterization of Ion Gels Pre- and Post-Curing

To confirm good shear-thinning behavior during the printing process, rheometrical characterizations were performed on the ion gels. The frequency sweep experiments (Figure 3.4a) were first performed to confirm stability of the ion gels over a frequency range. The storage and loss moduli appeared steady over 0.0159-15.9 Hz, suggesting that results from future experiments done within this frequency range would not be affected by the frequency. Therefore, the strain-sweep and cyclic experiments discussed next were performed at 1 Hz. Oscillatory strain-sweep experiments (Figure 3.4b) displayed the gel-sol transition the ion gels experienced when extruded (at 11% oscillatory strain), and cyclic strain experiments (Figure 3.4c) showed that the gel-sol transition is fast and reversible over multiple cycles without significant hysteresis. The prior two properties are important in the printing process, as the gel must be able to flow through the nozzle then quickly recover its gel state after exiting the nozzle, and the transition should happen reproducibly each time pressure is applied. Lastly, viscosity vs. shear rate experiments (Figure 3.4d) showed the decreasing viscosity with increasing shear rate, confirming that the ion gels are shear-thinning.

EIS showed that the ionoelastomers retained ionic conductivity from the ILs. The calculated ionic conductivities obtained through EIS were summarized in Table 3.2, with examplary Nyquist plots of [EVIM]BF_4 ion gel before and after curing shown in Figure 3.5. Overall, they were found to be in the range of 10^{-3}–10^{-4} $S{\cdot}cm^{-1}$, which are typical values for ion gels containing nonconducting polymers. Additionally, due to increasing molecular weight, ion gels containing ILs with longer side chains have a lower density of charge carriers. Therefore, the ionic conductivity of the [BVIM]BF_4 ion gel is lower than the [EVIM]BF_4 ion gel, and [HVIM]BF_4 ion gel the lowest. After curing, the ionic conductivity for the polymerized systems decreased to 10^{-6}–10^{-7} $S{\cdot}cm^{-1}$, which was expected due to lower number of mobile ions.[34] However, the cured material containing [BVIM]BF_4 has higher ionic conductivity compared to [EVIM]BF_4. With increasing side chain length, the inter-chain spacing increases, as the glass transition temperature (T_g) of the material. It has been shown that the ionic conductivity of ionoelastomers are largely dependent on the T_g, although not exclusively.[35–37] The relationshop between ionic conductivity and T_g can be described by Vogel–Tamman–Fulcher (VTF) equation for polyelectrolytes (Equation 3):

$$\sigma = AT^{1/2}e^{-E_a/(T-T_g)} \tag{3}$$

Where σ is the ionic conductivity, A is the frequency factor, T is temperature, and E_a is the activation energy.[38] [HVIM]BF_4 ionoelastomer also has a lower ionic conductivity due to the larger amount of F127-BUM used.

Additionally, TGA suggests the ionoelastomers retained the thermal stability of the ionic liquids. The TGA plots looks very similar between the ionoelastomers (Figure 3.6a) and ionoelastomers with added F127-BUM (Figure 3.6b). Overall, the onsets of decomposition for the [EVIM]BF_4, [BVIM]BF_4, and [HVIM]BF_4 ion gels decreased by 16.9 °C, 18.5 °C, and 30.6 °C, respectively, with addition of F127-BUM (Table 3.3). Despite a significant amount of F127-BUM added, these onset temperatures are much higher than that of pure F127, which is at 200 °C.[39,40] The presence of the polymerized ILs contribute to a marked increase in thermal stability of the ionoelastomers.

3.4.4 DIW Printing

The ion gels were printed using a pneumatic DIW system. Multi-layered constructs were successfully printed with an extruded filament diameter of ~0.4-0.6 mm (0.26 mm I.D. nozzle, 0.3 mm layer height), and did not require photo-curing between layer deposition. All structures were printed with 0.3 mm layer height. The [EVIM]BF_4 (Figure 3.7a) and [BVIM]BF_4 (Figre 3.7b) ion gels afforded successful multi-layered objects up to 20 layers, and the viscoelastic properties of the printed ion gel supported overhanging features. The softer [HVIM]BF_4 ion gel afforded constructs containing up to 8 layers with good layer-to-layer integrity (Figure 3.7c).

3.4.5 Mechanical Characterization of Casted Bulk vs. Printed Parts

All multi-layered constructs were UV-cured after they were entirely printed to encourage isotropic mechanical properties. A single post-print UV-cure reduces the interlayer defects, which is a common source of mechanical weakness in structures printed via 3D printing. Dogbone samples of each ion gel were casted in a mold and 3D printed in two different directions, and then characterized via tensile tests as is shown in Figure 38. The cured [EVIM]BF_4 PIL exhibits the stiffest response, with an elastic modulus of approximately 550 MPa, whereas the polymerized [BVIM]BF_4 and [HVIM]BF_4 ionoelastomers were almost an order of magnitude less stiff, with elastic moduli of 68 and 34 MPa, respectively. All three polymers exhibited a highly ductile response, wherein the [EVIM]BF_4 ionoelastomer showed the lowest ultimate strain, followed by the [HVIM]BF_4 then [BVIM]BF_4 ionoelastomers (Table 3.4). The differences in quasi-static mechanical properties between the different elastomers can be explained based on the size of the cation's alkyl side chain length. The [HVIM]BF_4 ionoelastomer, having the longest alkyl group of the set, consequently had the lowest T_g and thus the greatest amount of material flexibility.[35] We also observed that the mechanical properties of the ionoelastomers were independent of the method of dogbone fabrication, specifically, whether they were printed vertically, horizontally, or casted in a mold.

In comparison to other ionoelastomers, our materials appeared more flexible. We hypothesized that the increased flexibility in the materials are from the ILs that are not fully incorporated into the polymer network after curing. The unpolymerized ILs can disrupt point interactions between polymerized IL chains and increase distance between polymer chain backbones, which results in increased flexibility in the material. Gel fraction experiments were done to observe the difference in weight of the cured materials after 7 days of submersion in methanol. In all materials, approximately 90 wt% of the material was retained (Table 3.4), suggesting that 10 wt% of the materials were unpolymerized ILs that were leached out into methanol. We further confirmed this hypothesis by submerging dogbone samples in methanol for 48 h, and subjecting the samples to tensile tests after drying (Figure 3.9). Upon removal of residual ionic liquid, all of the samples showed increased elastic moduli and decreased ultimate strain, while maintaining a generally ductile response

3.4.6 Shape Recovery Properties

The tensile experiments further revealed that all of the ionoelastomers exhibited a varied time dependent (and generally nonlinear viscoelastic) recovery toward their original shape, as can be seen in Figure 3.10. All three polymers showed an initial, relatively rapid, partial shape recovery from 150% strain within the first 10 seconds, with the [EVIM]BF_4 and [BVIM]BF_4 ionoelastomers returning to 100% strain and the [HVIM]BF_4 ionoelastomer to 55% strain. After this initial rapid recovery, the viscoelastic recovery becomes slower and more varied between the three samples. After 120 hours, the [EVIM]BF_4 ionoelastomer, which exhibits the slowest recovery, retains approximately 54% strain, which suggests a partially plastic response. In contrast, the [BVIM]BF_4 and [HVIM]BF_4 ionoelastomers exhibited nearly full shape recovery after 2 hours, with the [HVIM]BF_4 ionoelastomer showing the faster recovery. While [EVIM]BF_4, [BVIM]BF_4, and [HVIM]BF_4 polymerized to form linear chains, the F127-BUM serves as a crosslinker in this polymer network and provides the ‘memory’ of the original shape of the object. We suggest the variable time-dependent recovery is likely due to the transient charge interactions between polymerized IL chains. The larger butyl and hexyl groups can shield the cation, which leads to higher mobility of the chains.

3.4.7 Fabrication of Shape-Morphing Bilayer Constructs

The differences in mechanical properties of the cured ion gel were utilized to print bilayers that were programmed via 3D printing to undergo mechano-activated shape changes. For example, a bilayer construct comprised of a [BVIM]BF_4 layer printed onto a [EVIM]BF_4 layer was cured and then mechano-activated by stretching (150% strain) and releasing the film. The combination of the plastic deformation of the [EVIM]BF_4 layer and the viscoelastic recovery of the [BVIM]BF_4 led to permanent bending of the bilayer construct in the direction of the elastomeric layer. The extent of curvature was dependent upon the applied strain, wherein smaller bending angles were produced with small strains (50%) and larger bending angles at higher strains (100% strain) (Figure 3.11).

The multi-material DIW printing process also enables the programming of more complex mechano-activated multidirectional shape-morphing. For example, we printed alternating parallel lines of [EVIM]BF_4 and [BVIM]BF_4 ion gels at a 135° angle on top of a [BVIM]BF_4 ion gel layer. The bilayer was UV-cured and then mechano-activated to fold into a helical structure, as is shown in Figure 3b. Bilayers were also programmed via 3D printing to encode letters that were revealed upon mechano-activation (Figure 3.12). A “U”, which requires bending in one direction was created by printing [BVIM]BF_4 ion gel on the upper layer in the region where the bend was desired. On the other hand, a “W” required the spatial localization of the [BVIM]BF_4 ion gel within both layers, in different locations, in order to facilitate the bending in opposite directions. Strain-concentrating regions were incorporated into the design in this case to maximize the strain incurred to the intended bending region, and minimize the strain incurred to the intended straight regions, under application uniaxial tensile load at the edges of the sample.

3.5 CONCLUSION

In summary, we have used multi-material DIW, enabled by polymerizable ion gels, to program the mechano-activated multidirectional folding of planar structures into 3D shapes. The polymerizable ion gels that were developed for this application exhibited variable viscoelastic or viscoelastic-plastic behaviors upon the application and release of a tensile load. The ability to control the viscoelastic and plastic response of the constituent materials of the printed morphing structure offers significant potential benefit, wherein future, time-dependent, sequential folding or autonomous origami schemes can be envisioned. The ion gels exhibited good shear-thinning behavior with rapid transitions between the gel- and sol-states. Mechanical characterization performed on cured structures confirmed minimal interlayer defects were introduced during the printing process. The ionic liquid within the ion gel was polymerized during a post-print UV cure, which led to objects with a high degree of isotropy. Unlike other methods of producing objects that undergo mechanically induced shape changes, our approach does not require pre-stretching before or during fabrication. Thus, the full capabilities of 3D printing can now be used to program more complex geometrical changes upon mechano-activation.

3.6 ACKNOWLEDGEMENTS

Adapted with permission from Wong, J.; Basu, A.; Wende, M.; Boechler, N.; Nelson, A. Mechano-Activated Objects with Multidirectional Shape Morphing Programmed via 3D Printing. *ACS Appl. Polym. Mater.* **2020**, *7*, 2504. Copyright 2020 American Chemical Society.

3.7 REFERENCES

(1) Kuang, X.; Roach, D. J.; Wu, J.; Hamel, C. M.; Ding, Z.; Wang, T.; Dunn, M. L.; Qi, H. J. Advances in 4D Printing: Materials and Applications. *Adv. Funct. Mater.* **2019**, *29*, 1805290.

(2) Zhang, Z.; Demir, K. G.; Gu, G. X. Developments in 4D-printing: a review on current smart materials, technologies, and applications. *Int. J. Smart Nano. Mater.* **2019**, *3*, 205–224.

(3) Joshi, S.; Rawat, K.; Karunakaran, C.; Rajamohan, V.; Mathew, A. T.; Koziol, K.; Thakur, V. K.; Balan, A.S.S. 4D printing of materials for the future: Opportunities and challenges. *Applied Materials Today* **2020**, *18*, 100490.

(4) Peng, B.; Yang, Y.; Gu, K.; Amis, E. J.; Cavicchi, K. A. Digital Light Processing 3D Printing of Triple Shape Memory Polymer for Sequential Shape Shifting. *ACS Materials Lett.* **2019**, *1*, 410–417.

(5) Wang, Z. J.; Hong, W.; Wu, Z. L.; Zheng, Q. Site-Specific Pre-Swelling-Directed Morphing Structures of Patterned Hydrogels. *Angew. Chem. Int. Ed.* **2017**, *56*, 15974–15978.

(6) Pezzulla, M.; Shillig, S. A.;Nardinocchia, P.; Holmes. Morphing of geometric composites via residual swelling. *Soft Matter* **2015**, *11*, 5812−5820.

(7) Davidson, E. C.; Kotikian, A.; Li, S.; Aizenberg, J.; Lewis, J. A. 3D Printable and Reconfigurable Liquid Crystal Elastomers with Light-Induced Shape Memory via Dynamic Bond Exchange. *Adv. Mater.* **2020**, *32*, 1905682.

(8) Kim, Y.; Yuk, H.; Zhao, R.; Chester, S. A.; Zhao, X. Printing ferromagnetic domains for untethered fast-transforming soft materials. *Nature* **2018**, *558*, 274–279.

(9) Wang, L.; Zhou, W.; Tang, Q.; Yang, H.; Zhou, Q.; Zhang, X. Rhodamine-Functionalized Mechanochromic and Mechanofluorescent Hydrogels with Enhanced Mechanoresponsive Sensitivity. *Polymers* **2018**, *10*, 994.

(10) Barbee, M. H.; Mondal, K.; Deng, J. Z.; Bharambe, V.; Neumann, T. V.; Adams, J. J.; Boechler, N.; Dickey, M. D.; Craig, S. L. Mechanochromic Stretchable Electronics. *ACS Appl. Mater. Interfaces* **2018**, *10*, 29918−29924.

(11) Meira, R. M.; Correia, D. M.; Ribeiro, S.; Costa, P.; Gomes, A. C.; Gama, F. M.; Lanceros-Méndez, S.; Ribeiro, C. Ionic-Liquid-Based Electroactive Polymer Composites for Muscle Tissue Engineering. *ACS Appl. Polym. Mater.* **2019**, *1*, 2649−2658.

(12) Hu, X.; Zeng, T.; Husic, C. C.; Robb, M. J. Mechanically Triggered Small Molecule Release from a Masked Furfuryl Carbonate. *J. Am. Chem. Soc.* **2019**, *141*, 15018−15023.

(13) Mohanraj, B.; Duan, G.; Peredo, A.; Kim, M.; Tu, F.; Lee, D.; Dodge,G. R.; Mauck, R. L. Mechanically Activated Microcapsules for “On-Demand” Drug Delivery in Dynamically Loaded Musculoskeletal Tissues. *Adv. Funct. Mater.* **2019**, *29*, 1807909.

(14) Diesendruck, C. E.; Steinberg, B. D.; Sugai, N.; Silberstein, M. N.; Sottos, N. R.; White, S. R.; Braun, P. V.; Moore, J. S. Proton-Coupled Mechanochemical Transduction: A Mechanogenerated Acid. *J. Am. Chem. Soc.* **2012**, *134*, 12446−12449.

(15) Rohde, R. C.; Basu, A.; Okello, L. B.; Barbee, M. H.; Zhang, Y.; Velev, O. D.; Nelson, A.; Craig, S. L. Mechanochromic composite elastomers for additive manufacturing and low strain mechanophore activation. *Polym. Chem.* **2019**, *10*, 5985–5991.

(16) Peterson, G. I.; Larsen, M. B.; Ganter, M. A.; Storti, D. W.; Boydston, A. J. 3D-Printed Mechanochromic Materials. *ACS Appl. Mater. Interfaces* **2015**, *7*, 577−583.

(17) Stafford, C. M.; Harrison, C.; Beers, K. L.; Karim, A.; Amis, E. J.; Vanlandingham, M. R.; Kim, H. C.; Volksen, W.; Miller, R. D.; Simonyi, E. E. A buckling-based metrology for measuring the elastic moduli of polymeric thin films. *Nat. Mater.* **2009**, *3*, 545−550.

(18) Cafferty, B. J.; Campbell, V. E.; Rothemund, P.; Preston, D. J.; Ainla, A.; Fulleringer, N.; Diaz, A. C.; Fuentes, A. E.;Sameoto, D.; Lewis, J. A.; Whitesides, G. M. Fabricating 3D Structures by Combining 2D Printing and Relaxation of Strain. *Adv. Mater. Technol.* **2019**, *4*, 1800299.

(19) Yin, L.; Kumar, R.; Karajic, A.; Xie, L.; You, J.; Joshuia, D.; Lopez, C. S.; Miller, J.; Wang, J. From All-Printed 2D Patterns to Free-Standing 3D Structures: Controlled Buckling and Selective Bonding. *Adv. Mater. Technol.* **2018**, *3*, 1800013.

(20) Huang, J.; Liu, A.; Kroll, B.; Bertoldi, K.; Clarke, D. R. Spontaneous and deterministic three-dimensional curling of pre-strained elastomeric bi-strips. *Soft Matter* **2012**, *8*, 6291−6300.

(21) Al-Rashed, R.; Jiménez, F. L.; Marthelot, J.; Reis, P. M. Buckling patterns in biaxially pre-stretched bilayer shells: wrinkles, creases, folds and fracture-like ridges. *Soft Matter* **2017**, *13*, 7969–7978.

(22) Robertson, J. M.; Torbati, A. H.; Rodriguez, E. D.; Mao, Y.; Baker, R. M.; Qi, J.; Mather, P. T. Mechanically programmed shape change in laminated elastomeric composites. *Soft Matter* **2015**, *11*, 5754−5764.

(23) Wisinger, C. E.; Maynarda, L. A.; Barone, J. R. Bending, curling, and twisting in polymeric bilayers. *Soft Matter* **2019**, *15*, 4541−4547.

(24) Wong, J.; Gong, A. T.; Defnet, P. A.; Meabe, L.; Beauchamp, B.; Sweet, R. M.; Sardon, H.; Cobb, C. L.; Nelson, A. 3D Printing Ionogel Auxetic Frameworks for Stretchable Sensors. *Adv. Mater. Technol.* **2019**, *4*, 1900452.

(25) Bideau, J. L.; Viau, L.; Vioux, A. Ionogels, ionic liquid based hybrid materials. *Chem. Soc. Rev.* **2011**, *40*, 907−925.

(26) Ueki, T.; Watanabe, M. Polymers in Ionic Liquids: Dawn of Neoteric Solvents and Innovative Materials. *Bull. Chem. Soc. Jpn.* **2012**, *85*, 33−50.

(27) Marr, P. C.; Marr, A. C. Ionic liquid gel materials: applications in green and sustainable chemistry. *Green Chem.* **2016**, *18*, 105−128.

(28) Hexemer, A.; Bras, W.; Glossinger, J.; Schaible, E.; Gann, E.; Kirian, R.; MacDowell, A.; Church, M.; Rude, B.; Padmore, H. A SAXS/WAXS/GISAXS Beamline with Multilayer Monochromator. *J. Phys. Conf. Ser.* **2010**, *247*, 012007.

(29) Ren, Y.; Guo, J.; Liu, Z.; Sun, Z.; Wu, Y.; Liu, L.; Yan, F. Ionic liquid-based click-ionogels. *Sci. Adv.* **2019**, *5*, eaax0648.

(30) Fang, J.; Lyu, M.; Wang, X.; Wu, Y.; Zhao, J. Synthesis and Performance of Novel Anion Exchange Membranes Based on Imidazolium Ionic Liquids for Alkaline Fuel Cell Applications. *J. Power Sources* **2015**, *284*, 517−523.

(31) Min, G.-H.; Yim, T.; Lee, H. Y.; Huh, D. H.; Lee, E.; Mun, J.; Oh, S. M.; Kim, Y. G. Synthesis and Properties of Ionic Liquids: Imidazolium Tetrafluoroborates with Unsaturated Side Chains. *Bull. Korean Chem. Soc.* **2006**, *27*, 847−851.

(32) Mortensen, K.; Batsberg, W.; Hvidt, S. Effects of PEO-PPO Diblock Impurities on the Cubic Structure of Aqueous PEO-PPO-PEO Pluronics Micelles: fcc and bcc Ordered Structures in F127. *Macromolecules* **2008**, *41*, 1720–1727.

(33) Liu, T.; Chu, B. Formation of homogeneous gel-like phases by mixed triblock copolymer micelles in aqueous solution: FCC to BCC phase transition. *J. Appl. Cryst*. **2000**, *33*, 727–730.

(34) Yuan, Y.; Antonietti, M. Poly(ionic liquid)s: Polymers expanding classical property profiles. *Polymer* **2011**, *52*, 1469

(35) Salas-de la Cruz, D.; Green, M. D.; Ye, Y.; Elabd, Y. A.; Long, T. E.; Winey, K. I. Correlating Backbone-to-backbone Distance to Ionic Conductivity in Amorphous Polymerized Ionic Liquids. *J. Polym. Sci. Pol. Phys.* **2012**, *50*, 338–346.

(36) U. H. Choi, A. Mittal, T. L. Price Jr., M. Lee, H. W. Gibson, J. Runt, R. H. Colby. Molecular Volume Effects on the Dynamics of Polymerized Ionic Liquids and their Monomers. *Electrochimica Acta* **2015**, *175*, 55–61.

(37) Jourdain, A.; Serghei, A.; Drockenmuller, E. Enhanced Ionic Conductivity of a 1,2,3-Triazolium-Based Poly(siloxane ionic liquid) Homopolymer. *ACS Macro Lett.* **2016**, *5*, 1283–1286.

(38) Lua, J.; Yana, F.; Texter, J. Advanced applications of ionic liquids in polymer science. *Prog. Polym. Sci.* **2009**, *34*, 431–448.

(39) Hendricks, N. R.; Watkins, J. J.; Carter, K. R. Formation of hierarchical silica nanochannels through nanoimprint lithography. *J. Mater. Chem.* **2011**, *21*, 14213.

(40) Dou, Q.; Karim, A. A.; Loh, X. J. Modification of Thermal and Mechanical Properties of PEG-PPG-PEG Copolymer (F127) with MA-POSS. *Polymers* **2016**, *8*, 341.

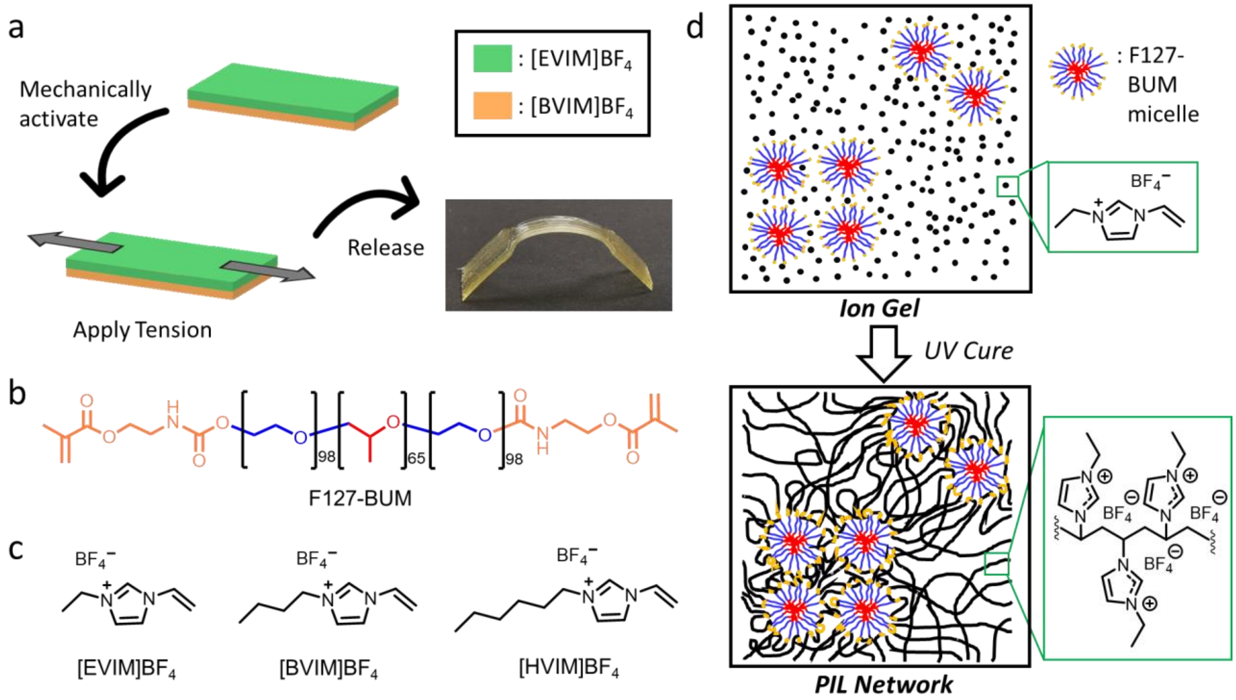

Figure 3.1 Strategy towards shape change and chemical compositions of the materials. a) Upon stretching and releasing the bilayer, the shape memory materials recover at different rates and to different degrees, allowing the bilayer to bend towards the side that recovers the most. The ion gels used to fabricate these structures were comprised of (b) an F127-based triblock copolymer with bisurethane methacrylate chain ends (F127-BUM) and (c) one of the following ILs: 1-ethyl-3-vinylimidazolium tetrafluoroborate ([EVIM]BF_4), 1-butyl-3-vinylimidazolium tetrafluoroborate ([BVIM]BF_4), or 1-hexyl-3-vinylimidazolium tetrafluoroborate ([HVIM]BF_4). d) The ion gel was shear-thinning and comprised F127-BUM micelles dispersed in the IL. After UV cure (365 nm), the methacrylate chain ends of F127-BUM and IL co-polymerize to form a shape memory polymeric network.

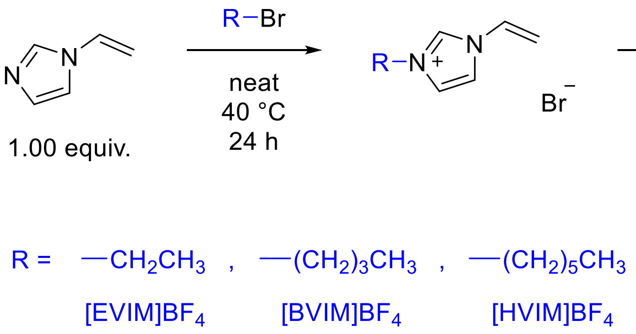

Scheme 3.1 Synthesis of polymerizable ILs. The first step involves an S_N2 quarternization reaction, ran neat at elevated temperature. The second step is a simple anion exchange with sodium tetrafluoroborate in acetone.

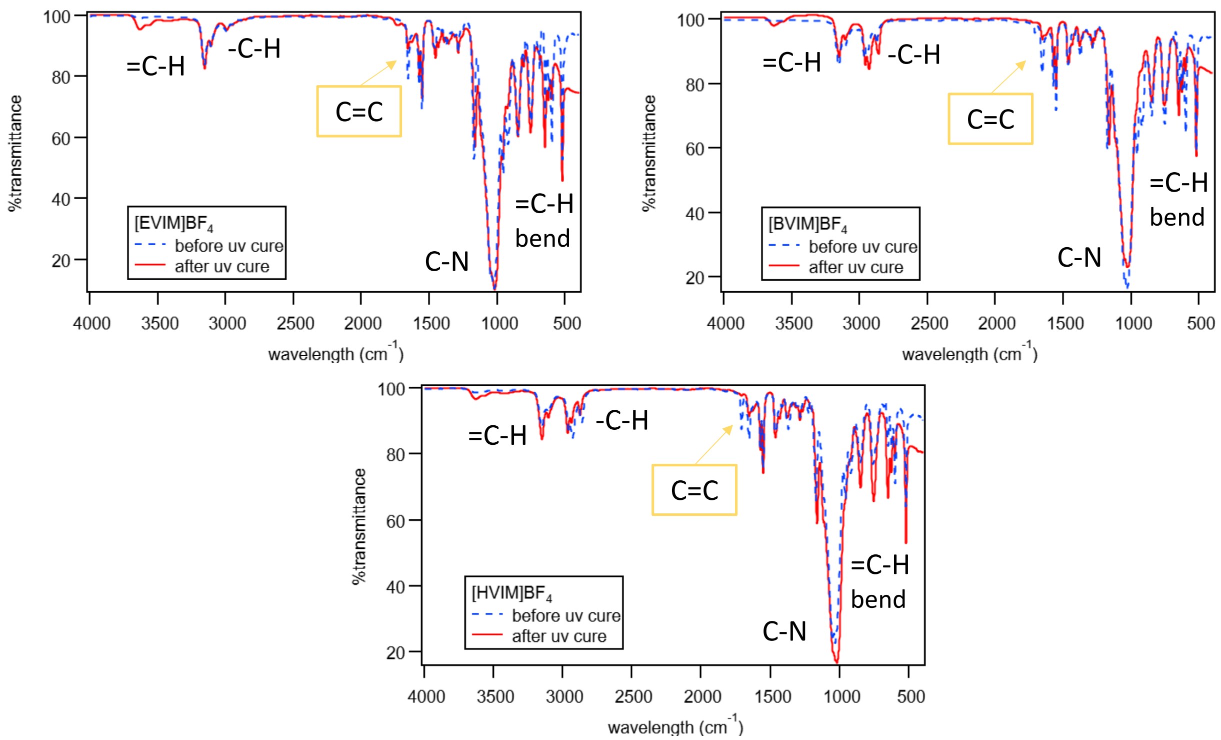

Figure 3.2 ATR-FTIR spectra for the polymerizable ILs before and after UV curing. The disappearance of C=C bond suggests successful polymerization of the cation's vinyl group to create a continuous polymer network.

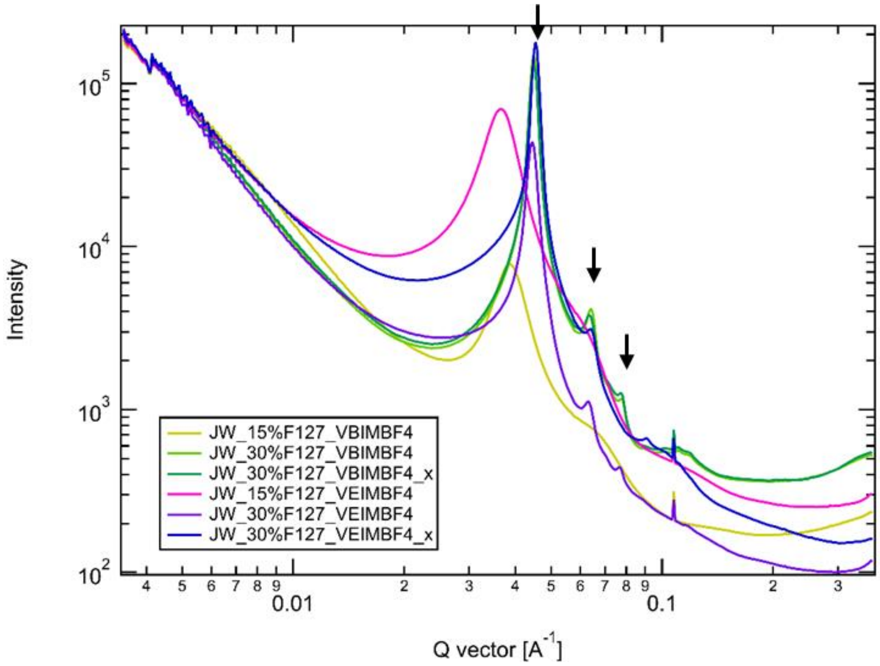

Figure 3.3 SAXS data plot of 15 wt% F127-BUM in [EVIM]BF$_4$ and [BVIM]BF$_4$ (solution), 30 wt% F127-BUM in [EVIM]BF$_4$ and [BVIM]BF$_4$ (ion gel), and 30 wt% F127-BUM in [EVIM]BF$_4$ and [BVIM]BF$_4$ (x = cured). The broad peaks for the polymer solutions suggest presence of free floating micelles, while multiple, sharp peaks for the ion gel suggest BCC packing of the micelles that leads to gelation.

[EVIM]BF$_4$ Q-value (A^{-1})	[EVIM]BF$_4$ dist. (Å)	[EVIM]BF$_4$ normalized Q-ratio	[BVIM]BF$_4$ Q-value (A^{-1})	[BVIM]BF$_4$ dist. (Å)	[BVIM]BF$_4$ normalized Q-ratio
0.044527	141.110	1	0.044947	139.791	1
0.063015	99.709	1.415 (~$\sqrt{2}$)	0.064209	97.855	1.429 (~$\sqrt{2}$)
0.077644	80.923	1.744 (~$\sqrt{3}$)	0.077468	81.107	1.724 (~$\sqrt{3}$)

Table 3.1 Q values, micelle-to-micelle distance, and normal Q-ratios for 30% F127-BUM in [EVIM]BF$_4$, [BVIM]BF$_4$

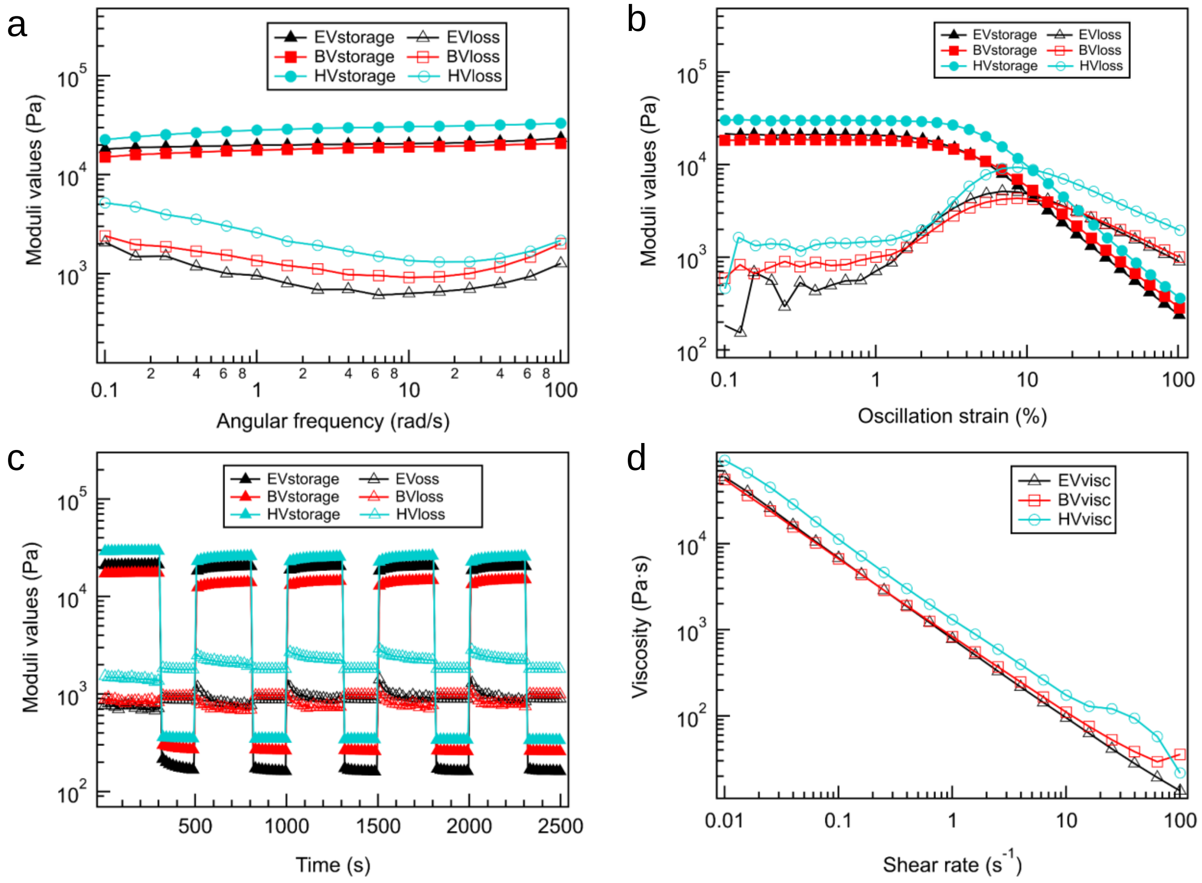

Figure 3.4 Rheometric characterizations on the PIL inks. (a) Frequency sweep experiment showing stable storage moduli values. (b) Oscillatory strain sweep experiment on the ion gels showing the storage and loss moduli as a function of strain, showing the gel-sol transition that enables printing. (c) Cyclic experiment to show that the transition is fast and reversible, and (d) a viscosity vs. shear rate to model the shear thinning behaviours.

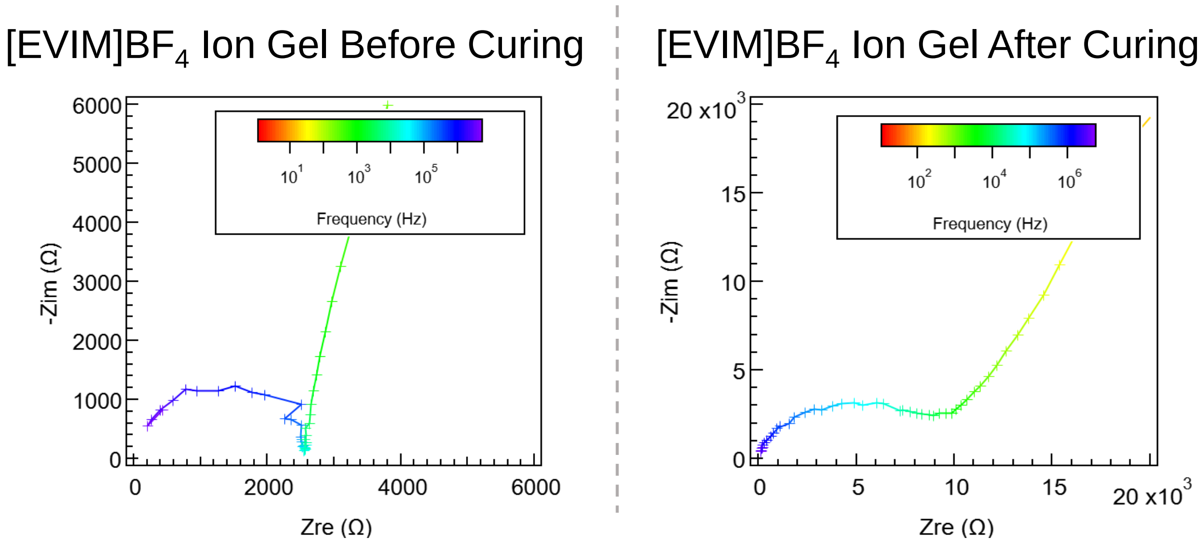

Figure 3.5 Representative Nyquist plots from EIS measurement on the ion gels before and after curing. After cure, the plot shows significantly higher resistance (Z_{re} as $-Z_{im} \rightarrow 0$ Ω), which leads to lower ionic conductivity.

Composition	σ gel (×10^{-3} S·cm^{-1})	σ cured (×10^{-6} S·cm^{-1})
[EVIM]BF_4 +27% F127-BUM	3.12±0.09	2.26±0.67
[BVIM]BF_4 +27% F127-BUM	1.41±0.04	8.08±0.92
[HVIM]BF_4 +37% F127-BUM	0.38±0.02	5.32±0.66

Table 3.2 Calculated ionic conductivity values (σ) for both the ion gels and cured products.

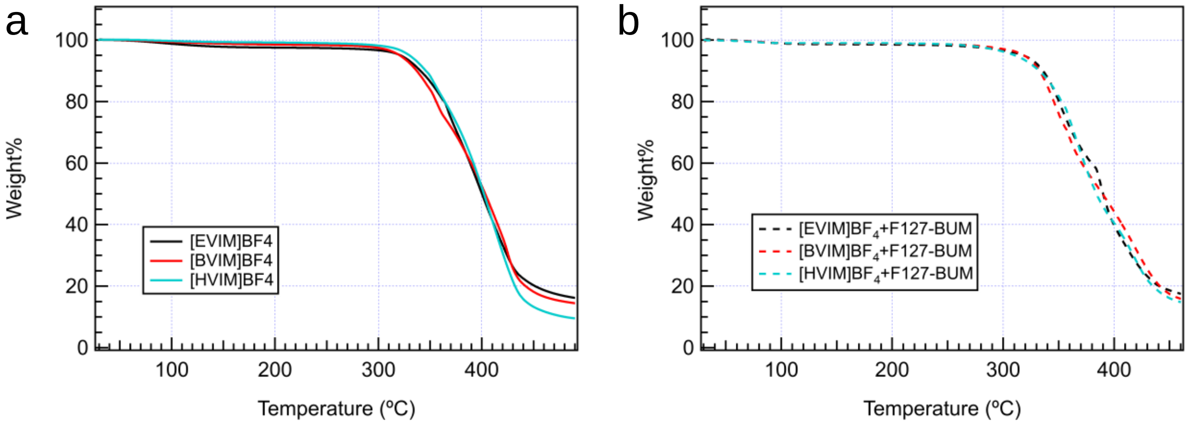

Figure 3.6 TGA plots for the ionoelastomers without F127-BUM (a) and with F127-BUM crosslinks (b).

Polymerized IL	T_{onset} ionoelastomer, no F127-BUM	T_{onset} ionoelastomer + F127-BUM	Δ
p([EVIM]BF_4)	343.98 °C	327.06 °C	16.92 °C
p([BVIM]BF_4)	347.69 °C	329.20 °C	18.49 °C
p([HVIM]BF_4)	355.63 °C	325.03 °C	30.60 °C

Table 3.3 Decomposition temperature onsets for both the cured ion gels with and without added F127-BUM and the calculated differences.

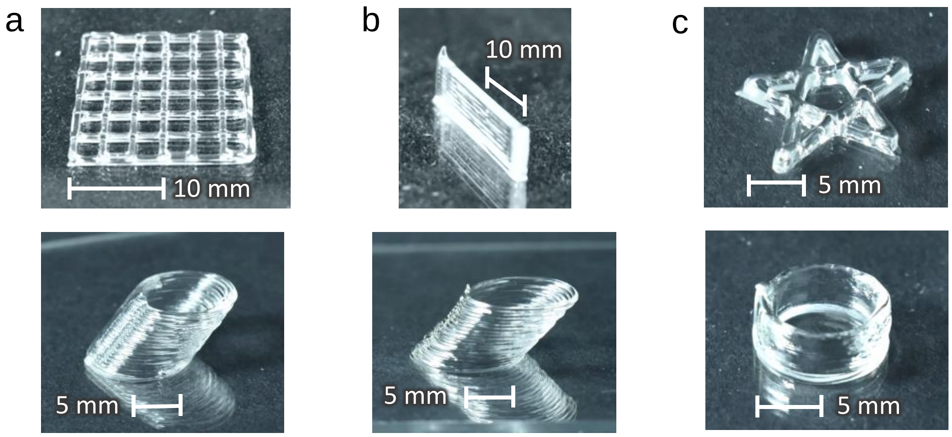

Figure 3.7 Example prints including (a) a 2-layer perpendicular serpentine structure and a 20-layer offset cylinder with a 40° overhang ($[EVIM]BF_4$ ion gel), (b) a 20-layer single line and a 20-layer offset cylinder with a 40° overhang ($[BVIM]BF_4$ ion gel), (c) an 8-layer 5-pointed star and a 20-layer straight cylinder ($[HVIM]BF_4$ ion gel).

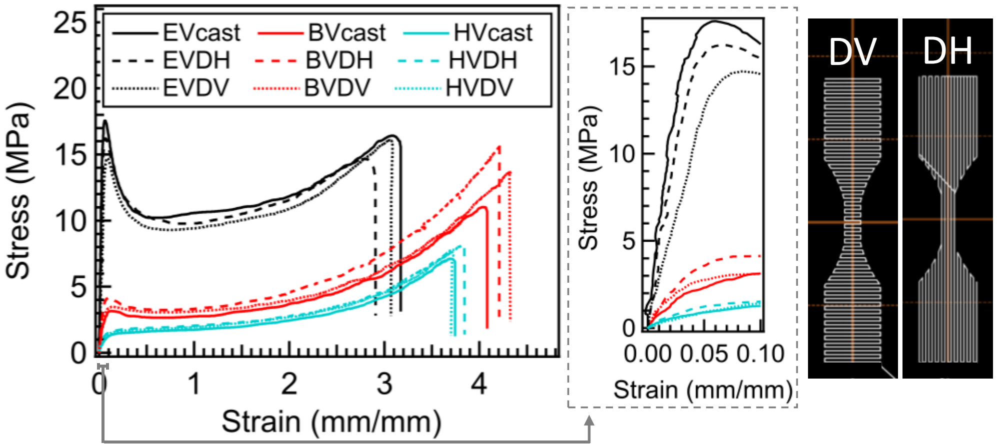

Figure 3.8 Stress-strain curves of the cured materials are shown for dogbone samples that were casted, printed perpendicular (DH), or printed parallel (DV) to the axis of applied strain. The similarity between tensile curves for each sample shows the advantage of curing at once after the printing to minimize interlayer defects and anisotropy in printing direction.

Composition	Young's Modulus (MPa)	Ultimate Strain (mm/mm)	Gel Fraction (7 days)
[EVIM]BF_4 + 27% F127-BUM	552.05±31.04	2.99±0.17	89.0±1.31%
[BVIM]BF_4 + 27% F127-BUM	68.02±10.78	4.08±0.38	89.6±0.38%
[HVIM]BF_4 + 37% F127-BUM	34.44±7.08	3.51±0.30	89.9±0.86%

Table 3.4 Young's moduli and ultimate strains from tensile tests on casted dogbones, and gel fraction taken after submerging PILs in methanol for 7 days and drying overnight at 70 °C.

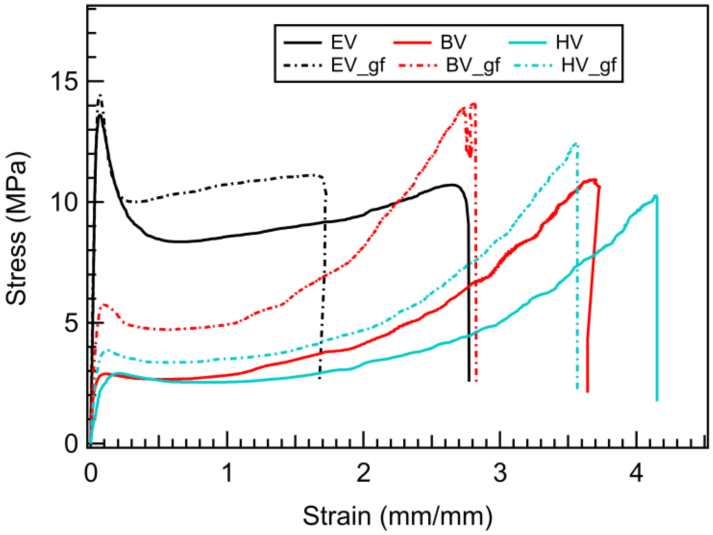

Figure 3.9 Tensile plots for dogbones directly after uv curing (solid lines) and gel fraction dogbones that have been extracted with methanol for 48 h and dried overnight (dashed lines).

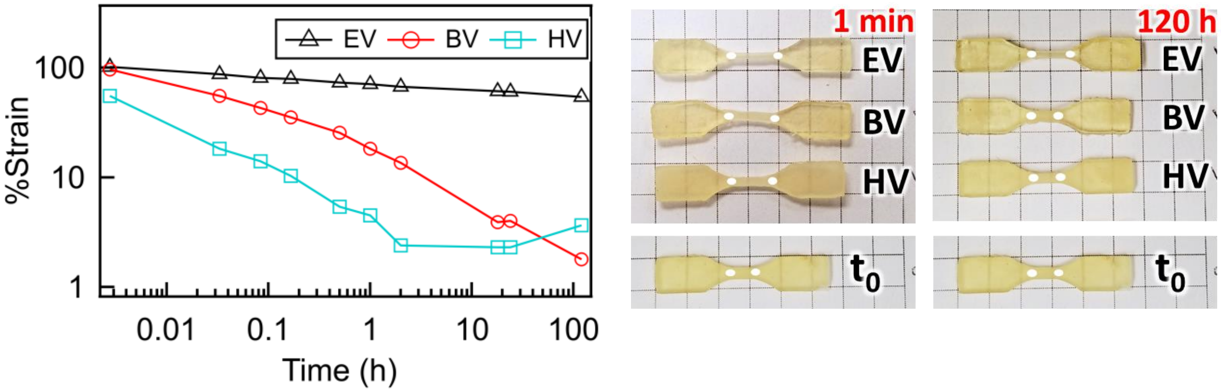

Figure 3.10 To observe the shape recovery of the cured structures, casted dogbones were stretched to 150% strain and released. The lengths of the dogbone’s narrow sections were monitored and the shape recovery as a function of time for the ion gels are plotted to show the difference in speed and extent of recovery.

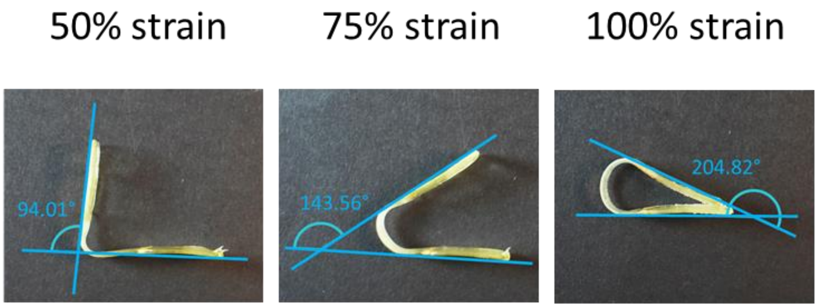

top: BV, bottom: EV

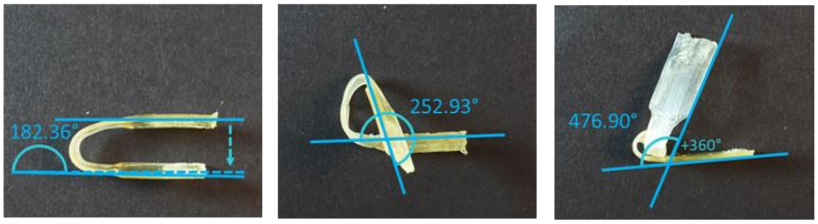

top: HV, bottom: EV

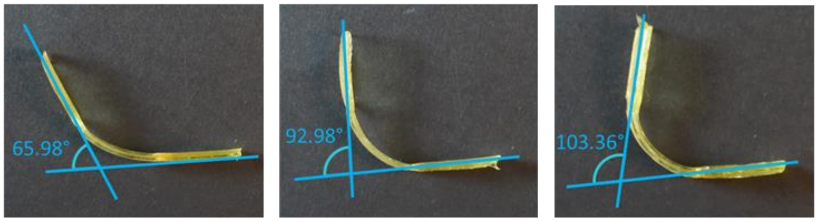

top: HV, bottom: BV

Figure 3.11 Printed bilayer strips can be stretched to 50%, 75%, and 100% strain. Upon release of tension, the structures bends. The amount of bending can be controlled by the magnitude of applied strain and the combination of selected materials.

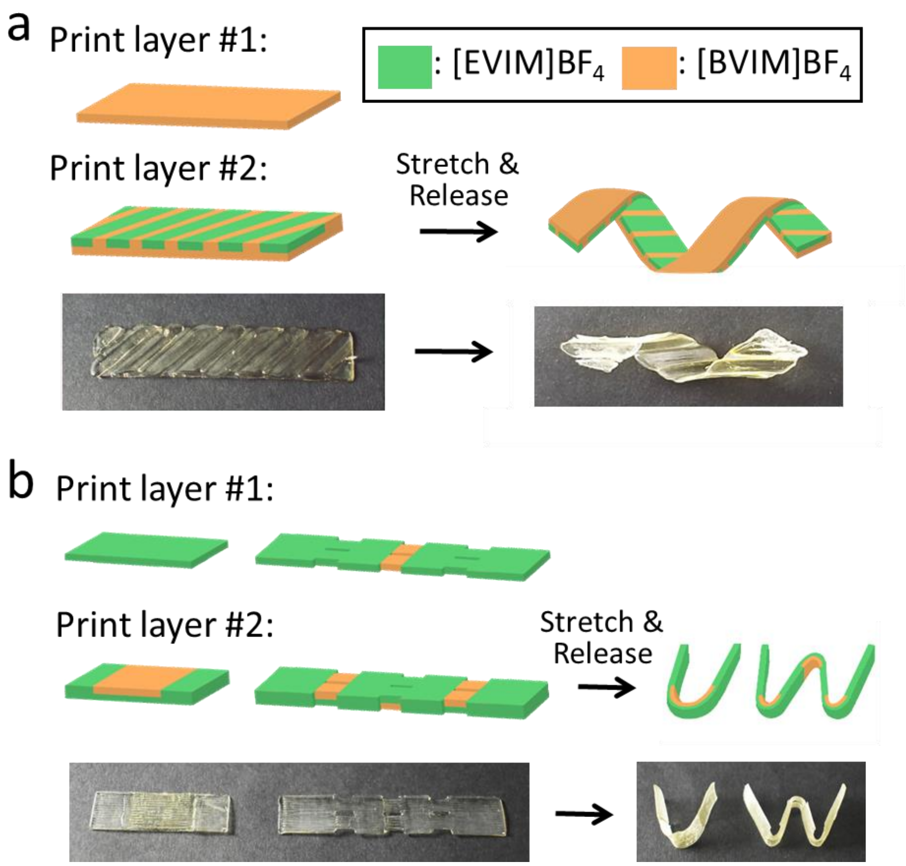

Figure 3.12 Mechano-activated shape transformation into (a) a helical ribbon, and (b) planar constructs that were encoded to transform into a “U” and a “W”.

CHAPTER 4: **PHOTOCURING 3D PRINTED OPAQUE COMPOSITE NETWORKS VIA TRIPLET FUSION UPCONVERSION**

4.1 ABSTRACT

High energy photons (λ<400 nm) are frequently used to initiate free radical polymerizations to form polymer networks, but is only effective for transparent objects. This poses major challenges to photochemically modify the physicochemical and mechanical properties of particle-reinforced composite networks since deep light penetration of short-wavelength photons is stifled. Herein, we employ the unconventional, yet versatile multiexciton process of triplet-triplet annihilation upconversion (TTA-UC) for curing opaque hydrogel composites created by direct-ink-write (DIW) 3D printing. TTA-UC mediates the conversion of low-energy red light (λ_{max} = 660 nm) for deep-penetration into higher-energy blue light to initiate free radical polymerizations within opaque objects. As proof-of-principle, hydrogels containing up to 15 wt% TiO_2 filler particles and doped with TTA-UC chromophores were readily cured with red light, while composites without the chromophores and TiO_2 loadings as little as 1-2 wt% remained uncured. Importantly, this method has wide potential to modify the chemical and mechanical properties of complex DIW 3D-printed polymer-particle composites.

4.2 INTRODUCTION

Additive manufacturing (AM or 3D printing) involves selective deposition of materials in a layer-by-layer fashion to create customizable structures with precise 3-dimensional control. As AM evolved from a rapid prototyping process to a key driver towards the next industrial revolution, massive effort and progress have been made towards developing advanced printable materials.[1–6]

In many AM techniques, printing robust 3D objects relies on the formation of polymer networks via photoinitiated radical polymerizations to achieve the desired mechanical properties.[7,8] Photopolymerization is a preferred method as it is fast and can be done at ambient temperature with spatiotemporal control. Network formation can occur during the printing process, in which patterned light is used to generate the 3D object.[9,10] Alternatively, network formation can be photoinitiated in a post-print cure step that occurs after the printing process is complete.[11,12] Both of these processes commonly use high energy light with wavelengths below ≤405 nm to generate radicals that initiate polymerization.[13–15] However, light penetration depth becomes increasingly critical in the fabrication of objects with homogeneous mechanical properties as the thickness of the printed part exceeds millimeter length scales. Most materials (including biological tissues) scatter light with smaller wavelengths via Mie and Rayleigh scattering.[16,17] Hence, photopolymerization with high energy light can require a longer exposure time or higher intensity, which increases energy consumption, risks dehydration of the hydrogels, and causes issues related to degradation.[18] While homogenous curing of thick and/or visually opaque materials to create uniform polymer networks would be beneficial for applications in particle composites or tissue engineering, this capability remains a significant challenge for the AM field.

Triplet-triplet annihilation upconversion (TTA-UC) is a process that effectively converts low energy photons[19] (long wavelength) into high-energy excitons, which can then emit short-wavelength irradiation or undergo energy transfer processes. Thus, we reason that this mechanism could present a facile methodology to cure polymer networks using conventional long-wavelength irradiation sources, devoid of highly specialized photochemical equipment. For example, two-photon polymerization (TPP) utilizes takes advantage of the deep penetration of red and infrared light to fabricate 3D objects.[20–24] However, the necessity for a single molecule to simultaneously absorb two photons requires an expensive laser set-up with high fluences. Similarly, Zhu, et al. demonstrated an application of DIW printing of pigmented inks using NIR-driven upconversion with inorganic nanoparticles.[25] Although upconversion using inorganic nanoparticles can also initiate photopolymerization with low energy photons[26], this technique requires a high excitation power density and has a lower absorption of visible excitation light and quantum yield.[19] Alternatively, TTA-UC involves two chromophores[27], a sensitizer and an annihilator, and benefits from the high extinction coefficient of the sensitizers and excitation at a relatively low light fluence.[28] The ability to employ TTA-UC to initiate polymerizations is rapidly gaining traction due to the versatility of the systems used, especially in molding and printing 3D polymeric objects.[29,30] Considering the vast advantages resulting from doping plastics with fillers to reinforce and alter mechanical properties of thermoplastics and thermosets, it is imperative develop photochemistries that yield reinforced composites by light irradiation in order to access chemically tunable 3D-printed objects made from materials that are sensitive to thermally-driven molding processes.

Herein, we introduce a modular strategy for multimaterial direct-ink-write (DIW) 3D printing composites and subsequent light-curing of thick and optically opaque hydrogels mediated by TTA-UC. We utilized a benchtop red light source (660 nm) to cure combinations of transparent hydrogels and opaque TiO_2 reinforced hydrogels. In order to test how TTA-UC compares to conventional UV light photocuring post-3D printing, core-shell objects were fabricated with a hydrogel core and TiO2-reinforced hydrogel shell. The limited penetration of UV light through the composite layer resulted in a “jammy gel” composite, comprising a cured shell and uncured core (Figure 4.1). In contrast, the construct cured via TTA-UC was cured through its entirety to afford a “hard-cured gel.” These results highlight the remarkable potential of implementing TTA-

UC to facilitate photoinitated polymer network formation through thick and opaque 3D printed objects that cannot be uniformly cured otherwise.

4.3 MATERIALS AND METHODS

4.3.1 Materials

Pluronics® F127 (BioReagent), triethanolamine (98%), Eosin Y (99%), Titanium(IV) oxide (325 mesh/44 microns, >99%) and $CDCl_3$ (D, 99.8% + 1% V/V TMS) were purchased from MilliporeSigma. Titanium(IV) oxide (NanoArc, 32 nm APS powder, 99.9%) was purchased from Alfa Aesar. 2-isocyanatoethyl methacrylate (>98%), dibutyltin dilaurate (>95%), and 2-hydroxy-2-methylpropiophenone (>96%) were purchased from TCI America. PdTPTBP was purchased from Santa Cruz Biotechnology, Inc. TIPS-anthracene was synthesized according to the reported procedure.[31] Diethyl ether, acetone, and tetrahydrofuran (HPLC grade) were purchased from Fisher Scientific. All reagents were used as received. Anhydrous methylene chloride was obtained by purification over alumina column on a Pure Process Technology purification system. Soybean oil was purchased from Alfa Aesar.

4.3.2 TTA-UC Solution Preparation

PdTPTBP (2.5 mg) was dissolved in tetrahydrofuran (1.00 mL) as a stock solution. To the freshly prepared stock solution (100 µL) was added TIPS-anthracene (14.0 mg). tetrahydrofuran (900 µL) was added to completely dissolve the TIPS-anthracene followed by the addition of soybean oil (1.00 mL). The control solution was made in the same way without addition of the TIPS-anthracene.

4.3.3 Synthesis of F127-BUM (New Workup Method)

Glassware was oven-dried at 125 °C for at least 16 h and F127 polymer (60 g, 4.8 mmol) was dried under vacuum (~ 2 Pa) for at least 16 h at room temperature in a round-bottom flask. Anhydrous dichloromethane (550 mL) was added to the flask under N_2 atmosphere. The mixture was stirred at 30 °C, and after the polymer has dissolved, dibutyltin dilaurate (12 drops) was added using a glass Pasteur pipette. The 2-isocyanatoethyl methacrylate (3.5 mL, 24.8 mmol) was diluted in anhydrous dichloromethane (50 mL) and added to the reaction mixture at a rate of approximately 1 drop/s. The reaction was left to stir under N_2 at 30 °C. After 2 d, the reaction was concentrated at 30 °C using a rotary evaporator. The polymer was precipitated by slowly pouring the concentrate into diethyl ether (1.8 L) in a large beaker. The precipitate mixture was stirred for an additional 30 min before turning off stirring to let the precipitate settle for 2 h. Diethyl ether was decanted off and the precipitate was then washed twice by adding diethyl ether (1 L), stirring for 15 min, and letting settle for 1 h. After the second washing, ether was decanted and the remaining residual amount was allowed to evaporate by agitating with a spatula under an N_2 flow. The resultant F127-BUM powder (56 g, 93.3% yield) was dried fully overnight at room temperature under vacuum (~ 2 Pa) and stored in the dark at 4 °C until further use.

4.3.4 Preparation of Hydrogels and Hydrogel Composites

The standard UV-cure hydrogels (5 g scale) were prepared by combining F127-BUM (1.5 g), TiO_2 (0.0x g; x = percent TiO_2), deionized water (3.5 – 0.0x g), and 2-hydroxy-2-methylpropiophenone (5 μL). The upconversion hydrogels were prepared by combining F127-BUM, TiO2, and deionized water. Triethanolamine (13.56 wt% solu. in PBS), Eosin Y (0.647 wt% solu. in PBS), and upconversion solution were then added via volumetric pipette, vortexed until mostly homogenous, and stored at 4 °C overnight to let F127-BUM dissolve. The amounts of each components used to make the upconversion hydrogels are summarized in Table 4.1. With the exception of tensile test, where both nano- and micron-sized TiO_2 particles were used, all other experiments used the micron-sized TiO_2.

4.3.5 Small-Angle X-Ray Scattering

Small-angle X-ray scattering (SAXS) was performed on beamline 12-ID-C at the Advanced Photon Source at Argonne National Laboratory over a Q-range of 0.01 to 1.3 $Å^{-1}$ in a pinhole configuration**.** The instrument used an X-ray source of 20 keV, corresponding to a wavelength of 0.62 Å, a beam size of 0.4 mm x 0.15 mm and a flux density of approximately 2 X 10^{12} photons/s/mm^2. Samples were loaded and cured in place in a custom aluminum 48 well plate, sealed between two Kapton windows.[32] SAXS data were collected at room temperature and with exposure times of 1 second each. Scattering profiles were radially integrated on-site using locally authored MATLAB software and were normalized using Kapton background subtraction.

4.3.6 Rheometric Characterization

Rheometrical characterization was performed on a TA Instruments DHR-2 equipped with an Advanced Peltier Plate system. All experiments were performed using the 8 mm flat stainless steel upper plate. The sample was cooled to 0 °C, then loaded by pouring the gel onto the bottom plate. The sample is then trimmed after the upper plate was lowered to the trim gap at 600 μm. The final geometry gap was then set to 500 μm, and pre-shear was applied at 5 °C for 10 s before additional sample conditioning at 25 °C for 8 min. The strain sweep experiment was performed to measure the storage and loss moduli over 0.01 to 100% strain (1 Hz). The cyclic shear strain experiment was performed at 25 °C using alternating strains of 1% for 5 min and 100% for 3 min (1 Hz). The frequency sweep experiment was performed to measure the storage and loss moduli at 1% strain over frequency range of 0.1 to 100.0 rad/s (equivalent to 0.0159-15.9 Hz). For the frequency sweep, the uncured material is trimmed at 1050 μm trim gap and the final gap is 1000 μm. For the frequency sweep on cured upconversion material, the gel was sandwiched between 2 microscope glass slides (using additional glass slides as spacers), and cured until 650 nm light for 25 minutes, and an 8 mm Royaltek biopsy punch was used to obtain the final sample. The sample is then placed on the geometry, which was lowered to a gap of 1000 μm (measured axial force = 1.7 N) for the data collection.

4.3.7 Gel Fraction Experiment

Cooled hydrogels are poured into a Sylgard mold for cylindrical samples (radius 10 mm, 5 mm height). Excess material was removed with a razor, and a large glass slide was placed over the top of the mold. The samples are then irradiated with 650 nm light for 25 min, and the entire setup was flipped and irradiated for an additional 5 min. The original masses are recorded, cut in halves and placed in tared scintillation vials with 10 mL acetone. The samples are then left for +1, +2, +3 days and acetone was decanted off and the vials are placed into vacuum oven for at least 24 h before mass of each sample is collected. The gel fractions are calculated by taking the ratio between the collected mass and the calculated dry original mass (original mass multiplied by percent of expected F127-BUM and TiO_2 in each formulation).

4.3.8 Mechanical Characterization

TestResources Universal Test System 1.1 kN electromechanical actuator single column load frame with a 44 N high accuracy S10 type load cell was used to evaluate the mechanical properties of the cured hydrogels. For dimensions of all dogbones, ASTM D638 type V specimen specifications were used. The dogbones were prepared by pouring the cooled hydrogel into a

Teflon dogbone. Excess material was scraped off by a razor and a microscope glass slide was placed on top. The gel was then exposed to 650 nm light for 25 min, then removed from the mold, flipped and cured for an additional 5 min. The sample was then attached to the vice grips with diamond grit jaw and subjected to increasing strain at a constant rate of 10 mm/min until mechanical failure.

4.3.9. Direct-write 3D Printing of Hydrogel Composites

Direct Ink Write 3D printing was performed on a HyRel Engine SR extrusion printer with SDS-5 syringer dispenser. The G-codes were written through a text editor. All printing was performed using F127-BUM upconversion system inks with an extrusion rate of 81 pulse/μL. The structures were printed with a layer height of 0.6 mm, with print speeds at 300 mm/min. After printing was completed, the printed structures are placed into a sealed petri dish and purged with argon before curing with red light for 25 minutes, followed by direct light curing with the petri dish lid off for another 10 minutes.

4.4 RESULTS AND DISCUSSION

4.4.1. Upconversion Hydrogel Composite Formulation

For this study, we used F127 bisurethane methacrylate (F127-BUM), which is a triblock copolymer that forms a versatile temperature responsive and shear-thinning hydrogel ink for DIW 3D printing (Figure 4.2a).[33] The hydrogel undergoes a temperature dependent sol-gel transition at ~17 °C[34,35], which enables additives to be incorporated homogenously while in its liquid form at low temperatures (5 °C). Upon warming to ambient temperature, the material becomes a self-supporting and shear-thinning gel that can be extruded from a nozzle to fabricate 3D constructs. Typically, a photoradical generator such as 2-hydroxy-4’-(2-hydroxyethoxy)-2-

methylpropiophenone[36] (Irgacure 2959) or Eosin Y/triethanolamine[37] is included in the crosslinkable F127 gel formulation for photocuring the construct. Thus, a hydrogel comprising a continuous polymer network can be formed by UV photoinitiated free radical polymerization of the F127-BUM chain ends.

To overcome the limitations of UV photoinitiated systems for hydrogels that absorb or scatter UV light, F127-BUM hydrogels were formulated with TTA-UC chromophores that could be incorporated within aqueous media.[31] Matching the absorption profile of Eosin Y was accomplished using the combination of palladium(II) meso-tetraphenyl tetrabenzoporphyrin (PdTPTBP) and 9,10-bis((triisopropylsilyl)ethynyl)anthracene (TIPS-anthracene), a sensitizer and annihilator, respectively (Figure 4.1).[38] The TTA-UC chromophores were dissolved in a mixture of tetrahydrofuran (THF) and soybean oil, the latter acting as an oxygen scavenger necessary to avoid quenching of triplet excitons.[39] A conventional photoredox initiator system based on Eosin Y and triethanolamine (TEA) was chosen since it can be activated using blue light.[40,41] The TTA-UC system is introduced to the 30 wt% F127-BUM hydrogel via addition of the sensitizer + annihilator, Eosin Y, and TEA solutions, followed by vortexing. While incorporation of other additives into hydrogels can change the polymer-polymer and polymer-solvent interaction gelation[42–45], our hydrogel with the TTA-UC system did not exhibit a significant shift in LCST (Figure 4.2b) and retains shear thinning behavior (Figure 4.2c).

4.4.2. Hydrogel Properties

F127-BUM self-assembles in aqueous media to form micelles that pack into ordered lattices that give rise to the gel state.[46] Characterization of these hydrogels by SAXS confirmed that the addition of the upconversion components did not disrupt the assembled structure in the gel (Figure 4.3a). There was no significant increase in the q-value, which represents the average intermicellar distance, in the presence of the TTA-UC additives. Thus, the presence of emulsion droplets (Figure 4.3b) from the TTA-UC solution does not alter the F127 micelle size and packing. The ratios of normalized Q-values amongst the peaks for both samples suggest the presence of micelles with ordered BCC packing, consistent with another study that observed BCC packing in purified F127.[47]

The viscoelastic properties of the hydrogel inks were characterized by rheometry to determine their suitability for DIW 3DP. Figure 4.4a shows a strain sweep experiment at room temperature, where the storage moduli at low strains (< 1%) was 30-40 kPa, suggesting firm gels that can support the load from subsequent layers in a multi-layered construct. Upon increasing applied strain, the materials exhibited a yielding behavior where the storage modulus decreased rapidly the loss modulus eventually exceeded the storage modulus. This gel-to-sol transition allows the hydrogels to flow out of the nozzle during the printing process. A cyclic strain experiment (Figure 4.4b), wherein the gel was subjected to alternating high (100%) and low (15%) strains showed that the changes in the moduli are reversible and instantaneous. The results show that the hydrogel can be extruded from a nozzle with an immediate response to applied force, and quickly recovers its gel state upon exiting the nozzle. Thus, these rheometric experiments suggest the addition of the TTA-UC components to the F127-BUM hydrogel does not affect its viscoelastic behaviors.

4.4.3. Photopolymerization with Visible Red Light

The F127-BUM hydrogel containing TTA-UC additives was photocured with red (660 nm) and UV (365 nm) light, and compared it to a control hydrogel (containing sensitizer, initiator system, but no annihilator). As shown in Figure 4.5a, both the upconversion and control hydrogels crosslinked under UV light, however, only the TTA-UC hydrogel crosslinked under red light. This result demonstrates that without the annihilator, the photoinitiator system remains inactive when exposed to red light, and no crosslinking was observed. We further confirmed the crosslinking using a frequency sweep rheometric experiment on the hydrogel pre- and post-cured with red light. The storage modulus increased three-fold after crosslinking and was stable across a range of frequencies over time, suggesting irreversible crosslinking (Figure 4.5b).

4.4.4. Using Red Light to Cure Opaque Hydrogel Composites

Inorganic fillers have been added to hydrogels to reinforce and modify the mechanical properties[48,49], but have limited function in photocurable materials as addition of the fillers reduce the transparency of the matrix.[50] As a representative example, we included TiO_2 particles in our hydrogels, which allowed us to test whether using red light can offer an advantage in deeper light penetration through opaque materials. In order to demonstrate this, we added varying amounts of TiO_2 particles into the hydrogel to reduce the transparency of the material. The gels were cast into a mold, cured, then cut in half to observe the extent of curing inside. While samples cured with UV light have uncured material in the center (more with increasing wt% TiO_2 particles), all samples cured with red light were entirely crosslinked through the center (Figure 4.6a). This observation was further quantified through gel fraction experiments, where the samples were cut in half and any material not crosslinked into the network are extracted with acetone. For transparent samples without TiO_2, the gel fraction for samples cured using UV light retained 96.2±1.5 wt% of the original polymer mass, but the samples cured using red light retained 84.21±0.55 wt%. We posit that potential side-reactions with the alkene groups in soybean oil could decrease the gel-fraction[51], which may be circumvented using other oxygen scavengers. On one hand, as we increased the amount of TiO_2, the mass fractions of samples cured with 365 nm light (Figure 4.6b) rapidly decreased, going from 64.7±2.5% (1 wt% TiO_2), to 21.1±1.1% (2 wt% TiO_2), to 14.3±3.9%

(5 wt% TiO_2). On the other hand, the mass fractions for samples cured with 650 nm light (Figure 4.6c) were very close to each other, between 81.83±0.87%(1 wt% TiO_2) and 76.91±0.96% (5 wt% TiO_2). The similar mass fractions suggested that samples cured using red light was not affected by addition of particles that reduce transparency, allowing the hydrogels to cure consistently throughout the structure. Through the same rheometric frequency sweep experiments as Figure 2E, we have demonstrated successful red light curing for hydrogels containing up to 15 wt% TiO_2 (Figure 4.7).

4.4.5. Mechanical Properties of Hydrogel Composites

To characterize the differences in mechanical properties of the hydrogel composites, such as Young's modulus and maximum strain, we performed tensile tests on the dogbones that were cast and cured using red light, shown in Figure 4.8. The calculated Young's modulus and maximum strain are summarized in Table 4.2. To further probe the effect of particle size, we did measurements on both micron and nanometer-sized TiO_2 particles. With increasing amount of micron-sized TiO_2, the Young's moduli increased and the maximum strain decreased. For the addition of nanometer-sized TiO_2, the particles initially have a plasticizing effect at low concentrations, reducing the Young's moduli and increasing the maximum strain, but ultimately stiffened the material as we increased the amount. The ability to either stiffen or soften the material with different types, size, and concentration of particles[52–54], and the limit to filler concentration that contributes to the change in mechanical properties aligned with other observations in literature.[23,55,56] While the increase in filler amount from 2 to 5 wt% of the nanometer-sized particles seemed to have a significant increase in stiffness, there was no significant difference for the micron-particles. This observation was attributed to the difficulty in dispersing larger particles in the hydrogel, as settling can occur and prevent the filler from effectively tuning the mechanical properties. While this study was only limited to 2 types of fillers, we were able to obtain a wide range of Young's modulus ranging from 27.98±0.46 to 80.2±5.8 kPa, falling into the same range of many soft biological tissues (vocal ligament 33.1 kPa[57], cardiac tissue 5-50 kPa[58], lens 54 kPa[59], glandular breast tissue 48-66 kPa[60], skin 50-150 kPa[61]). Additionally, our values were in similar range to many reported soft hydrogels systems developed for biological tissue mimics.[62–64] In future studies, varying the polymer composition, type and particle size of fillers can also further expand the range of mechanical properties.

4.4.6. Multi-Material DIW Printing of Hydrogel Composites

DIW printing enables the fabrication of multi-material objects without the need for a highly customized printer such as multi-wavelength printer[10,65], and the ability to print with compositional variations throughout the printed structure.[66–69] This form of AM also allows us to print the entire structure before photocuring, which enables polymer networks to be formed in the x, y, and z directions, and across the extruded filament boundaries. As a result, interlayer defects and interfacial boundaries between contrasting materials of a multi-material print were minimized, resulting in improved mechanical properties.[70,71] Therefore, multi-material DIW 3DP of hydrogel composites can be used to simulate biological systems comprising a complex scaffold of multiple cell type domains with varying mechanical properties.[72–74] As shown in Figure 4.9a, various architectures of dual composite materials of gels with and without particle additives were printed using a HyRel mechanical extrusion printer. The hydrogel and composite inks were readily transferred into syringes for extrusion while in their sol state at ~5 °C. The inks were extruded through a 20-gauge nozzle (0.603 mm I.D.) to produce filaments with 0.67 mm diameter to fabricate multi-material objects that could vary in their composition in the x, y, and z directions (Figure 4.9b). First, we printed a clear hydrogel layer sandwiched between 2 opaque hydrogel layers (Figure 4.9c), followed by irradiation with the light source above the opaque layer. Using UV light clearly resulted in a sluggishly cured gel that lost its shape when pressed. On the other hand, implementing TTA-UC to mediate photocuring resulted a thoroughly cured, mechanically robust polymer network. Another key advantage of the polymers used is that the interface between the opaque and clear layers contains methacrylic groups that can effectively fuse the entire construct. Thus, the multi-material print maintained its spatially and compositionally defined regions even after cutting through the object.

To challenge the photocuring process mediated by TTA-UC in opaque constructs, we devised an experiment to test the chemistry of core-shell objects (Figure 4.10). The printed constructs were cured with UV or red light, and then submerged in water to remove the uncured material. To our surprise, the cube structures with a transparent shell cured entirely under both conditions. Although UV light cannot penetrate through opaque regions, it is possible for the radical polymerization that initiates in the transparent regions to then propagate into the opaque section. However, the structure with the opaque shell led to drastic differences when irradiated with UV vs. red light. While the entire structure can be cured throughout by red light, the same structure irradiated with UV light exhibited a significant amount of uncured material in both layers, as evidenced by the presence of a void in the center of the cube. Although transparent, the core of the structure was not cured when using UV light.

Lastly, we explored the opportunity to exploit DIW printing of composites to create complex structures with mechanical reinforcement furnished by particle additives. Prior studies of gels with gradient layered structures highlight the importance of varying the mechanical properties within molded objects.[75] Thus, we printed composites with macroscopically well-defined interfaces between particle-reinforced and pristine gels. An optical microscopy image of a cross section (Figure 4.11a) of the structure from Figure 4C left in water for 1 month showed distinct separation between the materials (dark area = 1% TiO_2, transparent area = 0% TiO_2), revealing precise spatial control of printed materials by DIW. To compare differences in the mechanical properties of pristine and composite structures, we printed pristine gels and layered composite dogbones (five alternating layers of transparent hydrogel and TiO2 hydrogel composite). Uniaxial tensile experiments revealed that composite dogbones can undergo twice the stretching distance before failure, suggesting a potential to use TiO_2/hydrogel composite as reinforcement layers to the overall printed structure (Figure 4.11b). Interestingly, the Young's modulus of both systems remains the same. These results underscore the importance of photocurable-particle reinforced 3D printed objects.

4.5 CONCLUSION

In summary, we demonstrated how unconventional photochemical multiexciton processes can be exploited for initiating polymer network formation within 3D printed hydrogel composites. Low energy light can penetrate into visibly opaque hydrogels laden with TiO_2 particles, and TTA-UC chromophores activated the photoredox initiators to induce the formation of a covalent polymer network. While complementary systems that respond to visible light have emerged for initiating radical chemistries[17,76,77], our study shows that simply modifying the mechanism to activate conventional photoinitiation systems can be a powerful tool to chemically modify objects that block high energy photons. F127-BUM hydrogels retained their printability despite the addition of the TTA-UC components and TiO_2 particles. Multi-material DIW 3DP with hydrogel composites afforded homogeneously cured constructs with mechanically enhanced properties. The fabrication of these, and other hydrogel composites, via TTA-UC will have future utility as inks for DIW 3DP to produce complex multi-material objects with low optical transparency for use in tissue engineering and soft robotics.

4.5 REFERENCES

(1) Zheng, Y.; Zhang, W.; Baca Lopez, D. M.; Ahmad, R. Scientometric Analysis and Systematic Review of Multi-Material Additive Manufacturing of Polymers. *Polymers* **2021**, *13*, 1957.

(2) Lopes, L. R.; Silva, A. F.; Carneiro, O. S. Multi-material 3D printing: The relevance of materials affinity on the boundary interface performance. *Addit. Manuf.* **2018**, *23*, 45–52.

(3) Boydston, A. J.; Cao, B.; Nelson, A.; Ono, R. J.; Schwartz, J. J.; Thrasher, C. J. Additive manufacturing with stimuli-responsive materials. *J. Mater. Chem. A* **2018**, *6*, 20621–20645.

(4) Truby, R. L.; Lewis, J. A. Printing soft matter in three dimensions. *Nature* **2016**, *540*, 371–378.

(5) Hartings, M R.; Ahmed, Z. Chemistry from 3D printed objects. *Nat. Rev. Chem.* **2019**, *3*, 305–314.

(6) Layani, M.; Wang, X.; Magdassi, S. Novel Materials for 3D Printing by Photopolymerization. *Adv. Mater.* **2018**, *30*, 1706344.

(7) Zhu, J.; Marchant, R. E. Design properties of hydrogel tissue-engineering scaffolds. *Expert Rev. Med. Devices*, 2011, **8**, 607–626.

(8) Tan, L. J.; Zhu, W.; Zhou, K. Recent Progress on Polymer Materials for Additive Manufacturing. *Adv. Funct. Mater.* **2020**, *30*, 2003062.

(9) Bao, Y.; Paunović, N.; Leroux, J.-C. Challenges and Opportunities in 3D Printing of Biodegradable Medical Devices by Emerging Photopolymerization Techniques. *Adv. Funct. Mater.* **2022**, *32*, 2109864.

(10) Ge, Q.; Chen, Z.; Cheng, J.; Zhang, B.; Zhang, Y. F.; Li, H.; He, X.; Yuan, C.; Liu, J.; Magdassi, S.; Qu, S. 3D printing of highly stretchable hydrogel with diverse UV curable polymers. *Sci. Adv.* **2021**, *7*, eaba4261.

(11) Frost, B. A.; Sutliff , B. P.; Thayer , P.; Bortner, M. J.; Foster, E. J. Gradient Poly(ethylene glycol) Diacrylate and Cellulose Nanocrystals Tissue Engineering Composite Scaffolds via Extrusion Bioprinting. *Front. Bioeng. Biotechnol.* **2019**, *7*, 280.

(12) Highley, C. B.; Rodell, C. B.; Burdick, J. A. Direct 3D Printing of Shear-Thinning Hydrogels into Self-Healing Hydrogels. *Adv. Mater.* **2015**, *27*, 5075–5079.

(13) Fuchs, Y.; Soppera, O.; Haupt, K. Photopolymerization and photostructuring of molecularly imprinted polymers for sensor applications--a review. *Anal. Chim. Acta*, 2012, **717**, 7–20.

(14) Gómez, M. L.; Williams, R. J. J.; Montejano H. A.; Previtali, C. M. Influence of the ionic character of a drug on its release rate from hydrogels based on 2-hydroxyethylmethacrylate and acrylamide synthesized by photopolymerization. *EXPRESS Polym. Lett.*, 2012, **6**, 189–197.

(15) Qi, Z.; Xu, J.; Wang, Z.; Nie, J.; Ma, G. Preparation and properties of photo-crosslinkable hydrogel based on photopolymerizable chitosan derivative. *Int. J. Biol. Macromol.*, 2013, **53**, 144–149.

(16) Ash, C.; Dubec, M.; Donne, K.; Bashford, T. Effect of wavelength and beam width on penetration in light-tissue interaction using computational methods. *Lasers Med. Sci.*, 2017, **32**, 1909–1918.

(17) Ahn, D.; Stevens, L. M.; Zhou, K.; Page, Z. A. Additives for Ambient 3D Printing with Visible Light. *Adv. Mater.* **2021**, *33*, 2104906.

(18) Awwad, N.; Bui, A. T.; Danilov, E. O.; Castellano, F. N. Visible-Light-Initiated Free-Radical Polymerization by Homomolecular Triplet-Triplet Annihilation. *Chem* **2020**, *6*, 3071–3085.

(19) Zhao, J.; Ji, S.; Guo, H. Triplet–triplet annihilation based upconversion: from triplet sensitizers and triplet acceptors to upconversion quantum yields. *RSC Adv.* **2011**, *1*, 937–950.

(20) Saha, S. K.; Wang, D.; Nguyen, V. H.; Chang, Y.; Oakdale, J. S.; Chen, S. Scalable submicrometer additive manufacturing. *Science* **2019**, *366*, 105–109.

(21) Xing, J.; Zheng, M.; Duan, X. Two-photon polymerization microfabrication of hydrogels: an advanced 3D printing technology for tissue engineering and drug delivery. *Chem. Soc. Rev.* **2015**, *44*, 5031–5039.

(22) Maruo, S.; Nakamura, O.; Kawata, S. Three-dimensional microfabrication with two-photon-absorbed photopolymerization. *Opt. Lett.* **1997**, *22*, 132–134.

(23) Song, J.; Michas, C.; Chen, C. H.; White, A. E.; Grinstaff, M. W. From Simple to Architecturally Complex Hydrogel Scaffolds for Cell and Tissue Engineering Applications: Opportunities Presented by Two-Photon Polymerization. *Adv. Healthcare Mater.* **2020**, *9*, 1901217.

(24) Jung, K.; Corrigan, N.; Ciftci, M.; Xu, J.; Seo, S. E.; Hawker, C. J.; Boyer, C. Designing with Light: Advanced 2D, 3D, and 4D Materials. *Adv. Mater.* **2020**, *32*, 1903850.

(25) Zhu, J.; Zhang, Q.; Yang, T.; Liu, Y.; Liu, R. 3D printing of multi-scalable structures via high penetration near-infrared photopolymerization. *Nat. Commun.* ***2020***, *11*, 3462.

(26) Yi, G. S.; Chow, G. M. Synthesis of Hexagonal-Phase $NaYF_4$:Yb,Er and $NaYF_4$:Yb,Tm Nanocrystals with Efficient Up-Conversion Fluorescence. *Adv. Funct. Mater.* **2006**, *16*, 2324–2329.

(27) Bharmoria, P.; Bildirir, H.; Moth-Poulsen, K. Triplet–triplet annihilation based near infrared to visible molecular photon upconversion. *Chem. Soc. Rev.* **2020**, *49*, 6529–6554.

(28) Zhou, J.; Liu, Q.; Feng, W.; Sun, Y.; Li, F. Upconversion Luminescent Materials: Advances and Applications. *Chem. Rev.* **2015**, *115*, 395–465.

(29) Ravetz, B. D.; Pun, A. B.; Churchill, E. M.; Congreve, D. N.; Rovis, T.; Campos, L. M. Photoredox catalysis using infrared light via triplet fusion upconversion. *Nature* **2019**, *565*, 343–346.

(30) Sanders, S. N.; Schloemer, T. H,; Gangishetty, M. K.; Anderson, D.; Seitz, M.; Gallegos, A. O.; Stokes, R. C.; Congreve, D. N. Triplet fusion upconversion nanocapsules for volumetric 3D printing. *Nature* **2022**, *604*, 474–478.

(31) Meir, R.; Hirschhorn, T.; Kim, S.; Fallon, K. J.; Churchill, E. M.; Wu, D.; Yang, H. W.; Stockwell, B. R.; Campos, L. M. Photon Upconversion Hydrogels for 3D Optogenetics. *Adv. Funct. Mater.* **2021**, *31*, 2010907.

(32) L. D. Pozzo. 'SAXS-USAXS Liquids 48 well plate holder', https://github.com/pozzo-research-group/Automation-Hardware/tree/master/Cartridge%20Sample%20Holder%20for%20SAS%20Experiments/SAXS-USAXS%20Liquids%2048%20well%20plate%20holder (accessed Aug 30,2022).

(33) Millik, S. C.; Dostie, A. M.; Karis, D. G.; Smith, P. T.; McKenna, M.; Chan, N.; Curtis, C. D.; Nance, E.; Theberge, A. B.; Nelson, A. 3D printed coaxial nozzles for the extrusion of hydrogel tubes toward modeling vascular endothelium. *Biofabrication* **2019**, *11*, 045009.

(34) Texter, J.; Schwarz, R. Fouling release and antifouling coatings derived from thermoreversible gels. *Polymer Preprints* **2005**, *46*, 1238–1239.

(35) Shaikhullina, M.; Khaliullina, A.; Gimatdinov, R.; Butakov, A.; Chernov, V.; Filippov, A. NMR relaxation and self-diffusion in aqueous micellar gels of pluronic F-127. *J. Mol. Liq.* **2020**, *306*, 112898.

(36) Wu, C.-J.; Gaharwar, A. K.; Chan, B. K.; Schmidt, G. Mechanically Tough Pluronic F127/Laponite Nanocomposite Hydrogels from Covalently and Physically Cross-Linked Networks. *Macromolecules* **2011**, *44*, 8215–8224.

(37) Biase, M. D.; de Leonardis, P.; Castelletto, V.; Hamley, I. W.; Derby, B.; Tirelli, N. Photopolymerization of Pluronic F127 diacrylate: a colloid-templated polymerization. *Soft Matter* **2011**, *7*, 4928–4937.

(38) Nishimura, N.; Gray, V.; Allardice, J. R.; Zhang, Z.; Pershin, A.; Beljonne, D.; Rao, A. Photon Upconversion from Near-Infrared to Blue Light with TIPS-Anthracene as an Efficient Triplet–Triplet Annihilator. *ACS Materials Lett.* **2019**, *1*, 660–664.

(39) Liu, Q.; Xu, M.; Yang, T.; Tian, B.; Zhang, X.; Li, F. Highly Photostable Near-IR-Excitation Upconversion Nanocapsules Based on Triplet–Triplet Annihilation for in Vivo Bioimaging Application. *ACS Appl. Mater. Interfaces* **2018**, *10*, 12, 9883–9888.

(40) Bahney, C. S.; Lujan, T. J.; Hsu, C. W.; Bottlang, M.; West, J. L.; Johnstone, B. Visible light photoinitiation of mesenchymal stem cell-laden bioresponsive hydrogels *Eur Cell Mater*. **2011**, *22*, 43–55.

(41) Sharifi, S.; Sharifi, H.; Akbari, A.; Chodosh, J. Systematic optimization of visible light-induced crosslinking conditions of gelatin methacryloyl (GelMA). *Sci. Rep.* **2021**, *11*, 23276.

(42) Pandit, N. K.; Kisaka, J. Loss of gelation ability of Pluronic® F127 in the presence of some salts. *Int. J. Pharm.* **1996**, *145*, 129–136.

(43) Dai, M.; Tian, Y.; Fan, J.; Ren, J.; Liu, Y.; Rahman, M.D. M.; Ren, X.; Ma, H. Tuning cellulose ethers LCST. *BioRes.* **2019**, *14*, 7977–7991.

(44) Xu, R.; Tian, J.; Guan, Y.; Zhang, Y. Extraordinarily Large LCST Depression Converts Nonthermosensitive Polymer to Thermosensitive. *Macromolecules* **2019**, *52*, 365–375.

(45) Abou-Shamat, M. A.; Calvo-Castro, J.; Stair, J. L.; Cook, M. T. Modifying the Properties of Thermogelling Poloxamer 407 Solutions through Covalent Modification and the Use of Polymer Additives. *Macromol. Chem. Phys.* **2019**, *220*, 1900173.

(46) Prud'homme, R. K.; Wu, G.; Schneider, D. K. Structure and Rheology Studies of Poly(oxyethylene−oxypropylene−oxyethylene) Aqueous Solution. *Langmuir* **1996**, *12*, 4651–4659.

(47) Mortensen, K.; Batsberg, W.; Hvidt, S. Effects of PEO−PPO Diblock Impurities on the Cubic Structure of Aqueous PEO−PPO−PEO Pluronics Micelles: fcc and bcc Ordered Structures in F127. *Macromolecules* **2008**, *41*, 1720–1727.

(48) Rezwana, K.; Chena, Q. Z.; Blakera, J. J.; Boccaccini, A. R. Biodegradable and bioactive porous polymer/inorganic composite scaffolds for bone tissue engineering. *Biomaterials* **2006**, *27*, 3413–3431.

(49) Jiang, D.; Ning, F.; Wang, Y. Additive manufacturing of biodegradable iron-based particle reinforced polylactic acid composite scaffolds for tissue engineering. *J. Mater. Process. Technol.* **2021**, *289*, 116952.

(50) Ma, Q.; Zhang, Y.; Launay, V.; Dot, M. L.; Liu, S.; Lalevée, J. How to overcome the light penetration issue in photopolymerization? An example for the preparation of high content iron-containing opaque composites and application in 3D printing. *Eur. Polym. J.*, 2022, **165**, 111011.

(51) Zhao, T.; Li, X.; Yu, R.; Zhang, Y.; Yang, X.; Zhao, X.; Wang, L.; Huang, W. Silicone–Epoxy-Based Hybrid Photopolymers for 3D Printing. *Macromol. Chem. Phys.* **2018**, *219*, 1700530.

(52) Gantar, A.; da Silva, L. P.; Oliveira, J. M.; Marques, A. P.; Correlo, V. M.; Novak, S.; Reis, R. L. Nanoparticulate bioactive-glass-reinforced gellan-gum hydrogels for bone-tissue engineering. *Mater. Sci. Eng.* **2014**, *43*, 27–36.

(53) Czichya, C.; Spangenberg, J.; Günthera, S.; Gelinsky, M.; Odenbach, S. Determination of the Young's modulus for alginate-based hydrogel with magnetite-particles depending on storage conditions and particle concentration. *J. Magn. Magn. Mater.* **2020**, *501*, 166395.

(54) Yu, Y.; Yuk, H.; Parada, G. A.; Wu, Y.; Liu, X.; Nabzdyk, C. S.; Youcef-Toumi, K.; Zang, J.; Zhao, X. Hydrogels: Multifunctional “Hydrogel Skins” on Diverse Polymers with Arbitrary Shapes. *Adv. Mater.* **2019**, *31*, 1807101.

(55) Utech, S.; Boccaccini, A. R. A review of hydrogel-based composites for biomedical applications: enhancement of hydrogel properties by addition of rigid inorganic fillers. *J. Mater. Sci.* **2016**, *51*, 271–310.

(56) Jang, T. S.; Jung, H. D.; Pan, H. M.; Han, W. T.; Chen, S.; Song, J. 3D printing of hydrogel composite systems: Recent advances in technology for tissue engineering. *Int. J. Bioprint.* **2018**, *4*, 126.

(57) Min, Y. B.; Titze, I. R.; Alipour-Haghighi, F. Stress-strain response of the human vocal ligament. *Ann. Otol. Rhinol. Laryngol.* **1995**, *104*, 563–569.

(58) Domian, I. J.; Yu, H.; Mittal, N. On Materials for Cardiac Tissue Engineering. *Adv. Healthcare Mater.* **2017**, *6*, 1600768.

(59) Heys, K. R.; Cram, S. L.; Truscott, R. J. W. Massive increase in the stiffness of the human lens nucleus with age: the basis for presbyopia? *Mol. Vis.* **2004**, *10*, 956–963.

(60) Singh, G.; Chanda, A. Expansion potential of skin grafts with novel I-shaped auxetic incisions. *Biomed. Mater.* **2021**, *16*, 062004.

(61) Guimarães, C. F.; Gasperini, L.; Marques, A. P.; Reis. R. L. The stiffness of living tissues and its implications for tissue engineering. *Nat. Rev.* **2020**, *5*, 351–370.

(62) Feig, V. R.; Tran, H.; Lee, M.; Bao, Z. Mechanically tunable conductive interpenetrating network hydrogels that mimic the elastic moduli of biological tissue. *Nat. Commun.* 2018, *9*, 2740.

(63) Chen, R.; Xu, X.; Yu, D.; Xiao, C.; Liu, M.; Huang, J.; Mao, T.; Zheng, C.; Wang, Z.; Wu, X. Highly stretchable and fatigue resistant hydrogels with low Young's modulus as transparent and flexible strain sensors. *J. Mater. Chem. C* **2018**, *6*, 11193.

(64) Tronci, G.; Neffe, A. T.; Pierce, B. F.; Lendlein, A. An entropy–elastic gelatin-based hydrogel system. *J. Mater. Chem.* **2010**, *20*, 8875–8884.

(65) Dolinski, N. D.; Callaway, E. B.; Sample, C. S.; Gockowski, L. F.; Chavez, R.; Page, Z. A.; Eisenreich, F.; Hecht, S.; Valentine, M. T.; Zok, F. W.; Hawker, C. J. Tough

Multimaterial Interfaces through Wavelength-Selective 3D Printing. *ACS Appl. Mater. Interfaces* **2021**, *13*, 22065.

(66) Skylar-Scott, M. A.; Mueller, J.; Visser, C. W.; Lewis, J. A. Voxelated soft matter via multimaterial multinozzle 3D printing. *Nature* **2019**, *575*, 330–335.

(67) Chen, K.; Zhang, L.; Kuang X.; Li, V.; Lei, M.; Kang, G.; Wang, Z. L.; Qi, H. J. Dynamic Photomask-Assisted Direct Ink Writing Multimaterial for Multilevel Triboelectric Nanogenerator. *Adv. Funct. Mater.* **2019**, *29*, 1903568.

(68) Kokkinis, D.; Schaffner, M.; Studart, A. R. Multimaterial magnetically assisted 3D printing of composite materials. *Nat. Commun.* **2015**, *6*, 8643.

(69) Rocha, V. G.; Saiz, E.; Tirichenko, L. S.; García-Tuñón, E. Direct ink writing advances in multi-material structures for a sustainable future. *J. Mater. Chem. A* **2020**, *8*, 15646–15657.

(70) Wong, J.; Basu, A.; Wende, M.; Boechler, N.; Nelson, A. Mechano-Activated Objects with Multidirectional Shape Morphing Programmed via 3D Printing. *ACS Appl. Polym. Mater.,* 2020, **7**, 2504–2508.

(71) Chen, K.; Kuang, X.; Li, V.; Kang, G.; Qi, H. J. Fabrication of tough epoxy with shape memory effects by UV-assisted direct-ink write printing. *Soft Matter* **2018**, *14*, 1879–1886.

(72) Jammalamadaka, U.; Tappa, K. Recent Advances in Biomaterials for 3D Printing and Tissue Engineering. *J. Funct. Biomater.* **2018**, 9, 22.

(73) Advincula, R. C.; Dizon, J. R. C.; Caldona, E. B.; Viers, R. A.; Siacor, F. D. C.; Maalihan, R. D.; Espera Jr., A. H. On the progress of 3D-printed hydrogels for tissue engineering. *MRS Communications* **2021**, *11*, 539–553.

(74) Zhu, W.; Ma, X.; Gou, M.; Mei, D.; Zhang, K.; Chen, S. 3D printing of functional biomaterials for tissue engineering. *Curr. Opin. Biotechnol.* **2016**, *40*, 103–112.

(75) Karpiak, J. V.; Ner, Y.; Almutairi, A. Density Gradient Multilayer Polymerization for Creating Complex Tissue. *Adv. Mater.* **2012**, *24*, 1466–1470.

(76) Ahn, D.; Stevens, L. M.; Zhou, K.; Page, Z. A. Rapid High-Resolution Visible Light 3D Printing. *ACS Cent. Sci.* **2020**, *6*, 1555–1563.

(77) Wu, Z.; Jung, K.; Boyer, C. Effective Utilization of NIR Wavelengths for Photo-Controlled Polymerization: Penetration Through Thick Barriers and Parallel Solar Syntheses. *Angew. Chem. Int. Ed.* **2020**, *59*, 2013–2017.

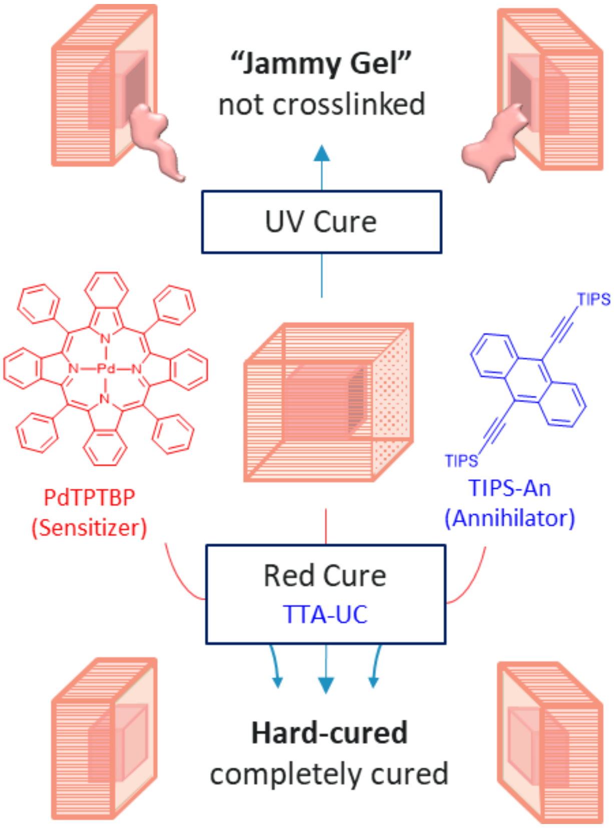

Figure 4.1 Design and formulation of TTA-UC hydrogel system. A) Our strategy was to cure a hydrogel composite with an opaque component by using low energy red light, which offered better penetration into most opaque materials and exploited the TTA-UC to obtain blue light to initiate crosslinking.

wt% TiO$_2$	F127-BUM [g]	TiO$_2$ [g]	DI H$_2$O [g]	TEA solu. [μL]	Eosin Y solu. [μL]	UC solu. [μL]
0	1.5	0	3.393	37	50	20
1	1.5	0.05	3.343	37	50	20
2	1.5	0.10	3.293	37	50	20
5	1.5	0.25	3.143	37	50	20

Table 4.1 Formulations for upconversion hydrogel/TiO$_2$ composites (5g scale).

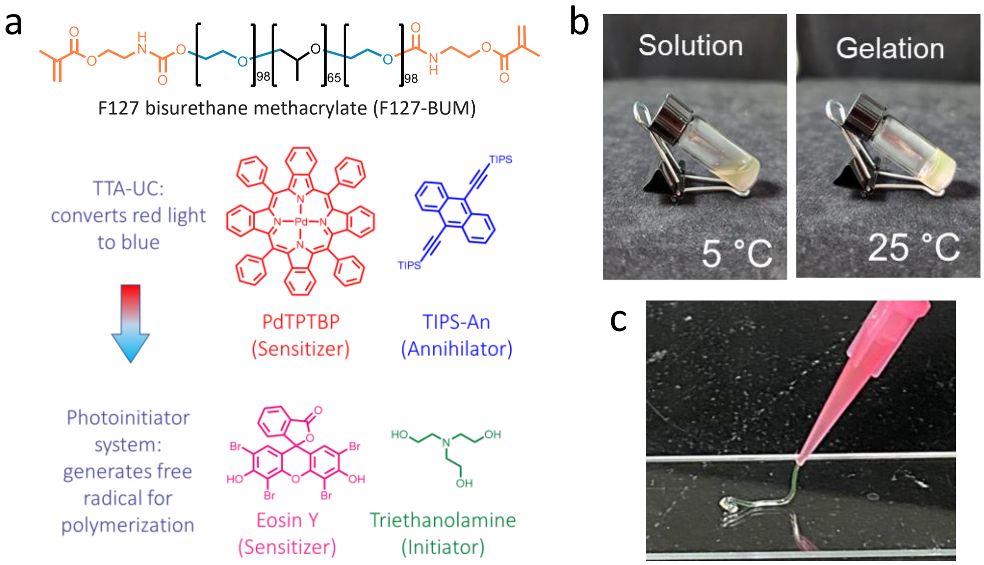

Figure 4.2 Our selected base material, F127-BUM hydrogel, forms micelles when dissolved in water and can undergo LCST transition and shear-thinning behavior (a). Upon addition of the TTA-UC system, the hydrogel retains its ability to undergo LCST sol-gel transition (b) and shear thin (c).

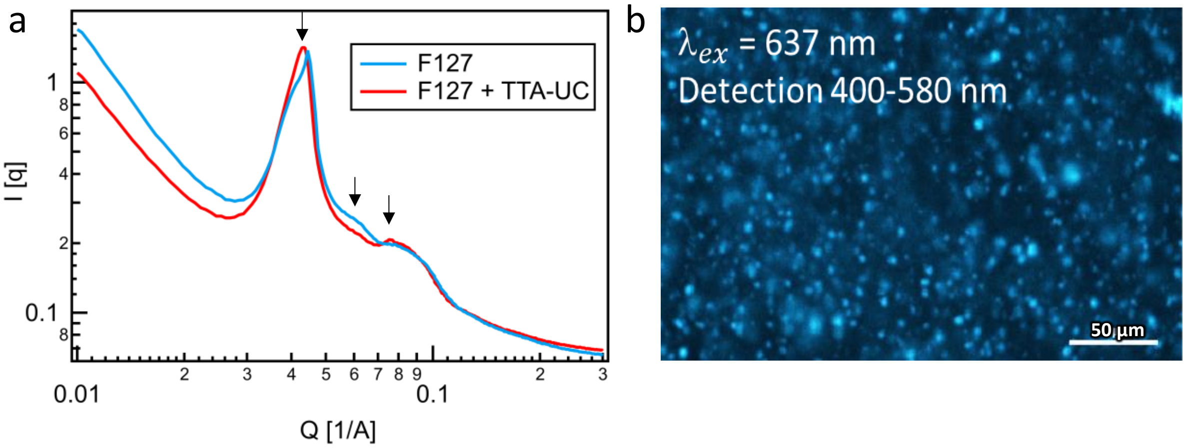

Figure 4.3 SAXS characterization of hydrogel inks with and without the TTA-UC additives. a) SAXS suggest BCC packing of F127-BUM micelles that leads to gelation was not affected by the presence of micron-sized upconversion droplets resulting from the emulsion between tetrahydrofuran, water, and soybean oil (b).

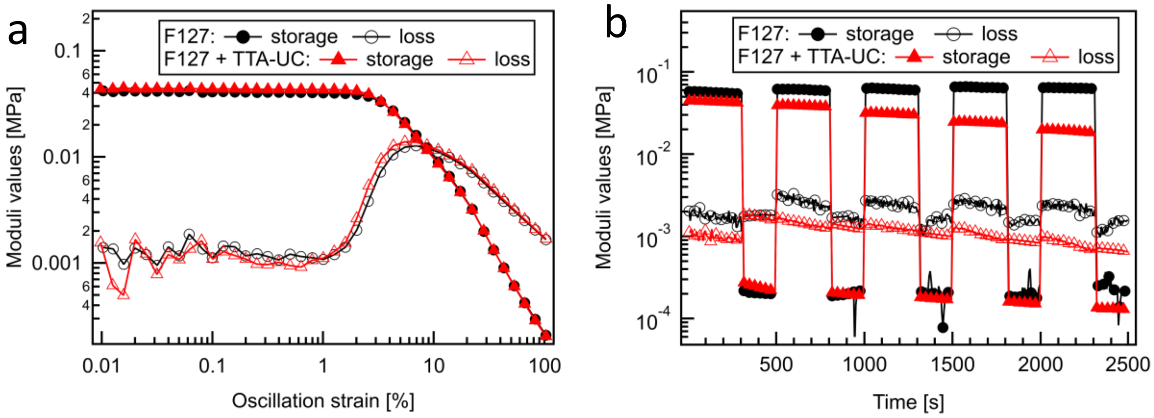

Figure 4.4 Rheometrical characterization includes a) strain sweep and b) cyclic strain experiments. Addition of TTA-UC additives did not affect the viscoelastic properties the material possess for good printability.

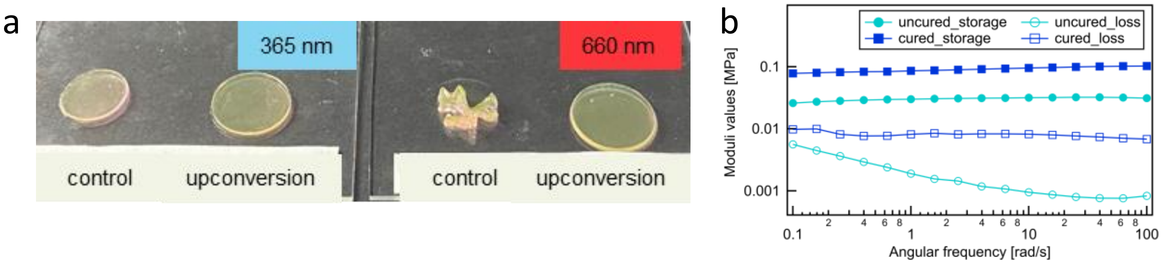

Figure 4.5 Red light curing of the TTA-UC and control gels (a), showing all components of TTA-UC system was required for photocuring with red light, and a frequency sweep rheometric experiment (b) to show the three-fold, irreversible increase of storage moduli after photocuring.

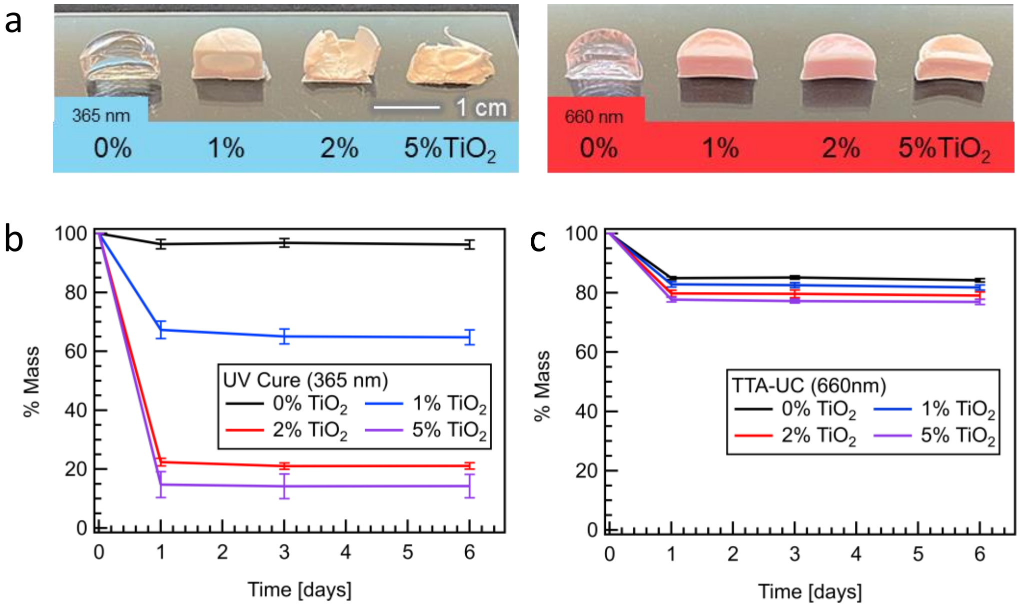

Figure 4.6 Characterization of materials after photocuring. a) Cross-sections of gel fraction samples with increasing amounts of TiO_2 after 6 days of acetone extraction. Gel fraction experiments for samples cured under UV light (b) and red light (c) reveals that the transparent samples (0 wt% TiO_2) has a higher extent of curing when cured with UV light, but had a difficult time curing when TiO_2 was added, while gel fraction of samples cured under red light were not significantly affected due to the addition of TiO_2.

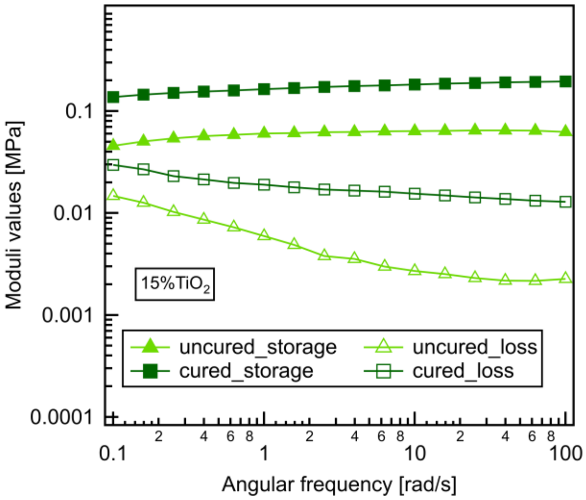

Figure 4.7 Frequency sweep rheometric experient to show the irreversible increase of storage moduli for the cured material at the maximum amount of TiO_2 loading tested at 15 wt%.

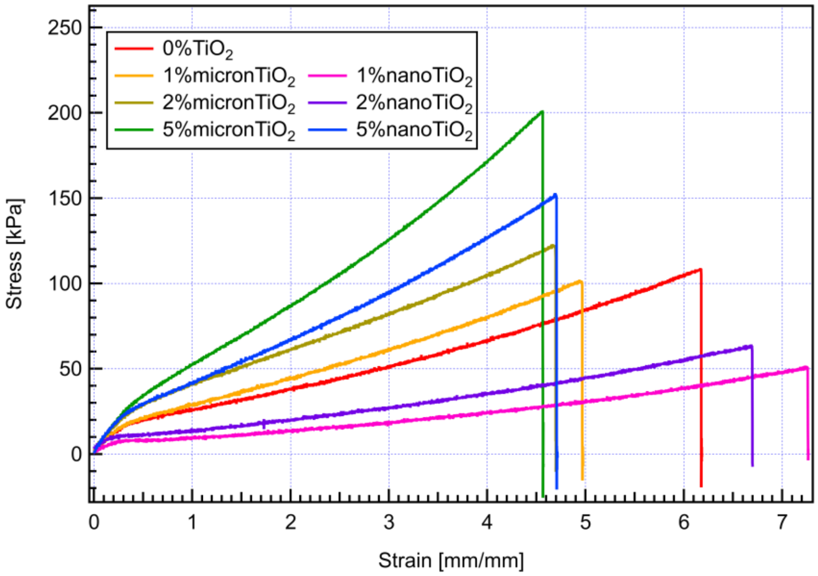

Figure 4.8 Tensile stress-strain curve for hydrogel samples with varying amounts of TiO_2.

	0% TiO_2	1% micron TiO_2	2% micron TiO_2	5% micron TiO_2	1% nano TiO_2	2% nano TiO_2	5% nano TiO_2
Young's Modulus [kPa]	53.63±0.99	51.2±4.9	73.2±1.2	79.1±4.1	27.98±0.46	36.8±2.0	80.2±5.8
Maximum Strain [mm/mm]	5.70±0.63	4.51±0.36	4.00±1.4	5.50±1.2	6.51±0.53	5.65±0.83	3.69±1.2

Table 4.2 Calculated Young's modulus and maximum strain from tensile test in Figure 3D. Micron TiO_2 particle size is 44 microns, while the nano TiO_2 particle size is 32 nm.

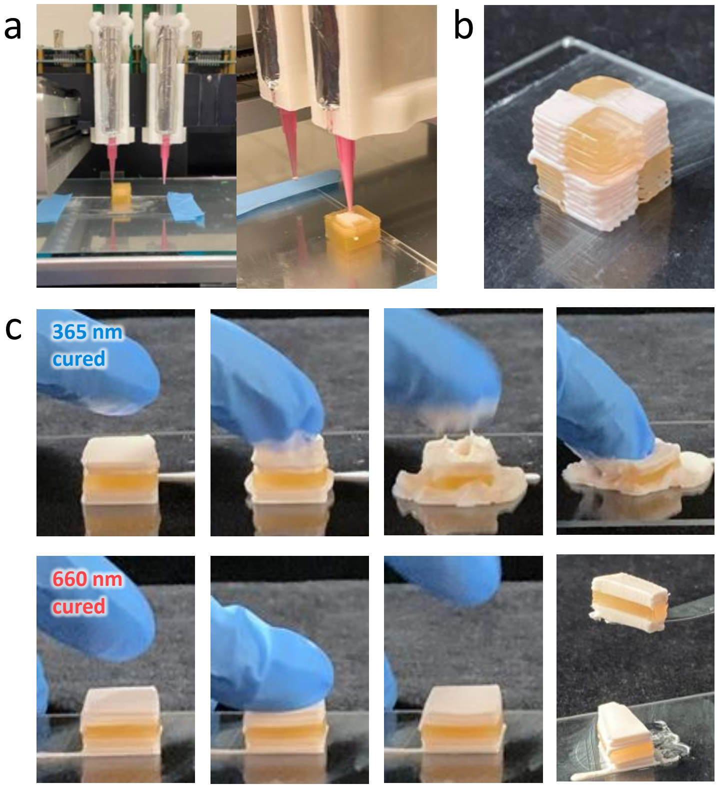

Figure 4.9 Multi-material DIW 3DP demonstrations using a HyRel extrusion printer (a) Prints include with changing materials in x,y,z directions b) checkered cube, c) sandwich cured under both UV and red light, where the UV cured structure was not cured entirely.

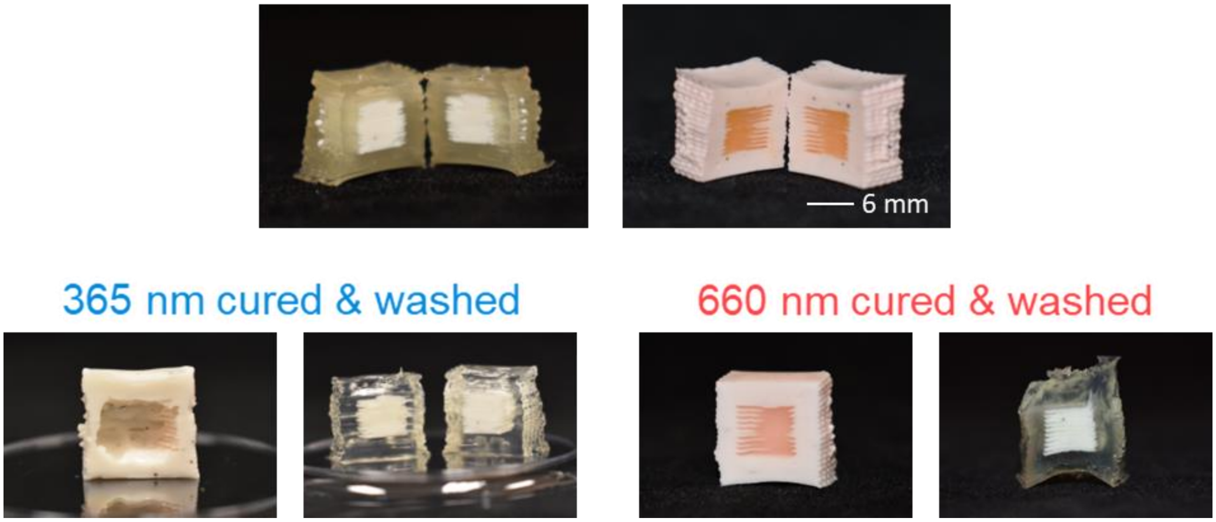

Figure 4.10 The structures in (D) are cured and washed and shown in (E) and (F). E) The UV cured structure on the right side is not cured completely, but F) red light cured structures were both completely cured.

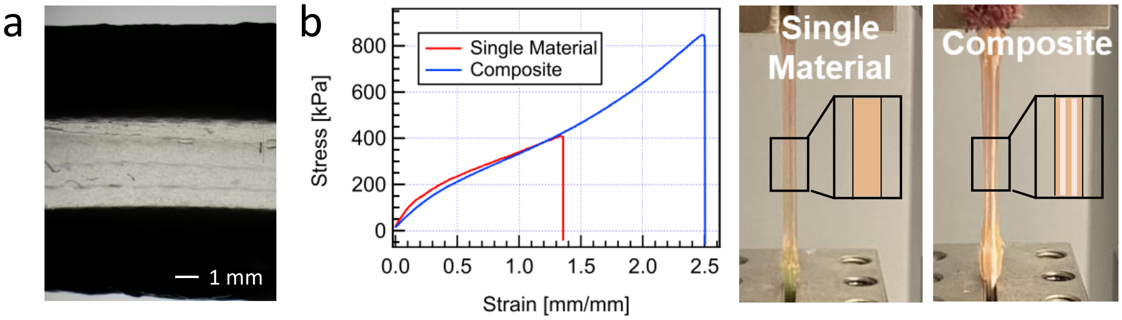

Figure 4.11 Optical microscopy image of sandwich (1 mm slice) in Figure 4.9c. H) Tensile test for printed single material (0% TiO_2) and composite (alt. layers 0/1% TiO_2) dogbones.

APPENDIX A

3D Printing Ion Gel Auxetic Frameworks for Stretchable Sensors

Ionic Liquid Screening

Imidazolium ILs with 5 different anions were screened for compatibility with F127-BUM to obtain a self-supporting gel. Imidazolium ILs were picked for their commercial availability and cost. The ILs were screened by dissolving 20-40 wt% F127-BUM. For ILs with hydrophilic anions, such as dimethyl phosphate (DMP) and hydrogen sulfate (HSO_4), F127-BUM overall has poor solubility. Despite use of methanol as cosolvent, the polymer precipitated out upon evaporation. For the ILs with hydrophobic anions, such as hexafluorophosphate (PF_6) and bis(trifluoromethane)sulfonimide (TFSI), F127-BUM dissolves in the ILs without the use of a cosolvent. However, no gelation was observed**,** which we hypothesized is due to lack of phase separation required for micelle formation, as both the PEO and PPO blocks of F127-BUM has good solubility due to the ion-dipole and hydrophobic interaction, respectively, with the ILs. For ILs with tetrafluoroborate anion (BF_4), F127-BUM was initially insoluble. But with use of methanol cosolvent to encourage the initial dissolution, clear, self-supporting gels were obtained upon evaporation of methanol. This lead us to the conclusion that in order to obtain a gel, the PPO block needs to be partially soluble in the IL. However, further studies are required to confirm these observations.

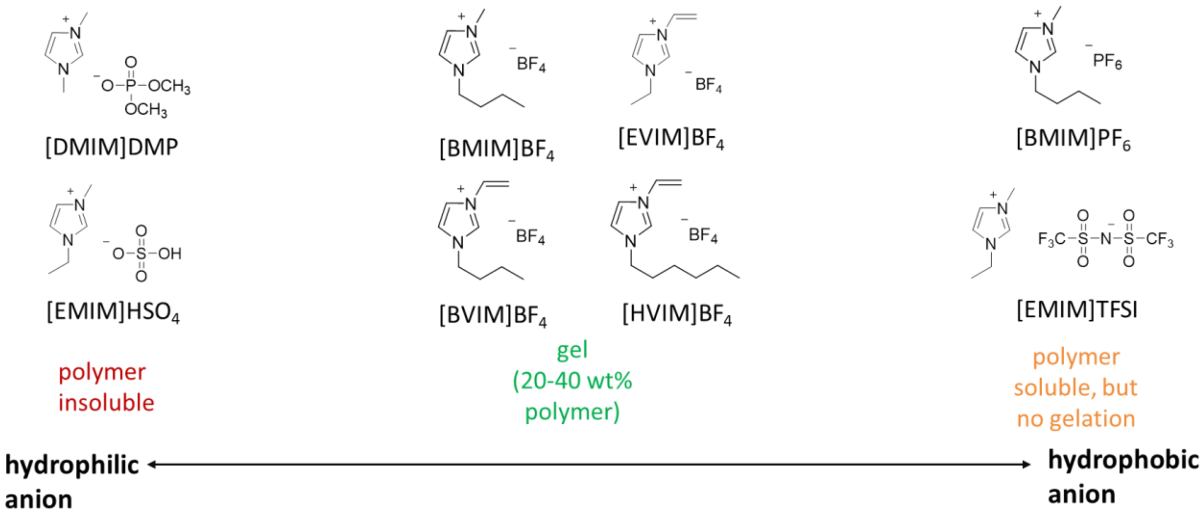

Figure A1. Screening of Ionic Liquids for Gel Formation with F127-BUM

APPENDIX B

Mechano-Activated Objects with Multi-Directional Shape Morphing Programmed via 3D Printing

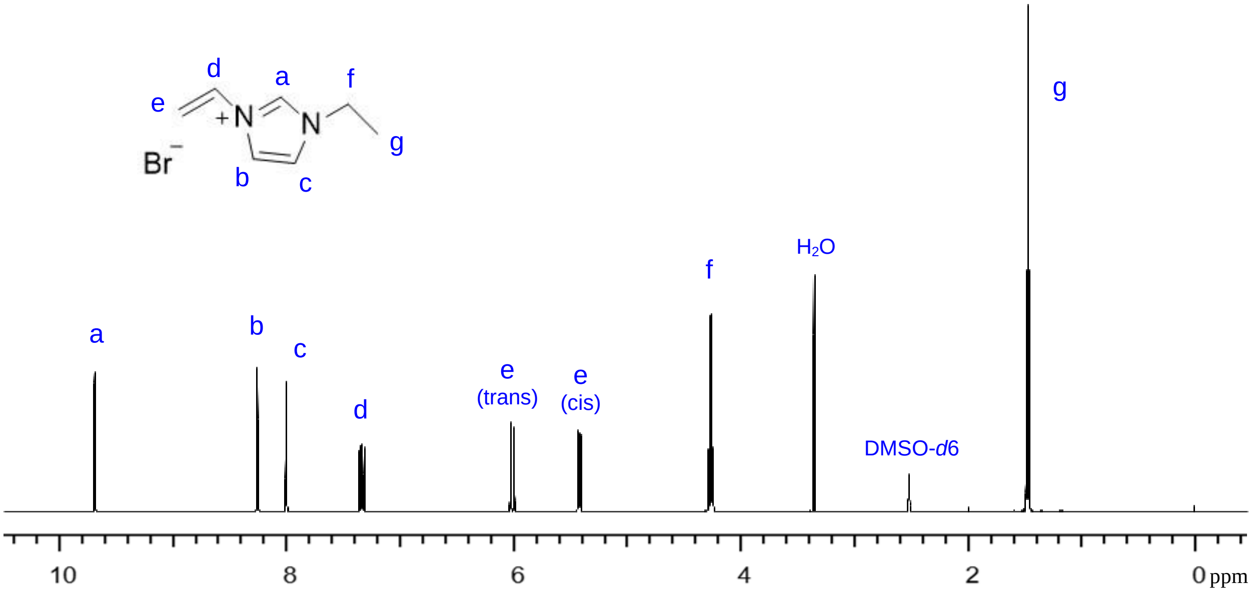

Figure B1. ^{1}H NMR of [EVIM]Br, 500 MHz frequency, *T* = 298 K

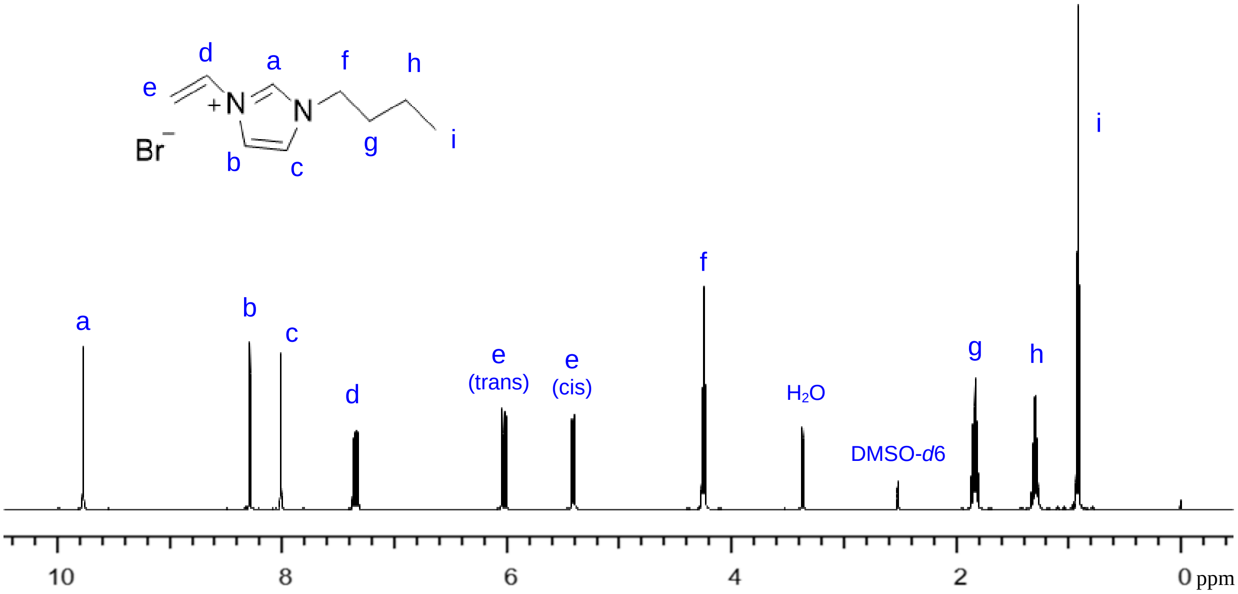

Figure B2. ^{1}H NMR of [BVIM]Br, 500 MHz frequency, *T* = 298 K

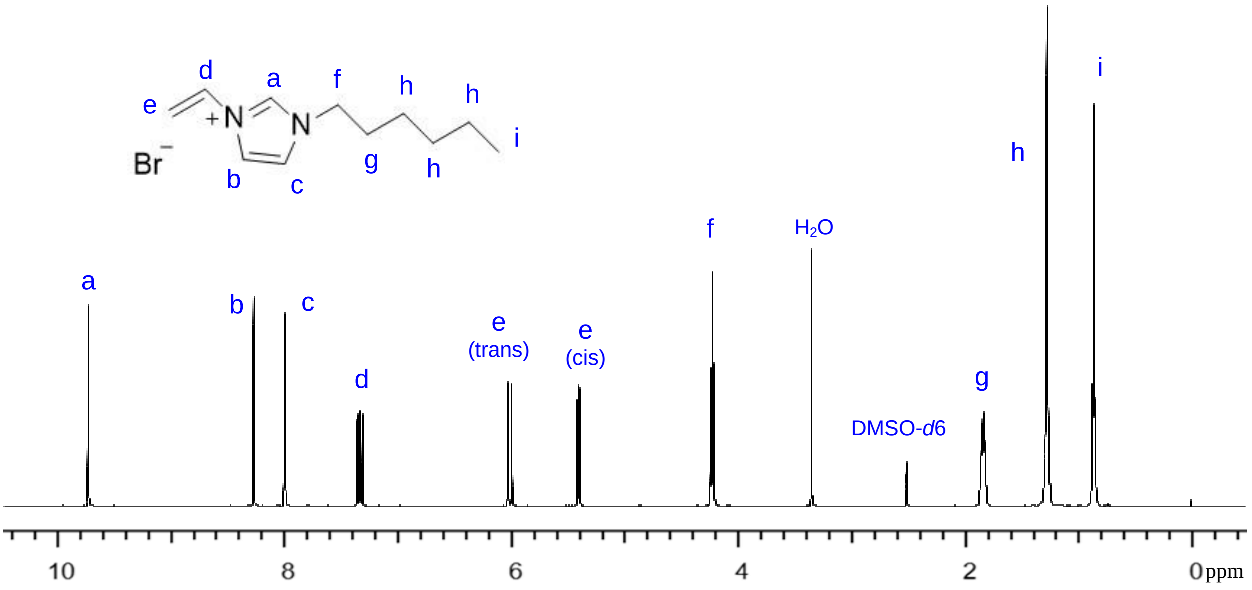

Figure B3. ^{1}H NMR of [HVIM]Br, 500 MHz frequency, T = 298 K

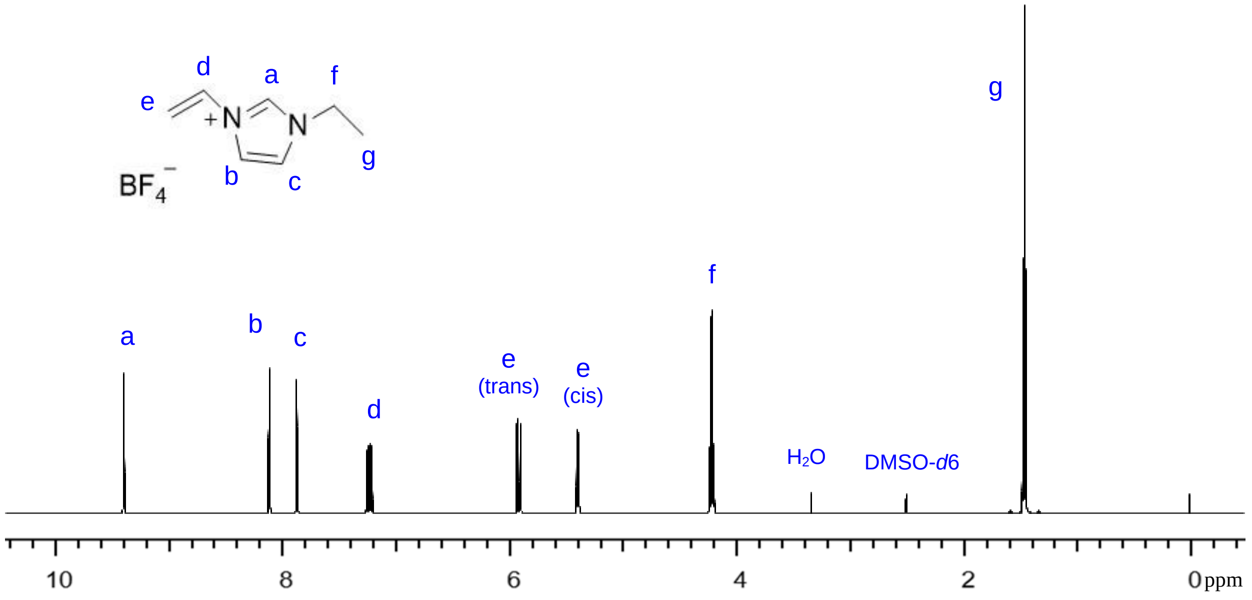

Figure B4. ^{1}H NMR of [EVIM]BF_4, 500 MHz frequency, T = 298 K

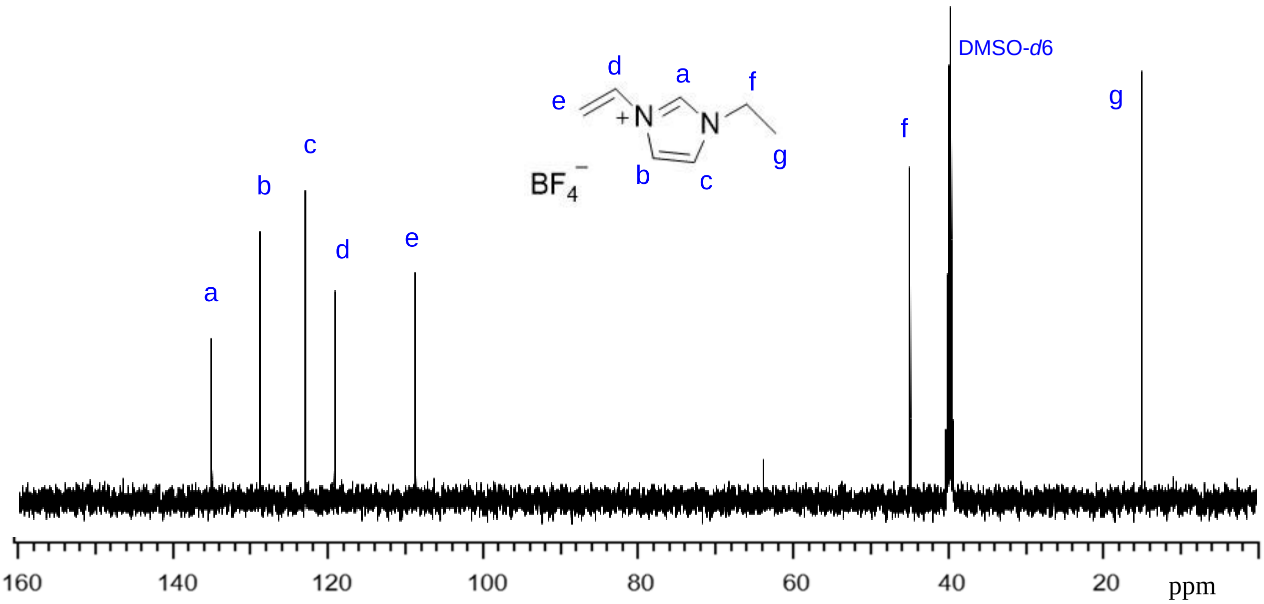

Figure B5. ^{13}C NMR of [EVIM]BF$_4$, 500 MHz frequency, T = 298 K

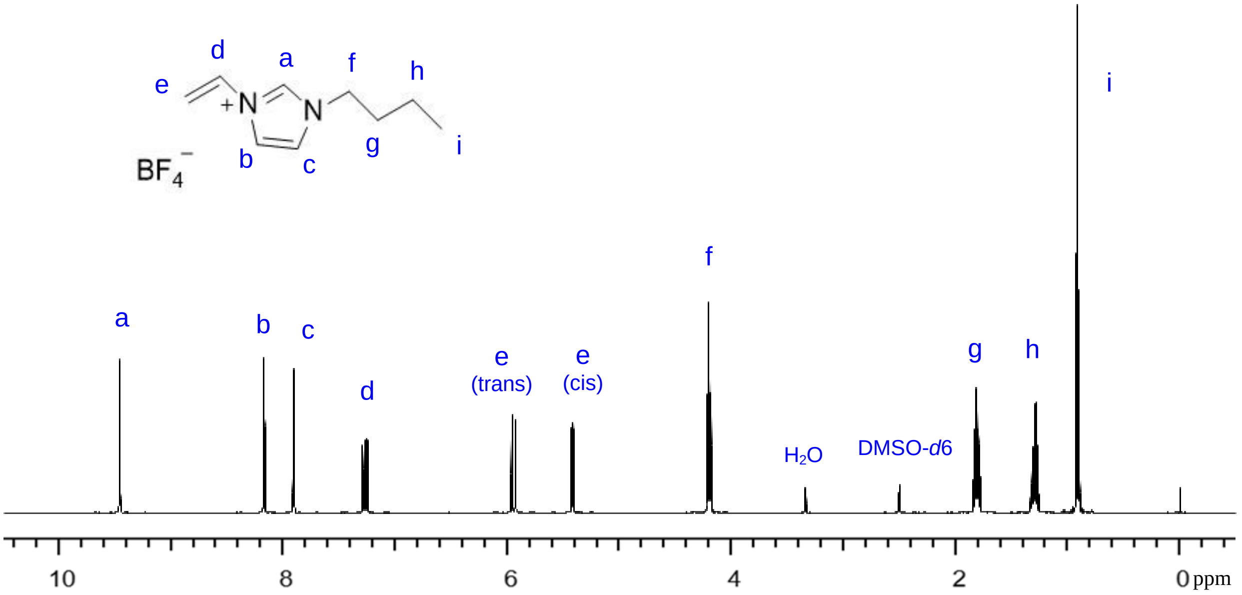

Figure B6. ^{1}H NMR of [BVIM]BF$_4$, 500 MHz frequency, T = 298 K

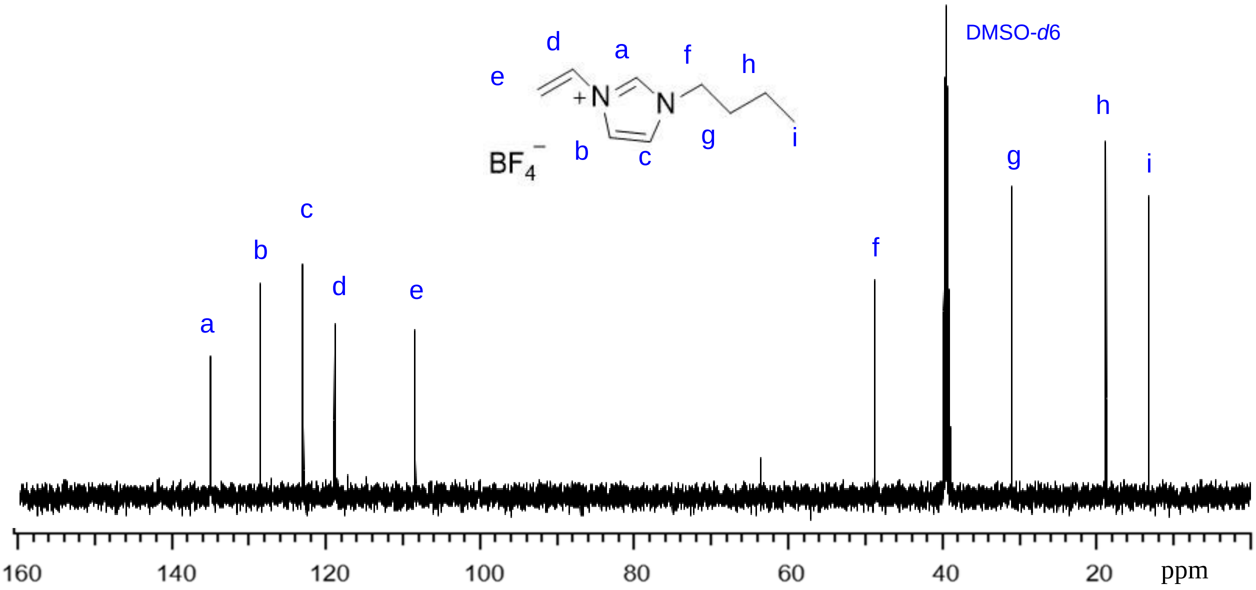

Figure B7. ^{13}C NMR of [BVIM]BF_4, 500 MHz frequency, T = 298 K

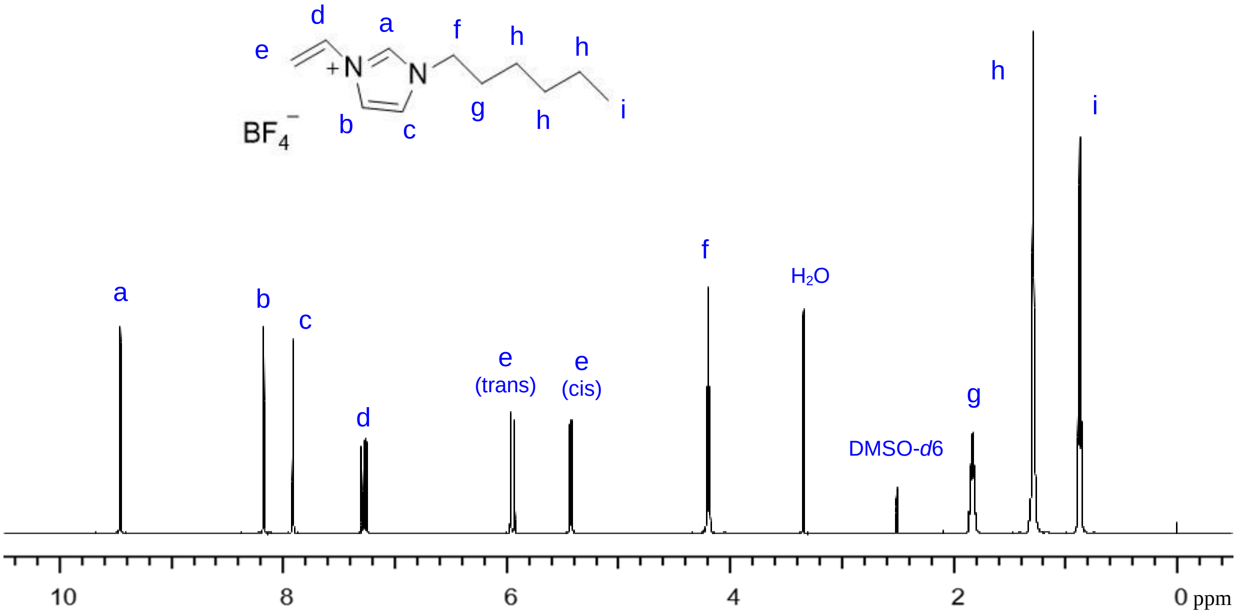

Figure B8. ^{1}H NMR of [HVIM]BF_4, 500 MHz frequency, T = 298 K

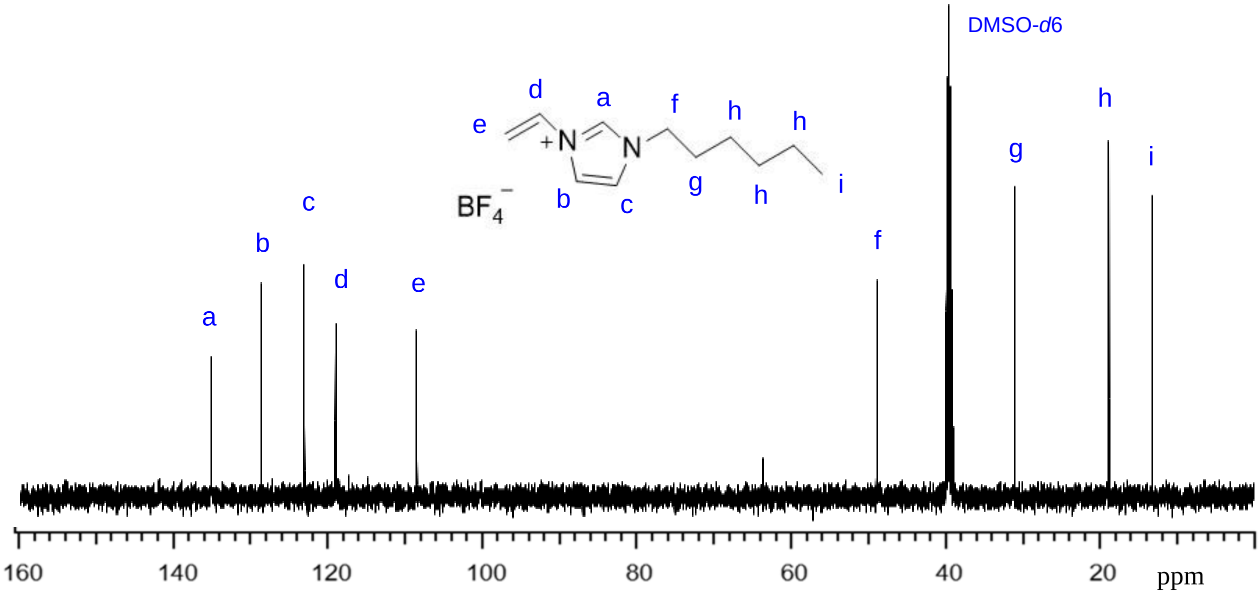

Figure B9. ^{13}C NMR of [HVIM]BF$_4$, 500 MHz frequency, *T* = 298 K